DISSERTATIONES
PHYSICAE
UNIVERSITATIS
TARTUENSIS
107

FRED VALK

Nitrogen emission spectrum as a measure of electric field strength in low-temperature gas discharges

DISSERTATIONES PHYSICAE UNIVERSITATIS TARTUENSIS
107

DISSERTATIONES PHYSICAE UNIVERSITATIS TARTUENSIS
107

FRED VALK

Nitrogen emission spectrum as a measure of electric field strength in low-temperature gas discharges

UNIVERSITY OF TARTU
Press

This study was carried out at the Institute of Physics, University of Tartu.

The Dissertation was admitted on November 1, 2016 in partial fulfilment of the requirements for the degree of Doctor of Philosophy in physics, and allowed for defence by the Council of the Institute of Physics, University of Tartu.

Supervisors: Dr. Märt Aints, Institute of Physics, University of Tartu, Estonia.

Dr. Peeter Paris, Institute of Physics, University of Tartu, Estonia.

Opponent: Dr. Ronny Brandenburg, Leibniz Institute for Plasma Science and Technology, Germany.

Defence: January 25, 2017, at University of Tartu, Estonia.

This study was supported by the Estonian Science Foundation under grants 4518, 5675, 6928, 7318 and 8237.

ISSN 1406-0647
ISBN 978-9949-77-315-2 (print)
ISBN 978-9949-77-316-9 (pdf)

University of Tartu Press
www.tyk.ee

CONTENTS

LIST OF ORIGINAL PUBLICATIONS

This thesis is based on the following papers:

I. Paris P, Aints M, Laan M and Valk F 2004 Measurement of intensity ratio of nitrogen bands as a function of field strength *J. Phys. D: Appl. Phys.* **37** 1179–84 http://iopscience.iop.org/0022-3727/37/8/005/

II. Paris P, Aints M, Valk F, Plank T, Haljaste A, Kozlov K V and Wagner H-E 2005 Intensity ratio of spectral bands of nitrogen as a measure of electric field strength in plasmas *J. Phys. D: Appl. Phys.* **38** 3894–9 http://iopscience.iop.org/0022-3727/38/21/010/

III. Paris P, Aints M, Valk F, Plank T, Haljaste A, Kozlov K V and Wagner H-E 2006 Reply to comments on 'Intensity ratio of spectral bands of nitrogen as a measure of electric field strength in plasmas' *J. Phys. D: Appl. Phys.* **39** 2636–2639 http://iopscience.iop.org/0022-3727/39/12/N01/

IV. Valk F, Aints M, Paris P, Plank T, Maksimov J and Tamm A 2010 Measurement of collisional quenching rate of nitrogen states $N_2(C^3\Pi_u, v = 0)$ and $N_2^+(B^2\Sigma_g^+, v = 0)$ *J. Phys. D: Appl. Phys.* **43** 385202 http://iopscience.iop.org/0022-3727/43/38/385202/

Other publications:

V. Aints M, Valk F, Plank T, Paris P and Jõgi I 2012 Ozone production rate as a function of electric field strength in oxygen *J. Phys. D: Appl. Phys.* **45** 205201 http://iopscience.iop.org/0022-3727/45/20/205201/

VI. Plank T, Jalakas A, Aints M, Paris P, Valk F, Viidebaum M, Jõgi I 2014 Ozone generation efficiency as a function of electric field strength in air *J. Phys. D: Appl. Phys.* **47** 335205 http://iopscience.iop.org/0022-3727/47/33/335205/

Presentations at international conferences:

1. Paris P, Aints M, Valk F, Plank T, Haljaste A 2005 Intensity ratio of nitrogen bands as a function of field strength, XXVIIth ICPIG, July 2005, Eindhoven, the Netherlands.

2. Paris P, Valk F, Aints M, Kozlov K V 2007 Ozone production in dark discharge, XXVIIIth ICPIG, July 2007, Prague, Czech Republic.

3. Paris P, Aints M, and Valk F 2009 Collisional quenching rates of $N_2^+(B^2\Sigma_g^+, v = 0)$, Contr. Papers 17th Symposium on Application of Plasma Processes, January 2009, Liptovsky Jan, Slovakia.

Author's contribution:

Paper I: All measurements were made by the author.

Papers II–III: All measurements were made by the author. Author also performed calculations needed and modelled the processes under investigation.

Paper IV: All measurements were made under the supervision of the author. Author preformed calculations needed and modelled processes under investigation; also main person responsible for writing the paper.

SYMBOLS, UNITS AND ABBREVIATIONS

Symbols and units:

U, V	–	voltage. U_d – voltage applied to the electrodes, gap voltage; U_a – HV source output voltage (50–5000 V).
d, m	–	distance between the electrodes (0.15–5.6 mm).
S, m^2	–	area; S_e – electrode area; S_d – discharge area (≈ 2.54 cm^2).
p, Pa	–	gas pressure (1–760 Torr; ~ 0.1–100 kPa).
i, A	–	discharge current (0.5–2 μA);
$\boldsymbol{E}$, V/m	–	macroscopic electric field (strength) ($E \sim 10^6$ V/m); E_ρ – electric field produced by space charge. $\lvert\boldsymbol{E}\rvert = E$.
T, K	–	(gas) temperature ($T \approx 300$ K); T_i – ion temperature; T_e – electron temperature.
N, m^{-3}	–	gas number density, the number of gas molecules in one cubic meter (~ 10^{22} – 10^{25} m^{-3}); N – nitrogen atom.
n	–	total number of particles. May denote different species: n_e – total number of electrons.
ρ, m^{-3}	–	charged or excited particle number density; defined similarly to gas number density but may denote different charged species: ρ_e – electron number density; ρ_p – positive ion number density.
E/N, Td	–	electric field strength divided by gas number density, usually referred to as reduced electric field strength; typically measured in units of Td (Townsend), where 1 Td = 10^{-21} V·m^2 (100–4000 Td).
μ, m^2/V·s	–	mobility of a charged species; μ_e – electron mobility; μ_p – positive ion mobility, etc.
$\boldsymbol{v}$, m/s	–	drift velocity; $\boldsymbol{v}_e$ – electron drift velocity; $\boldsymbol{v}_p$ – positive ion drift velocity; $\boldsymbol{v}_{nu}$ – unstable negative ion drift velocity; $\boldsymbol{v}_{ns}$ – stable negative ion drift velocity.
τ, s	–	time constant of a process, e.g. the time during which the number of (excited) particles decreases e (≈ 2.718) times. τ_0 – natural lifetime.
σ, m^2	–	cross-section of a particular collisional process.
k, m^3/s	–	rate constant of a second-order process (chemical reaction); k_1, s^{-1} – first-order; k_3, m^6/s – third-order rate constant.
α, m^{-1}	–	mean number of ionizing collisions per electron per unit drift path length. Often referred to as the first Townsend (also ionization or avalanche) coefficient.
η, m^{-1}	–	mean number of attachments per electron drifting 1 m in electronegative gas in the opposite direction of the field.

β, m^{-1}	– mean number of conversion processes per unstable negative ion in a time an electron drifts 1 m in the opposite direction of the electric field.
δ, m^{-1}	– mean number of detachment processes per unstable negative ion in a time an electron drifts 1 m in the opposite direction of the electric field.
W, eV	– energy, 1 eV (electronvolt) ≈ $1.602 \cdot 10^{-19}$ J.
$\boldsymbol{\Gamma}$, $m^{-2} \cdot s^{-1}$	– particle flux density.
γ_{se}	– number of secondary electrons produced by one incident positive ion on cathode. Dimensionless quantity.
I_λ, 1/s	– emission intensity, photon flux, at wavelength λ.
$R_{\lambda 1/\lambda 2}$	– intensity ratio of spectral bands at λ_1 and λ_2.
r, Ω	– electrical resistance.
≈	– denotes inexact identity, i.e. approximately equal.
~	– denotes same order of magnitude or proportionality.
Δ	– denotes non-infinitesimal change of a quantity.

Non SI units used in this work:

Td	= 10^{-21} V·m^2	=	10^{-17} V·cm^2
Torr	≈ 1 mm Hg	≈	133.32 Pa
760 Torr	= 1 atm	≈	760.001 mm Hg (at T_0 and g_0)

Abbreviations:

EEDF	– Electron Energy Distribution Function.
FNS	– First Negative System.
SPS	– Second Positive System.

Physical constants and conversion factors used in this work:

p_0	= 100 kPa ≈ 0.987 atm	Standard pressure; STP (IUPAC).
T_0	= 0ºC (273.15 K)	Standard temperature; STP (IUPAC).
k_B	≈ $1.3807 \cdot 10^{-23}$ J/K	Boltzmann constant.
e	≈ $1.602 \cdot 10^{-19}$ C	Elementary charge.
1 eV	11605 K	Temperature corresponding to 1 eV.
1 eV	1240 nm	Wavelength corresponding to 1 eV.

1. GENERAL INTRODUCTION

This thesis belongs to the field of gas discharge physics or plasma physics, depending on the point of view. It is claimed that more that 95% of the Universe consists of plasma. While it is almost impossible to prove (or disapprove) this statement, it still points to the prevalence of plasma state and is widely used in introductory texts to plasma physics. The prevalence is mainly caused by stars, like Sun, which are all big 'balls of plasma'. Nevertheless, in everyday life we hardly see any device or appliance that utilizes matter in a plasma state for its operation. We know that integrated circuits use semiconductors for their operation, i.e. matter in a solid state; heat transmission systems use liquids or vapour – and there are numerous examples for matter in gaseous state. So is the realm of plasma physics strictly bound to the field of theoretical physics or are there new emerging applications still coming? While scientists may argue about the percentage of plasma in the Universe, one thing is undeniable – the number of appliances and technologies utilizing plasma in their work will certainly rise. As a matter of fact, nowadays, at least one third of the tens to hundreds of fabrication steps required for microchip production are typically plasma-based (Lieberman and Lichtenberg 1994). The absence of plasma around us is caused by the fact that in temperature ranges suitable for life matter cannot be in plasma state, but can be in solid, liquid or gaseous state. Only in limited cases, for example in a bolt of lightning, can matter be converted into plasma state, which quickly cools back to gaseous state. Therefore, special equipment needs to be designed to obtain and manipulate matter in plasma state.

As with every technology, before we can utilize it in a useful fashion, we need to be able to manipulate its characteristics in a way advantageous for the objective. This requires for models that adequately tie the useful properties to other commutable and selectable qualities. Scientists can only develop such models if they can obtain reliable and unambiguous measurements of the parameters incorporated in their models. Such parameters for solids may be conductivity, modulus of elasticity, temperature, etc. One can see that measuring these parameters does not have to be invariably complicated, and one can buy such equipment from many stores. Nevertheless, measuring parameters that describe plasma (plasma conductivity, temperature, local field strength, etc.) is somewhat different. The reason is that most sensors are themselves solids and inserting them into a plasma results in development of a sharp temperature /potential boundary, often referred to as plasma sheath. Interpreting such measurement results is complicated, since the effect of inserting the sensor or probe into the plasma has to be counteracted in the calculations. For some plasma parameters and for some situations this can be done quite successfully. In fact, the very first plasma measurements were done by using so-called Langmuir probes, which are still useful today for many applications.

The problem of measuring sensor affecting the measured quantity is not intrinsic to plasma physics, but can be encountered in many fields, just in plasma physics such problems are more pronounced. For example, imagine we are

trying to measure temperature of molten metal or temperature of a material possessing poor thermal conductivity. In the first case the sensor would melt, and in the second case we would obtain a reading which is closer to the initial temperature of the sensor rather than to the temperature of the investigated material. We know that such measurements could be carried out more successfully by using IR/non-contact thermometers or formerly pyrometers. These devices do not measure temperature but the emitted spectrum, from which the temperature of the explored surface is deduced. This deduction is only possible if the underlying processes and relations are well known to be thereafter implemented inside a microcontroller.

Current thesis explores the possibility of using a spectroscopic method for electric field strength determination in low-temperature gas discharges. Often the ratio of emission intensities, corresponding to $N_2^+ B^2\Sigma_u^+ \rightarrow X^2\Sigma_g^+$ (FNS) 0–0 (391.4 nm) and $N_2 C^3\Pi_u \rightarrow B^3\Pi_g$ (SPS) 0–0 (337.1 nm) transitions, is used for electric field strength estimation. The excitation threshold energies for the upper states of these bands differ considerably (11.0 eV and 18.7 eV) and, therefore, the ratio of emission intensities, $R_{\lambda 1/\lambda 2}$, is sensitive to comparatively small changes in the mean electron energy. This dependence can be used for electric field strength estimation in low-temperature gas discharges, if the excitation of nitrogen molecules from the ground state by electron impact is the dominant process (Kozlov *et al* 2001).

The value of knowing this relationship has both practical and theoretical benefits. It is, however, unlikely that a device will built to measure electric field strength in this way. By knowing electron energy distribution function, emission cross-sections for these transitions, their corresponding lifetimes and quenching rates, we can actually calculate the expected intensity ratio as a function of electric field strength. This has been previously done by several authors (Creyghton 1994, Djakov *et al* 1998, Kim Y *et al* 2003). The current investigation was inspired by the fact that the results of different authors diverge considerably and no experimental validation had yet been made.

The aim of the current thesis was to experimentally determine the relationship between the intensity ratio of the above-mentioned nitrogen bands and macroscopic electric field strength. As a result, the dependence of the intensity ratio on the field strength and pressure, $R_{391/337}(E/N,\ N)$, was determined experimentally in air for the first time in a wide range of E/N values (Paris *et al* 2004, 2005, 2006). The results show that the measured intensity ratio also considerably differs from the theoretical calculations of other authors. Probable reasons for discrepancies are put forth. The results obtained in this thesis are explained and presumed to be correct.

The first three chapters are addressed to a reader unfamiliar with the field of gas discharge physics. Chapter 2 and 3 serve as introductory texts to gas discharge physics and spectra of diatomic molecules with more emphasis on topics related to the current thesis. Chapters 4, 5 and 6 summarize the results obtained in this thesis and are presented in a more complex form, but the main outline should be clear even to a reader without any prior experience in this field.

2. BACKGROUND ON PLASMA CHARACTERIZATION

2.1. Introduction

The known matter, at least on Earth, is generally observed to be in one of its three states: solid, liquid or gaseous. It is the electromagnetic force that is responsible for creating these structures. Typically, at lower temperatures matter forms some kind of solid structure, like ice for example. By heating up the solids, at some temperature, the thermal energy of the solid becomes larger than the binding energy of the structure and, as a result, the solid transforms to liquid state i.e. the solid melts. By increasing the temperature further, the obtained liquid starts to vaporize, and if molecules vaporize from the surface faster than they re-condense, the liquid transforms to gas. By increasing the temperature yet further, the kinetic energy of the gas molecules becomes large enough for molecules to be ionized by collisions. The obtained substance, which may be partly or fully ionized, is generally referred to as *plasma* (Goldston and Rutherford 1995).

The term plasma comes from Greek, meaning formed or moulded, and was originally used to describe the fluid that remains after removing all the corpuscular material from blood. Irving Langmuir was the first scientist who in 1927 used this term to describe ionized gas. The reasoning behind this was probably the fact that in both cases there is some entertaining medium and some (two types of) particles immersed in it. However, if blood is cleaned of corpuscular material, there is actually some residue; but if we removed all the charged particles from fully ionized gas, we would also remove the entertaining medium, since this medium (electromagnetic fields) is produced by the charged particles themselves (Bellan 2006).

As we know, it is fairly simple to describe gas. For example, the Ideal Gas Law provides us the relations between gas temperature, pressure and volume. This is because we can treat each 'collision' as an independent process. What this 'collision' actually means is not all that important. We can modify or improve the Ideal Gas Law by adding terms that describe the 'collision' force as a function of distance between two colliding molecules and a term that describes the volume of molecules. The obtained result describes neutral gas even better, especially at higher pressures. The basic situation, however, has not changed – each particle moves independently of the others – energy and momentum are transferred from one particle to another only by collisions. But, if this neutral gas is even slightly ionized, significant changes to this simple description manifest themselves. The ionization degree can vary from 100% (fully ionized gases) to very low values (e.g. 10^{-4}–10^{-6}; partially ionized gases). Firstly, the liberated electrons and resulting ions 'feel' the force of the electric field and each such particle is a source of electric field itself, through which every charge exerts forces on any other charged particle in inverse square proportion to their separation. As every charged particle also creates a magnetic field, which exerts force on other particles, moving relative to that particular particle, the resulting effect produced by electric and magnetic fields can be described by Lorentz force (Braithwaite 2000). To

calculate the electromagnetic force acting on a single charged particle, the location, speed and direction of all the other charged particles must be known.

Usually, the number of charged particles under investigation is very large and to calculate the trajectory of charged particles under these circumstances some simplifying assumptions about these processes must be made. In that sense plasma science is not a precise science. It is rather a collection of different mathematical models and descriptions suitable for different situations (Bellan 2006). Typical simplifications/assumptions may be that the externally applied magnetic field is assumed to be zero, or that the magnetic field, generated by the charged particles, is also assumed to be zero – as is the case in this this work. There are numerous other simplifications that are often made, leaving a plasma scientist with a more manageable problem. Instead of following a single particle in plasma, particles are often grouped according to their properties, giving rise to forms of fluid theory. However, even after simplifications, the obtained equations are more often solved by numerical methods – only in limited cases can analytical solutions be obtained.

So, how are plasmas obtained? As explained previously, plasma is usually obtained when sufficient energy, higher than the ionization energy, is added to atoms of a gas, causing ionization and production of ions and electrons. As gas is already the closest state of matter to plasma, generally, plasmas are created from gases. Heating the gas to a sufficiently high temperature is more complicated. Hot gas will indeed ionize itself through kinetic energy of the random motion of particles, but since 1 eV is equivalent to a kinetic temperature of 11605 K, one would not expect much thermal ionization below a few thousand kelvin (Braithwaite 2000). Therefore, we cannot use standard heating methods, since the heater itself would melt before the gas becomes even slightly ionized. In practice, plasma is usually excited and sustained by using electricity in different forms: direct current, radio frequency, microwaves, etc. As even the air we breathe is always slightly ionized due to natural background radiation, we can accelerate those charged particles, which in turn will convey the obtained energy, via collisions, to other, still neutral particles. In this way quite high ionization degrees can be obtained, but as the plasma container walls still act as effective form of cooling, very high temperatures still cannot be reached. For high-temperature, or *fusion grade plasmas*, collisions between plasma particles and the walls of the plasma container must be avoided. This is achieved by using complicated magnetic field configurations and equipment (Grill 1994).

As plasmas are commonly produced by electrical discharges in gases, a term *gas discharge* is often used to describe specific forms of plasma. This term has a long history, dating back to 18th century, when Leyden jar (a capacitor in essence) was the main way of saving and using electrical energy. By discharging the Leyden jar through air, a transient effect can be witnessed, giving rise to 'gas discharge'. Leyden jar was replaced by Voltaic pile roughly a hundred years later, which allowed achieving continuous discharges. Since electron was discovered only about hundred years later, in 1897, the nature of those early discharges was poorly understood. The term plasma appeared still later. Typi-

cally, in gas discharges one obtains cold plasma which is not in thermal equilibrium. These terms are clarified in the following sections. In any case, historically, the term *gas discharge* is used to associate certain experimental techniques, processes and plasma types (Anders 2003). The concept of *gas discharge* is often used to refer to a process, while *plasma* is used to refer to a state of matter. Current thesis also falls into the category of gas discharges, but as the obtained substance fails to meet the strict requirements for plasma state, we refer to the discharge used in this work as a *gas discharge* and not as *plasma*. Generally, for *plasma physics* magnetic fields are important and cannot be ignored, but when one talks about *gas discharge physics* then magnetic fields can be ignored, though the processes involved may largely overlap.

The keywords describing plasma state are high conductivity as opposed to very low conductivity of typical gases. Typical gas particles have Maxwellian velocity distribution; plasma can have velocity distribution far from Maxwellian – the proportion of high-speed particles is larger for plasma. Since plasma does not exist in temperature ranges encountered in everyday life, people do not have a sort of intuition for plasma behaviour on the contrary to gases, liquids or solids. It is often claimed that plasma (structure) is very complex in essence. There exist other complex structures besides plasmas, like microprocessors for example, where different types of circuits are allocated and linked together forming a complex structure. The complexity of plasma is, however, somewhat different. In plasma the complexity is expressed not only spatially, but also, and more importantly, temporally. The linkage between the temporal and spatial behaviour of plasma is the principal source of plasma complexity (Fitzpatrick 1998).

2.2. Basic plasma parameters and concepts

2.2.1. Plasma species, degree of ionization and temperature

Typical gas discharge sustained in a mixture of molecular gases consists of number of different types of neutral and charged particles. A group of identical particles is commonly cited as (plasma) *species*. Most important parameters for any gas discharge or plasma are:

- particle number density;
- temperature corresponding to different species;
- the type, form and strength of externally applied electric and magnetic fields.

Charged particle number density is often expressed by the *degree of ionization*, φ, of the gas, which specifies the fraction of ionized particles in gaseous phase:

$$\varphi = \frac{\rho_-}{N} \approx \frac{\rho_+}{N}, \tag{2.1}$$

where ρ_- and ρ_+ denote positive and negative particle number densities. For

different particle species different densities may be defined. In this work we denote neutral particle number density by N, m^{-3}. Number density corresponding to different charged particles is denoted by ρ, m^{-3}. Particular species is denoted by adding corresponding subscript. Negative particles may be electrons and ions with a negative charge; positively charged particles are solely positive ions. For plasmas sustained in gas discharges, the degree of ionization generally ranges from 10^{-6} to 10^{-3}. If the discharge is confined by additional magnetic fields, then the degree of ionization may be much higher. In this work the degree of ionization is very low, of the order of 10^{-11}.

Temperature is more complicated term for plasma, as compared to gas, not only because we have to consider different species, but also, because the energy distribution function of the charged particles is often not Maxwellian. Temperature of charged particles, corresponding to different plasma types, may also differ several orders of magnitude. Typically, higher plasma temperature means higher degree of ionization. As electrons gain energy more easily from electric field they, in turn, energize other species by losing part of their energy through collisions. Heavy particles, on the other hand, obtain energy mostly from collisions with electrons and lose energy to the surroundings by radiation or by heat transfer to the walls of the container. At a first approximation, any discharge or plasma can be viewed as consisting of two subsystems: the first containing electrons and the second containing neutral atoms, molecules or molecular fragments and ions. The situation gets more complicated as heavy species often have different temperatures. For thermodynamic equilibrium to exist, all these temperatures have to be equal. For typical laboratory gas discharges this is hardly the case. However, under certain laboratory conditions it is possible to achieve local thermodynamic equilibrium in volumes of the order of free path length (Grill 1994). Under these circumstances the plasma is called *local equilibrium plasma* (*LTE plasma*). In typical gas discharges these conditions are rarely met and these plasmas are often referred to as *non-LTE plasmas* or *cold plasmas.*

Typically, at lower pressures electron temperature is much higher than the temperature of the gas, $T_e >> T$. At higher pressures the energy transfer from electrons to neutral particles increases and may reach equilibrium value for some discharge types. Although the electron temperature in non-LTE plasmas may reach 10^4 K, it does not mean that these plasmas are hot. Electron densities in these plasmas are low, and due to low density and low heat capacity of electrons the amount of heat transferred from electrons to the gas and, consequently, to the walls of the container is very small. The term *cold plasma*, therefore, derives its meaning from the small amount of heat transferred to the gas or solids in contact with it (Grill 1994). The type of discharge used in this work also falls into the category where $T_e >> T_i > T$.

Externally applied electric and magnetic fields can differ in many ways. Firstly, the frequency of the applied fields may differ several orders of magnitude, starting from zero (constant fields) and reaching up to optical frequencies, covering a vast dynamical range, each range having its own effects and appli-

cations. Secondly, the form of the applied fields may be very different. For example, the fields may be more or less homogenous. Since the number of possibilities is large, we retain ourselves to the framework of this thesis where $B = 0$ and $E = const$, i.e. typical gas discharges.

There are numerous other parameters (*Debye length*, *plasma frequency* etc.) that are used to describe plasma, which we do not define in this work. These parameters only become important when *plasma state* is actually achieved in a gas discharge, and are not essential in the context of this work. Strict definition of plasma states that the scale of the discharge must be greater than the screening distance (or *Debye length*) of the ionized matter. In the present work, however, this criterion is not met. Generally, though, many authors still refer to plasma with simplified meaning of 'ionized gas'.

2.2.2. Plasma classification and applications

Plasmas exist in natural form in cosmos and are created under unique conditions for specific purposes. Plasmas found in nature cover a very large range of electron densities and temperatures. Different plasma types can be classified by the basic plasma parameters, described in the previous section, and divided into three main groups (Bellan 2006):

- space plasmas;
- fusion-grade terrestrial plasmas;
- non-fusion terrestrial plasmas, i.e. gas discharges.

Parameters describing space plasmas cover an enormous range. Charged particle number densities in space plasmas can vary from 10^6 m^{-3} in interstellar space to 10^{20} m^{-3} in the solar atmosphere. Most of the astrophysical plasmas (solar winds, ionosphere and stars), that have been investigated, have temperatures in the range of 1–100 eV, and these plasmas are usually fully ionized. It is, however, very difficult to obtain large scale plasmas in practice that are dense and fully ionized, and so, we do not meet those plasmas in laboratory. The research into space plasmas was started in 1940s by Hannes Alfvén and continuous today by using advanced satellites and modelling techniques. Space plasmas do not have practical applications, other than the value of knowing and understanding the underlying principles of our Universe.

The investigation into fusion-grade terrestrial plasmas started in 1950s as a part of thermonuclear weapon research separately in different countries. After realizing that controlled fusion was unlikely to be of military value, several countries have since combined their research efforts. The plasma needed for controlled thermonuclear fusion requires electron temperatures above 10 keV (10^8 K) and ion densities around 10^{14} cm^3. These values are required in order to obtain the nuclear fusion reaction between deuterium and tritium atoms, as reasonable cross-sections for the fusion reactions are obtained only for energies above 5 keV. At the end of 1960s a magnetic confinement configuration called

tokamak was developed, which produced plasmas with parameters far better than devices of the previous decades. It was then thought that human race will harvest thermonuclear power as soon as in 1980s. History, however, showed that it is far more difficult to obtain fusion-grade plasma. The main problem in heating these plasmas is to prevent interaction of the energetic particles with the walls of the reactor. The interaction with the walls causes both loss of energy from the plasma and its contamination with particles sputtered from the walls of the plasma container (Bellan 2006). Since energy loss is proportional to plasma vessel surface area, but heat production rate is proportional to plasma (vessel) volume, it is more practical to use large containers for obtaining fusion-grade plasmas. To prevent plasma interaction with the walls, strong external magnetic fields must be applied. These are obtained by using superconductors and liquid helium. This makes these devices (*tokamaks*, *stellarators*) very large and expensive to manufacture and service. Therefore, there are only limited number of such devices available in the world. However, if one day fusion power is nevertheless harnessed, fusion grade-plasmas, undoubtedly, present most important practical application of plasma physics.

Non-fusion terrestrial plasmas differ from space plasmas and fusion-grade terrestrial plasmas in a number of ways. The most notable is scale. For space plasmas the scale is of the order of kilometres; for fusion-grade plasmas the scale is of the order of meters. Non-fusion terrestrial plasmas have typical scale of several centimetres, and these plasmas are usually sustained in gas discharges. Regardless of their small size, these plasmas have far more practical applications than the types described previously. Non-fusion terrestrial plasmas can be further divided into two subgroups.

- Non-fusion terrestrial plasmas, i.e. gas discharges:
  - hot plasmas or LTE plasmas, for which $T_e \approx T_i > T$;
  - cold plasmas or non-LTE plasmas, for which $T_e >> T_i \approx T$.

In general, the first subgroup combines plasmas that are more or less in thermal equilibrium, and the second those which are not in thermal equilibrium. Most space and fusion-grade plasmas, described previously, are in thermal equilibrium. For thermal equilibrium many collisions are needed. As collision frequency increases with pressure, thermal equilibrium is more easily achieved at higher pressures. High gas pressure implies many collisions in the plasma, leading to an efficient energy exchange between the plasma species and, hence, equal temperatures. The number of collisions between particles also increases, as the scale of plasma increases, because charged energetic particles collide more with less energetic cold species before moving out of the scope of plasma. Therefore, it is understandable why in space and fusion-grade plasmas thermal equilibrium is more easily achieved. Non-fusion hot LTE plasmas, sustained in gas discharges, are also more easily obtained at higher, atmospheric, pressures and larger scales. LTE plasmas, which are characterized by rather high temperatures, are often used for applications where heat is required, such as for

cutting, spraying and welding (Bogaerts *et al* 2002). Temperatures in these plasmas can easily reach up to 30000 K. The discharge types for sustaining LTE plasmas include *electric arcs* and *plasma jets*.

In low-pressure and small-scale discharges thermodynamic equilibrium is not reached, even at a local scale. Such non-LTE plasmas are often used for applications where heat is not desirable, for instance etching or for deposition of thin layers. The heavy particle temperature is low, often not much higher than room temperature, but the electron temperature is much higher, because they are light and easily accelerated by the applied electromagnetic fields. High electron temperature gives rise to inelastic electron collisions, which sustain the plasma in a chemically-rich environment. Electrons are, therefore, considered to be the primary agents in the plasma. Most of the applications, on the other hand, result from the heavy particle kinetics, e.g. sputtering, deposition, ion implantation (Bogaerts *et al* 2002). One may think that the large temperature difference is a disadvantage and we should always aspire towards thermal equilibrium. Actually, this is not the case. Low temperature of the heavy species is an important advantage of non-LTE plasmas, and there are currently far more applications for non-LTE plasmas than for LTE plasmas. Non-LTE plasmas are also the main subject of gas discharge physics.

In recent years the field of gas discharge plasma applications has rapidly expanded. This is due, among other things, to the large chemical freedom offered by the non-equilibrium aspects of the non-LTE plasmas. Wide variety of chemical non-equilibrium conditions is possible, since external control parameters can easily be modified.

- Parameters to be varied in cold or non-LTE plasmas:
  - the chemical input, i.e. working gas which defines different species in the plasma: electrons, atoms, molecules, ions, radicals, clusters;
  - gas pressure, p;
  - electromagnetic field strength and structure.

In non-LTE plasmas electron temperature, T_e, can reach temperatures up to 10^4 K, while temperature of the gas, T, may be as low as room temperature, $\sim 10^2$ K. By applying different combinations of the listed parameters, variety of non-LTE plasmas can be obtained. For example, different charged radical densities can be obtained and then accelerated by electric fields into the substrate. The low temperature of the heavy species guarantees that little heat is transferred to the substrate, preventing it from melting. The technological applications of non-LTE plasmas are numerous and include thin film deposition, semiconductor processing, materials treatments (modification of surface physics and surface chemistry, sterilization), lamps, light sources and displays, thick film deposition, waste treatment and material analysis (Lieberman and Lichtenberg 1994).

Current thesis also falls into the category of cold or non-LTE plasmas. Typically, for investigative purposes more simple forms of discharges are used than

for industrial manufacturing purposes. For obtaining non-LTE plasmas many different forms of discharges exist. For example, if E is homogenous, but the discharge current is not limited, *glow discharge* or *arc discharge* may develop. These discharge types are each vast areas of research. One may wonder, how it is possible that such small changes in externally applied parameters would result in fundamental changes in the form of the discharge. The reason is that each discharge is actually a balance between numerous nonlinear processes, including external electric fields and the electric fields created by charged particles in the discharge, which are in turn bound to the production and loss mechanisms of these charged particles. Small change in one of these parameters can, therefore, result in an entirely different point of balance between these processes.

The discharge used in this thesis, called *dark discharge* or *Townsend discharge*, is obtained under conditions where externally applied field, E, is homogenous and constant. Current density is kept very low, ensuring that $E >> E_\rho$. In the present work the chemical input mainly includes mixture of N_2 and O_2. Gas pressure, p, is kept between 1–760 Torr (~ 10^2–10^5 Pa). Dark discharge does not have any practical applications in industry, but it has become indispensable for research purposes as a medium that is simple to describe mathematically.

2.2.3. Basic quantities and phenomena

One of the most important quantities for describing gas discharges may be obtained by dividing the absolute value of electric field strength, E, by gas number density, N. The obtained relation is usually referred to as *reduced electric field strength*, E/N, and is often measured in units of Td (Townsend), where 1 Td = 10^{-21} V·m^2. This relation describes the amount of energy an electron typically absorbs from the applied electric field between collisions. One can see that this energy remains invariable if we, for example, doubled both, E and N. The mean free path between collisions would decrease two times, but an electron would gain the same amount of energy, since E has been doubled also. Because the energy of the colliding particles determines the probability of a particular collisional process to occur, E/N is a kind of invariant in gas discharge physics. Many other quantities, intrinsically related to collisions, are often expressed as a function of the reduced electric field strength, E/N, including the most important results of this thesis.

The unit, Td, is named after Irish physicist John Sealy Edward Townsend (1868–1957) who conducted various studies concerning the electrical conduction of gases. He was the first physicist who, after the discovery of electron, was able to explain the basic relations between the applied parameters and the observed effect, producing equations that were also scalable. These equations are still useful today – we will discuss some of these shortly.

In gas discharges E/N is generally between 10–1000 Td (10^{-20}–10^{-18} V·m^2). For lower reduced electric field strengths the loss rate of charged particles is often greater than the production rate; at higher E/N values it is more complicated to control the discharge by external parameters. Since the measured quantities in typical gas discharges are gas pressure, p, and temperature, T, the reduced electric field strength can be conveniently found from:

$$E/N = k_{\mathrm{B}} \cdot \frac{E \cdot T}{p}. \tag{2.2}$$

Generally, though, the input power that is used to maintain the discharge rises gas temperature. Charged particles in the discharge, in their turn, distort the applied electric field in a ways that is complicated to describe mathematically. This makes formula (2.2) quite useless for typical plasmas and gas discharge configurations. However, this formula can still be used, if we know the strength of the externally applied homogenous electric field, and this field is much stronger than the collective electric field created by charged particles in the discharge. Also, the energy input into the discharge must be small enough for gas temperature to remain unchanged. In this case we can use discharge container or room temperature in formula (2.2). Only (Townsend) dark discharge, used in this study, satisfies these requirements. This type of discharge is named, similarly to Td, after physicist John Sealy Edward Townsend, indicating to a long history of this type of discharge. The word 'dark' implies that there are no visual effects involved, and the discharge remains dark for human eyes. This does not mean that there is no optical emission present. The discharge can be easily visualized using high sensitivity camera, as can be seen in figures 6.1 and 6.2, where selected pictures of the discharge, taken by the author of this work, are presented.

It is often inconvenient to describe the motion of charged particles in gas discharges by taking into account all the possible (collisional) processes. As the number of possible processes is very large, it is more customary to use quantities that describe the processes under interest in a more general manner. Most important of these quantities in gas discharge physics is the *mobility*, μ, m^2/V·s. Mobility can be defined separately for each charged particle species. For zero electric field strength, $\boldsymbol{E} = 0$, the charged particles only follow random thermal motion, characterized by corresponding distribution function. If an electric field is present, an additional collective motion, called *drift* of charged particles, manifests itself. Mobility is defined as the coefficient of proportionality between the *drift velocity*, $\boldsymbol{v}$, of a charged particle species and the electric field strength:

$$\boldsymbol{v}(E/N) = \mu \cdot \boldsymbol{E} = \mu N(E/N) \cdot E/N. \tag{2.3}$$

Mobility describes the 'frictional force' applied to charged particle species by other particles in the discharge. It is basically the sum of all the possible collisional processes, resulting in a drag that prevents charged particles to be infi-

nitely accelerated and for a balancing force to develop between the accelerated (charged) species and background (neutral) species. For zero electric field strength drift velocity is zero, meaning there is no net current. If an electric field is present, an electrical current arises. Typically, the measured current is the sum of all the currents produced by different charged particle species. Because electron mass is much smaller than the mass of ions, the mobility of electrons is also much higher than the mobility of ions, so the most prominent current component is often the current related to the motion of electrons. To divide the measured current into different components and distinguish the electron current from the current produced by different ion species, we have to know how the number of electrons is related to the number of ions. For this we have to know the production and loss rates of different charged species, which is the subject of next sections.

Experimental evidence shows that mobility is not a constant. Mobilities are often determined experimentally for a specific gas and presented in the form $\mu N(E/N)$, so that drift velocity becomes a function of E/N. This is because the drift velocity is intrinsically related to collisions.

Diffusion of charged species, which is fundamentally different from diffusion of neutral species, is another parameter related to the transport properties of gas discharges. In this work diffusion does not produce any observable effects, and does not influence the measured parameters in any measurable way, so we omit further discussion of diffusion here. The reason is that other processes, like attachment for example, disperse charges more than diffusion.

2.2.4. Electron energy distribution function

In addition to collective motion, characterised by drift, particles in the discharge also have a random thermal motion, characterised by corresponding velocity or energy distribution function. Neutral gas particles typically have Maxwellian velocity distribution, corresponding to the maximum entropy of the system. Charged particles in plasma, however, can have velocity distribution different from Maxwellian, with higher proportion of high-energy particles. As different process (ionization, excitation, etc.) rates depend strongly on electron energy, i.e. have threshold energies, the choice of proper distribution function is of utmost importance. This is one of the fundamental problems in gas discharge and plasma physics.

The particle *velocity distribution function*, $f(v)$, is defined as the number density of particles in the velocity space that satisfies the equation (Grill 1994):

$$\rho = 4\pi \int_0^\infty f(v) \cdot v^2 dv \,. \tag{2.4}$$

Here v denotes velocity (not to be confused with *drift velocity*), $f(v)$ is velocity distribution function, and ρ denotes particle number density. If it is assumed

that the velocity distribution of the electrons in the plasma is isotropic and that the effects of inelastic collisions act only as a perturbation to the isotropy and the effects of the electric fields are negligible, then the velocity distribution is Maxwellian:

$$f(v) = \rho_{\mathrm{e}} \left(\frac{m_{\mathrm{e}}}{2\pi k_{\mathrm{B}} T_{\mathrm{e}}} \right)^{\frac{3}{2}} \exp\left(-\frac{m_{\mathrm{e}} v^2}{2 k_{\mathrm{B}} T_{\mathrm{e}}} \right), \tag{2.5}$$

where m_{e} denotes electron mass. The *electron energy distribution function* (EEDF), $f(W)$, is related to the velocity distribution function, $f(v)$, trough relation:

$$f(W) = \frac{4\pi}{m_{\mathrm{e}}} \cdot v \cdot f(v) \,. \tag{2.6}$$

Maxwellian electron energy distribution function, $f_{\mathrm{M}}(W)$, can be expressed as:

$$f_{\mathrm{M}}(W) \approx 2.07 \cdot {W_{\mathrm{mean}}}^{-\frac{3}{2}} \cdot W^{\frac{1}{2}} \cdot \exp\left(-\frac{1.5 \cdot W}{W_{\mathrm{mean}}} \right). \tag{2.7}$$

The mean electron energy, W_{mean}, is related to electron temperature, T_{e}, by:

$$W_{\mathrm{mean}} = \frac{3}{2} k_{\mathrm{B}} T_{\mathrm{e}} \,. \tag{2.8}$$

Due to the simplifying assumptions, the Maxwellian distribution provides only a first approximation of the EEDF in typical low-temperature discharges. The assumptions made for the Maxwellian distribution can be replaced in cold plasmas by the following assumptions:

- the electric field strength, E, in the discharge is sufficiently low, such that one can neglect the inelastic collisions, but large enough for the electron temperature to be much higher than the ion temperature, T_{i};
- the frequency of the electric field, E, is much lower than the frequency of collisions;
- the collision frequency is independent of the electron energy.

Under these assumptions the EEDF in the discharge is given by the Druyvesteyn distribution, $f_{\mathrm{D}}(W)$:

$$f_{\mathrm{D}}(W) \approx 1.04 \cdot {W_{\mathrm{mean}}}^{-\frac{3}{2}} \cdot W^{\frac{1}{2}} \cdot \exp\left(-\frac{0.55 \cdot W^2}{{W_{\mathrm{mean}}}^2} \right). \tag{2.9}$$

The Druyvesteyn distribution function gives a better approximation than the Maxwellian distribution in non-LTE discharges. However, if the degree of ionization, φ, is high, the electron number density also affects the energy distribution. For

typical plasmas both distribution functions give only approximation, and better results are often obtained by numerical calculations (Grill 1994).

In Appendix A Maxwellian and Druyvesteyn distribution functions are calculated for $W_{\mathrm{mean}} = 4.5$ eV and $W_{\mathrm{mean}} = 8.1$ eV, corresponding to about 165 Td and 395 Td in air. The Druyvesteyn distribution is characterized by a shift toward higher electron energies, as compared to Maxwellian. In general, reactions in gas discharges have an energetic threshold, and only happen if the energy of the colliding particles (electrons) is higher than the threshold value. Thus, reaction rates are very sensitive to the high-energy tail of the distribution function. The high-energy tails of the distribution functions are rather different for the same mean electron energies and, therefore, different distribution functions provide us different reaction rates.

Heavy charged species also have their energy distribution function, but since electrons are more directly responsible for most of the reactions, the electron energy distribution function, EEDF, is the most important. There are some processes that are related to collisions between heavy species, like *Penning effect* for example, but the reaction rates of these processes primarily depend on how high is the concentration of these (excited) heavy particles, which in turn primarily depends on EEDF. Therefore, the EEDF is of primary importance in gas discharge and plasma physics.

Similarly to drift velocity, the mean electron energy can be expected to be a function of the reduced electric field strength, E/N, i.e. $f(E/N, W)$. However, as with drift velocity, there is no simple relation between E/N and W_{mean}. These relations are determined experimentally for a specific gas or obtained by numerical calculations. This topic is shortly discussed in section 2.3.5.

2.3. Fundamental collisional processes

2.3.1. Production and loss of charged or excited particles

When two or more particles collide various processes may occur. By far the most common encounter in gas discharges is between pairs of particles (*binary collisions*). The production of charged or excited particles may be solely contributed to collisions. The subsequent loss of these particles can happen in two ways: by a subsequent collision or by a spontaneous loss (excited particles). Collisions can be further divided into two groups: collisions between particles and collisions between particles and surfaces (electrodes and container walls).

- Collisions between particles. Such collisions are described by a quantity called the *cross-section* (σ, m^2) of that process. Collisions between particles may be further divided into three clearly different cases:
  - collisions between neutral (heavy) particles;
  - collisions between charged particles;
  - collisions between neutral and charged particles:

    - collisions between heavy particles i.e. ions and neutrals,
    - collisions between neutrals and electrons.
- Spontaneous loss of excited particles. This process is common for excited particles but also for negative ions. Such processes are described by a quantity called the *time constant* (τ, s).
- Collisions between particles and surfaces. These processes are usually tackled by calculating particle flux onto a surface from *particle flux* density ($\boldsymbol{\Gamma}$, $m^{-2} \cdot s^{-1}$).

Collisions between neutral heavy particles in low-temperature gas discharges do not produce new excited or ionized species, since the kinetic energy of these particles is typically below 0.1 eV. For ionization, dissociation or excitation of electronic states commonly energies of several eV are needed. Therefore, these collisions are *elastic* in essence – no change in total kinetic energy. However, if one of the colliding particles is in excited state, then the energy corresponding to an excited state may be transferred to kinetic energy of the particles and the excitation is effectively quenched. Such processes are commonly referred to as *quenching* or *collisional deactivation* of an excited state.

Certain excited states do not satisfy selection rules for electric dipole radiation, though other radiative or radiationless transitions may still occur. These mechanisms are generally weak, leading to lifetimes that are long, of the order of microseconds (Lieberman and Lichtenberg 1994). These excited particles are called *metastable particles* or shortly *metastables*. Collisions with metastable particles can result in a transfer of the excitation from metastable particle to another particle, if the corresponding energy levels are energetically close to each other. This process is known as the *Penning effect.* For example, in He-Ne gas lasers excited Ne atoms that subsequently radiate are created by metastable He atoms. Metastables can also be important source of ionization among species where the ionization energy of one species is lower than the excitation energy of another, metastable, species.

Unlike collision between neutral particles, collisions between charged particles are described by long-range Coulomb interaction ($F \sim 1/x^2$). In theory one charged particle can influence the other from very long distances, but since other charged species tend to counterbalance that field, a limiting distance develops. In this work the degree of ionization is very low, of the order of $\varphi \sim 10^{-11}$, and collisions between charged particles can be excluded, so we omit further discussion of collisions between charged particles.

By far the main collisional processes in *weakly ionized discharges* are between charged and neutral particles. Therefore, the most important aspects of such discharges, and consequently this work, are related to collisions between neutral and charged particles, which can be further divided into two cases. One involves collisions with ions and the other collisions with electrons. Because ions have approximately the same mass as neutral species, and in collisions between equal mass particles the more energetic particle (ion) can lose up to half of its

kinetic energy in a single collision, ions rapidly exchange energy with neutrals and tend to be in thermal equilibrium with the neutrals. Since $T_i \approx T < 0.1$ eV, ion-neutral collisions should not be expected to be responsible for ionization or excitation of electronic states. In this sense, such collisions are similar to collisions between neutral species, described previously. Processes that are related to collisions between neutral particles and ions include (resonant) charge transfer, oligomerization and others. We do not describe these here, but move on to the processes directly related to the results of this work. This does not mean that such processes do not take place in the discharge used in this work, but rather that these processes take place quite independently of the processes important in the context of this work.

The most important processes in weakly ionized discharges are the processes related to collisions between neutrals and electrons. Electrons, with mass m_e, cannot lose much energy elastically to heavier particles, with mass M, – at best only a fraction $2m_e/M \approx 1/40000$. Therefore, electron temperature remains much higher. Electrons can, however, lose virtually all their kinetic energy through *inelastic* collisions with heavier particles. Such processes are the main sources of excitation and ionization in weakly ionized gas discharges. In discharges sustained in molecular gases such processes include:

$$\mathrm{e} + \mathrm{AB} \rightarrow \mathrm{AB}^+ + 2\mathrm{e}\,, \tag{2.10}$$

$$\mathrm{e} + \mathrm{AB} \rightarrow \mathrm{A}^+ + \mathrm{B} + 2\mathrm{e}\,. \tag{2.11}$$

The second process is called *dissociative ionization*, and it typically needs higher impact energy. For discharges sustained in mixtures of N_2 and O_2, as in this work, these processes become:

$$\mathrm{e} + \mathrm{N_2} \overset{> 15.6\ \mathrm{eV}}{\rightarrow} \mathrm{N_2^+} + 2\mathrm{e}\,, \tag{2.12}$$

$$\mathrm{e} + \mathrm{N_2} \overset{> 24.5\ \mathrm{eV}}{\rightarrow} \mathrm{N^+} + \mathrm{N} + 2\mathrm{e}\,, \tag{2.13}$$

$$\mathrm{e} + \mathrm{O_2} \overset{> 12.5\ \mathrm{eV}}{\rightarrow} \mathrm{O_2^+} + 2\mathrm{e}\,, \tag{2.14}$$

$$\mathrm{e} + \mathrm{O_2} \overset{> 20.0\ \mathrm{eV}}{\rightarrow} \mathrm{O^+} + \mathrm{O} + 2\mathrm{e}\,. \tag{2.15}$$

From presented threshold energies (Braithwaite 2000) one might conclude that the mean electron energy, W_{mean}, must be of the order of ten eV for these reactions to occur. Actually, to obtain weakly ionized plasma, only the tip of the high-energy tail of the EEDF must reach these values. So, the mean electron

energy may be as low as a few eV for these reactions to take place in typical gas discharges. The second thing to notice about the threshold energies is that the processes related to oxygen have lower thresholds. Therefore, one might expect that the same degree of ionization, φ, could be obtained in oxygen at lower W_{mean} values and, consequently, at lower E/N values. This conclusion is, however, deceptive. The degree of ionization also depends on processes related to loss of charged particles. These processes are more pronounced for electronegative gases, like oxygen, and surfaces. Such processes are discussed in subsequent sections.

To develop a mathematical description of collisional processes, we first consider the following differential equation, where $\rho_{\mathrm{e}}(x)$ denotes incident electron number density:

$$\frac{d\rho_{\mathrm{e}}(x)}{dx} = -\sigma \cdot N \cdot \rho_{\mathrm{e}}(x)\,. \tag{2.16}$$

The decrease rate of these electrons that have not yet collided is proportional to incident electron number density and also to background gas number density, N. The coefficient of proportionality in (2.16) is called the *cross-section* of a particular collisional process. Solution to this equation yields:

$$\rho_{\mathrm{e}}(x) = \rho_{\mathrm{e0}} \cdot \exp(-\sigma \cdot N \cdot x)\,. \tag{2.17}$$

Here ρ_{e0} denotes incident electron number density at x = 0 m. Quantity $1/\sigma{\cdot}N$ corresponds to the distance for which the uncollided electron number density has decreased exp(1) ≈ 2.718 times, and it is named the *mean free path* for the decay. Experimental evidence shows that cross-section is not a constant but a function of incident electron energy, i.e. $\sigma(W)$. Note that the cross-section is a function of energy of a particular collision, not W_{mean}, which can be viewed as a result of many such collisions.

Selected cross-sections for electron collisions with N_2 are presented in Appendix A. The presented ionization cross-section corresponds to process (2.12). One can see that below 15.6 eV this ionization cross-section equals zero, and from equation (2.16) we can conclude that the decrease rate of incident electrons giving rise to process (2.12) is zero if the incident electron energy remains below 15.6 eV.

Another way to describe binary collisions is by considering the rate of change in time. Let $\rho^*(t)$ denote excited particle number density. The change in number density can be described by the following differential equation:

$$\frac{d\rho^*(t)}{dt} = -k_1 \cdot \rho^*(t) - k \cdot N \cdot \rho^*(t)\,. \tag{2.18}$$

This equation (2.18) has the following solution:

$$\rho^*(t) = \rho_0^* \cdot \exp\left(-\frac{t}{\tau}\right), \tag{2.19}$$

where

$$\frac{1}{\tau} = k \cdot N + k_1; \;\; k_1 = \frac{1}{\tau_0}. \tag{2.20}$$

Here τ denotes the time during which the number density decreases exp(1) ≈ 2.718 times. k_1 (s^{-1}) is named the *first-order rate constant* and k (m^3/s) the *second-order rate constant*. τ_0 is often called the *natural lifetime* of an excited state. The first term, related to k_1, describes spontaneous processes. The second term depends on N and may be related to collisions. If k or N equals zero then $\tau = \tau_0$, i.e. if particles are not removed by collisions then the actual lifetime equals the natural lifetime. This is inherent to excited particles which can spontaneously radiate. In this work we denote the second-order rate constant related to quenching of excited states by k_q. The second term may describe the rate of change of excited particles, but also other particle species, like electrons. If both terms are non-zero then $\tau < \tau_0$.

Both rate constants can be, in principle, determined by experimentally measuring the rate of change of excited particles, described by (2.18), since the decay of excited particles is often accompanied by photon emission. In this work natural lifetimes and quenching rate constants of $N_2(C^3\Pi_u, v' = 0)$ and $N_2^+(B^2\Sigma_u^+, v' = 0)$ states are determined exactly in this way.

The second term in equation (2.18) may be related, in addition to loss of excited particles, also to production of new particles, like electrons. One can notice that differential equations (2.16) and (2.18) are similar in essence – one is related to distance and the other is related to time. The link between these equations is, apparently, incident particle velocity, v. Consider an incident mono-energetic electron beam with velocity v. Omitting spontaneous processes, i.e. $k_1 = 0$, we can write $k = \sigma \cdot v$. This formula can be only used if all the colliding particles have the same velocity, which is rarely true in typical gas discharges. Substituting velocity with energy of incident electrons, and employing EEDF instead of constant velocity, we can write:

$$k(E/N) = \left(\frac{2}{m_e}\right)^{\frac{1}{2}} \int_0^\infty f(E/N, W)\, W^{\frac{1}{2}}\, \sigma(W) \mathrm{d}W\,. \tag{2.21}$$

Since cross-section is a function of impact energy, we have to integrate over the whole scope of the EEDF. For example, to obtain the rate constant for process (2.12), $k_{2.12}(E/N)$, at 165 Td, we have to evaluate expression (2.21) using EEDF for 165 Td and the corresponding ionization cross-section. Note that $k(E/N)$ is only non-zero if EEDF and $\sigma(W)$ have an overlapping non-zero energy domain.

As was noted in previous section, EEDF, $f(E/N, W)$, is often not known. This is also true for $\sigma(W)$. Even if the uncertainties related to $f(E/N, W)$ and

$\sigma(W)$ are small, the resulting uncertainty related to $k(E/N)$ may be very large. This is true, since the result of (2.21) describes the product of $f(E/N, W)$ and $\sigma(W)$ in overlapping energy domain, which is very sensitive to the high-energy tail of the EEDF. In conclusion, the rate constant of a collisional process can be calculated from (2.21), but the obtained result may be considered reliable only if $f(E/N, W)$ and $\sigma(W)$ are well known.

Historically, individual processes and their corresponding cross-sections were poorly known, and another quantity was often used to mathematically describe the production of new electrons. It is called the *first Townsend coefficient* or *ionization coefficient*, α (m^{-1}). It describes the mean number of ionizing collisions per electron per unit drift path length, and it is the reciprocal of ionization free path length. It is the coefficient of proportionality in the following differential equation:

$$\frac{d\rho_e(x)}{dx} = \alpha \cdot \rho_e(x) \,. \tag{2.22}$$

Ionization coefficient offers a way for describing all the processes responsible for production of new electrons by a single coefficient. From equations (2.16) and (2.22) we could, somewhat incorrectly, conclude that the ionization cross-section equals α/N. However, the difference between these equations is that σ is related to a particular process, but α is related to actual ionization, which is usually the sum of many such processes. Ionization coefficient, corresponding only to a single process, for example (2.12), is related to respective rate constant through relation $\alpha_{2.12}/N_{N2} = k_{2.12}(E/N)/v_e(E/N)$. In conclusion, cross-section is a function of energy of a particular collision, but α/N can be expressed as a function of E/N, i.e. $\alpha/N(E/N)$. This means that α, unlike σ, can be used independently of the EEDF.

Formerly, ionization coefficients for different gases and experimental conditions were experimentally measured and the obtained results were published, so that others could utilize the results in their research. Often the following semiempirical formula was used to approximate the obtained data:

$$\alpha/N\,(E/N) \approx A \cdot \exp\left(-\frac{B}{E/N}\right). \tag{2.23}$$

Coefficients for gases used in this work are presented in table 2.1. Since only two coefficients, A and B, are used to approximate the data, formula (2.23) produces valid results only in a limited range of E/N values. A short overview of approximation formulas for ionization coefficient in air is presented in our latest paper (Plank *et al* 2014). Note that $\alpha/N(E/N)$ is very sensitive to E/N. This is caused by the fact that at some E/N value the high-energy tail of the EEDF reaches the threshold ionization energy of processes responsible for producing new electrons. In air these processes include (2.12–2.15).

Table 2.1. Constants for calculating ionization coefficient in nitrogen, air (21% O_2; 79% N_2) and oxygen. By using the values shown in parentheses, formula (2.23) produces $\alpha/N(E/N) - \eta/N(E/N)$ not $\alpha/N(E/N)$ in a very limited E/N range of 200–400 Td. [1]—numerically calculated with BOLSIG+; [2]—Raju 2006; [3]—Morrow 1985.

Gas	A, m^2	B, V·m^2	E/N range, Td
N_2	$4.55\cdot10^{-20}$ ($4.55\cdot10^{-20}$)	$12.0\cdot10^{-19}$ ($12.0\cdot10^{-19}$)	500–1500 [1]
Air	$4.66\cdot10^{-20}$ ($4.6\cdot10^{-20}$)	$11.3\cdot10^{-19}$ ($11.4\cdot10^{-19}$)	500–2480 [2]
O_2	$2.12\cdot10^{-20}$ ($2.0\cdot10^{-20}$)	$6.21\cdot10^{-19}$ ($6.5\cdot10^{-19}$)	400–800 [3]

2.3.2. Processes involving negative ions

When an electron collides with a neutral atom or molecule of an *electronegative gas* the electron can become attached to this atom or molecule and form a negative ion. Electronegative gases include O_2, NO_2, etc. Processes involving negative ions are important in discharges which include electronegative species. In nitrogen–oxygen mixtures there are two clear cases of negative ion formation:

dissociative attachment: $\mathrm{e} + \mathrm{O_2} \rightarrow \mathrm{O^-} + \mathrm{O}$; (2.24)

three-body attachment: $\mathrm{e} + \mathrm{O_2} + \mathrm{M} \rightarrow \mathrm{O_2^-} + \mathrm{M}$ ($\Delta W \approx 0.43$ eV). (2.25)

Here the third particle is denoted by M, which in this work can be N_2 or O_2. The energy difference, ΔW, is called *affinity*. This means that process (2.25) is exothermic with energy of about 0.43 eV. A stable negative ion, O_2^-, exists, if its ground state has a potential minimum that lies below the ground state of O_2. In an *electropositive gas*, such as N_2, affinities are negative, and N_2^- and N^- cannot form (Lieberman and Lichtenberg 1994).

Similarly to ionization, attachment of free electrons in the discharge is related to numerous processes that may not be exactly known. A common quantity, incorporating all these possible processes, is called the *attachment coefficient* or the *second Townsend coefficient*, η (m^{-1}). It is the coefficient of proportionality in the following differential equation:

$$\frac{d\rho_e(x)}{dx} = -\eta \cdot \rho_e(x) \,. \tag{2.26}$$

It describes the mean number of attachments per electron drifting 1 m in the opposite direction of the electric field.

Negative ions in the discharge may interact with gas molecules leading to the detachment of the electron or to the exchange of the negative charge (Badaloni

and Gallimberti 1972). In air discharges the dominant process in E/N values over 60 Td is (2.24) and below 50 Td is (2.25) (Pancheshnyi 2013). Therefore, in this work η is predominantly related to process (2.24). These, unstable, ions can further lose their negative charge by associative detachment:

$$O^- + N_2 \rightarrow N_2O^{-*} \rightarrow NO_2 + e\,, \tag{2.27}$$

or be converted into more stable O_2^- ions via charge transfer:

$$O^- + O_2 \rightarrow O_3^{-*} \rightarrow O_2^- + O\,. \tag{2.28}$$

The presented list of processes is by no means definitive. At different E/N ranges different processes may become important. At higher pressures the significance of three-body processes increases. To also take into account processes related to *detachment* and *conversion*, more parameters, in addition to α and η, are often used. The first is named *detachment coefficient*, δ (m^{-1}), for auto-detachment and collisional detachment, and it is defined as the mean number of detachment processes per unstable negative ion in a time electron drifts 1 m in the opposite direction of the electric field. The second is called *conversion coefficient*, β (m^{-1}), and it is defined as the number of conversion processes per unstable negative ion in a time an electron drifts 1 m in the opposite direction of the electric field (Wen 1989). Similarly to ionization coefficient, for binary collisions, η/N, δ/N and β/N can be expressed as a function of E/N. For three-body processes, as (2.25), η/N is a function of N and E/N.

The real and apparent increase rates in electron number density are related by (Wen 1989):

$$(\alpha - \eta)_{\text{apparent}} = (\alpha - \eta)_{\text{real}} + \frac{\eta \cdot \delta}{\delta + \beta}\,. \tag{2.29}$$

If the detachment coefficient, δ, is zero, i.e. all the attached electrons stay attached, the last term in relation (2.29) becomes zero, and there is no difference between apparent and real values. Similarly, if ion conversion rate is high and all unstable negative ions are quickly converted to stable negative ions, there is no difference between apparent and real values. Otherwise, apparent ionization is higher than the real ionization, since some new electrons are added to the discharge via detachment from negative ions.

For electronegative gases equations (2.22) and (2.26) can be combined and, instead of $\alpha - \eta$, the total rate of change in electron number density is determined by the apparent increase rate. If this rate is negative, then free electrons are effectively removed from the discharge. The critical electric field corresponding to zero net ionization is obtained, if the apparent increase rate in electron number density equals zero. In dry air at atmospheric pressure this field

is about 90 Td (Pancheshnyi 2013). Although the EEDF may reach the ionization threshold values for processes (2.12–2.15) at 90 Td in dry air, these newly created free electrons are removed from the discharge by attachment.

From table 2.1 we can see that as the oxygen concentration increases, α obtained from formula (2.23) increases (B decreases). This is exactly what might be expected from processes (2.12–2.15), since the ionization threshold energies are lower for oxygen. By using the values presented in parentheses, instead of α, formula (2.23) produces the apparent increase rate. In that case the increase in oxygen concentration produces lower values, since the removal of electrons increases (B increases). Of course, there is no difference for N_2. More recent formulae for apparent ionization are presented in Pancheshnyi 2013.

To correctly describe temporal behaviour of electron production in the discharge, a more complicated set of differential equations has to be solved, as compared to (2.22) and (2.26), since drift velocities of different ion species and electrons differ. This topic is further discussed in section 5.1.

2.3.3. Three-body processes

There is a group of processes that can happen only if three particles collide. Three-body processes are often viewed as two consecutive processes, related to binary collisions. The first collision produces a complex state, which needs immediate collision with a third body. For example, processes (2.25) is a three-body processes. To describe such processes, differential equation (2.18) must be modified to include a term which takes into account collision between three particles:

$$-k_3 \cdot N^2 \cdot \rho^*(t)\,. \tag{2.30}$$

Solution to this equation has a form of (2.19), but the natural lifetime, τ_0, and the actual lifetime, τ, are related through relation:

$$1/\tau = k_3 \cdot N^2 + k \cdot N + k_1\,. \tag{2.31}$$

Here k_3 (m^6/s) is called the *third-order rate constant* which describes collisional processes between three particles. The term that describes collisions between two particles is related linearly to gas number density, but for three-body collisions this term is proportional to N^2. Notice that relation (2.20) has the following form: $y(x) = a{\cdot}x + b$. Therefore, if we plot $1/\tau$ against N (or p) the natural lifetime equals the reciprocal of the intercept of the (regression) line and the quenching rate constant, k_q, of the process can be obtained from the slope of that same line. To obtain the necessary data for composing such a line, a data set, corresponding to different lifetimes at different pressures, must be measured. Such plots are often called Stern–Volmer dependencies.

In this work natural lifetimes and quenching rate constants for $N_2(C^3\Pi_u, v' = 0)$ and $N_2^+(B^2\Sigma_u^+, v' = 0)$ states are important. Typical Stern–Volmer dependencies for $N_2(C^3\Pi_u, v' = 0)$ state can be seen in figure 6.4.

The loss of nitrogen ion $N_2^+(B^2\Sigma_u^+, v' = 0)$ state, can be also due to ion conversion process, involving three particles (Badaloni and Gallimberti 1972):

$$N_2^+ + N_2 + N_2 \rightarrow N_4^+ + N_2 \,. \tag{2.32}$$

If k_3 is small or gas pressure, p, is very low the new term (2.30) approaches zero. Therefore, at lower pressures, one may expect the reciprocal of lifetime to be linearly related to pressure. At higher pressures N^2 increases more rapidly than N and three-body processes may become important. In that case the reciprocal of lifetime is linearly related to N^2. The exact transition pressure may be expected to depend on respective rate constants.

2.3.4. Surface processes

Surface processes are important, since production and loss of charged or excited particles can also happen due to processes related to surfaces. These surfaces may be discharge container walls or, more importantly, electrodes. Collisions between particles and surfaces can be described by particle flux onto a surface, which can be directly found from particle *flux density*, $\boldsymbol{\Gamma}$ ($m^{-2} \cdot s^{-1}$):

$$\boldsymbol{\Gamma} = \rho \cdot \boldsymbol{v} - D \cdot \nabla n \approx \rho \cdot \mu \cdot E, \tag{2.33}$$

where D ($m^2 \cdot s^{-1}$) is the diffusion constant. When an external electric field is absent or mobility is zero only the second part, related to diffusion, becomes important. When neutral particles collide with surfaces of the container they are bounced back without any effect, except for losing small amount of thermal energy the particle could have obtained in the discharge. Consequently, such collisions can be viewed as being responsible for energy outflow from the discharge. When an excited neutral particle collides with a surface the excited particle is effectively quenched. When an electron collides with a surface it is typically lost into the surface.

Most prominent surface effects are related to collisions between ions and surfaces. Since ions may be accelerated to high energies, collisions between ions and surfaces can have several important side effects, depending on impact or ionization energy and surface properties. First of these effects is called *secondary electron emission*, and it can be described by the following relation:

$$\boldsymbol{\Gamma}_{se} = \gamma_{se} \cdot \boldsymbol{\Gamma}_{p}. \tag{2.34}$$

Here $\boldsymbol{\Gamma}_p$ describes the flux of positive ions onto the surface, and $\boldsymbol{\Gamma}_{se}$ describes the flux of secondary electrons. Coefficient of proportionality, γ_{se}, describes the

number of secondary electrons produced per one incident ion. For metals γ_{se} is generally between 0.1–0.3. One may expect γ_{se} to be a function of kinetic energy of an incident ion. In practice, however, neutralization of 10 eV or 100 eV ions seems to release secondary electrons with almost equal effectiveness.

Experiment shows that γ_{se} is a function of the energy required to remove an electron from the surface, called *work function*, and also a function of the ionization energy of the incident ion. In a first approximation, the following relation can be used to estimate γ_{se} (Raizer 1991):

$$\gamma_{se} \approx 0.016 \cdot \Delta W. \tag{2.35}$$

Here ΔW, measured in eV, describes the difference between ionization energy and work function for two electrons – first electron neutralizes the ion. For metals the work function is generally several electronvolts. For aluminium cathode, used in this work, this energy is about 4.0–4.25 eV. For Al_2O_3 the energy is lower, about 3.8 eV. For N_2 ion, produced by process (2.12), and aluminium surface we obtain: $\Delta W \approx 15.6$ eV $- 2 \cdot 4.1$ eV ≈ 7.4 eV; $\gamma_{se} \approx 0.118$.

When ion impact energy is of the order of 100 eV or more ions can, in addition to secondary electron production, also sputter neutral atoms from the surface. Such process is known as *sputtering*. Sputtering is an important process by which thin films are deposited on substrates. In the present work sputtering is responsible for the wear-off of aluminium cathode, which may be quite disturbing factor for an experimenter. Results of such process can be seen in Appendix D. To reduce sputtering and preserve the cathode for longer, experimental points at lower E/N values were measured first.

Surface production of electrons can also be related to *photoelectric effect*. The incident photon energy must be equal or more than the work function of the metal surface. For aluminium surface the wavelength of the incident electromagnetic wave must be less than $1240/4.1 \approx 300$ nm. Since sputtering also effectively removes oxides from the surface, the number of electrons produced by photoelectric effect may vary, even if the UV source itself has a constant output power. Photoelectric effect can also be related to secondary electron production, if photons created in the discharge hit surrounding metal surfaces.

Electric fields around 10^7 V/m are strong enough to pull electrons directly out of solids (Dutton 1978). This effect is named *field emission*. This kind of effect is most easily achieved around sharp edges for which the electric field strength is strongly enhanced. Although field emission may be important source of electrons for some discharge types, in this work this type of electron emission must be avoided, since it can corrupt the measurement results for which E/N is presumed to be homogenous.

Other surface processes may also happen. These include fragmentation of the incident ion, absorption or desorption of gaseous particles, thermionic emission and implantation of ions into the solid.

2.3.5. Modelling of gas discharge processes

In this work, so far, two different descriptions of collisional processes are presented. The first, *microscopic model*, describes particular processes by corresponding cross-sections, σ. The second, *macroscopic model*, uses so-called *swarm parameters*, μ, α, η, to describe the production and loss of different particle species.

The relation between microscopic and macroscopic description for collisions with electrons, responsible for most of the reactions in the discharge, is determined by the EEDF and corresponding cross-sections. Formerly, EEDF and cross-sections of different processes were poorly known, and better results were often obtained by experimentally determining swarm parameters for subsequent usage rather than trying to calculate these directly from microscopic quantities. Since any gas discharge can be sustained in an infinite number of different gas mixtures, there isn't much experimental data available for different gas mixtures, except for simple cases, like air.

The arrival of computer era allowed calculating EEDF in the discharge by directly solving the Boltzmann equation. This equation, which we do not present here, describes the effect of applied electric field and collisions on the EEDF. Solving the Boltzmann equation is mathematically challenging and often numerical methods together with various approximations are implemented to find a solution (Raju 2006). However, the increase in accuracy of such calculations nowadays, allows calculating macroscopic swarm parameters directly from microscopic quantities. Often such calculations give better results than former results based on direct measurements. For example, $\alpha/N(E/N)$ can be found from relations (2.21) and (2.3), if all the microscopic processes and quantities required for this calculation are known.

In this work two-term numerical Boltzmann equation solver BOLSIG+ is used for calculating macroscopic swarm parameters from microscopic quantities for different nitrogen-oxygen mixtures and E/N ranges, for which the data available from literature is not sufficient or satisfactory. BOLSIG+ is a free computer program for the numerical solution of the Boltzmann equation for electrons in weakly ionized gases in uniform electric fields – conditions which occur in swarm experiments and in various types of gas discharges and low-temperature plasmas. Under these conditions the EEDF isn't exactly Maxwellian nor Druyvesteyn, and it is determined by an equilibrium between electric acceleration and momentum and energy losses in collisions with neutral gas particles. In Appendix A numerically calculated EEDFs from BOLSIG+ are presented for comparison with Maxwellian and Druyvesteyn.

From now on, we adhere entirely to macroscopic description of gas discharge processes, originally adopted by Townsend. Since macroscopic quantities can be expressed only as a function of E/N and N, formulae become more comprehensible, and we do not have to carry out a laborious computational task each time some experimental parameter changes – we can find the corresponding change by solely using the macroscopic model. Only when the gas mixture changes, must these macroscopic swarm parameters be recalculated from microscopic quantities.

2.4. Discharges between parallel-plate electrodes

Figure 2.1 shows typical set-up for sustaining and exploring gas discharges. It consists of a tube filled with gas that is being investigated. The external electric field is applied form a high-voltage (HV) source. Electric current, *i*, flowing through this gaseous medium can be measured by an ammeter (A). Generally, this tube is made of some transparent material to also explore the optical radiation emanating from the tube. This type of set-up has a very long history, dating back over a hundred years, and it is also used in this work.

Initial electrons released from the surface of the cathode diffuse both radially and longitudinally, although the radial diffusion presented in figure 2.1 is exaggerated. New electrons may be produced by ionizing collisions and, consequently, electron number density towards the anode increases. Near the cathode drifting electrons may have not yet collided statistically large number of times, so the EEDF near the cathode may not be fully developed.

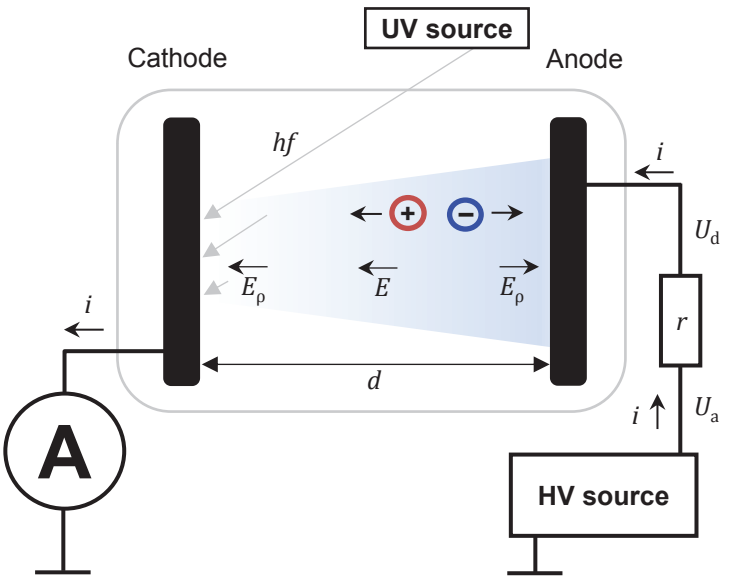

Figure 2.1. Set-up for sustaining and exploring gas discharges.

If the applied voltage is low and the UV source is switched off, a small current in the range of picoamperes is produced. This is due to normal background radiation and high-energy cosmic rays. Even the first natural philosophers experimenting with electric charge noticed that an isolated charged object loses its charge over the time. It took some time before a theory was hatched that this charge was flowing away through air (Anders 2003). The strength of such current does not depend much on the applied voltage, since the energy gained by electrons from the electric field remains much lower than is needed for ionization. In this case the applied voltage does not affect the number of charges

present in the discharge gap – the charge carrier number density is determined by background radiation or by the intensity of the UV source.

By increasing the applied voltage, at some point, a small proportion of electrons – high-energy tail tip of the EEDF – reach the ionization energy. From this point on the discharge current becomes dependent on the applied voltage, and several different forms of discharges may exist. If the intensity of the UV source is high enough, and the resistance of the external circuit, r, is high, then the discharge current cannot rise unlimitedly. Under these circumstances Townsend dark discharge develops, which is used in this work. If the voltage is kept low, typically, current in the range of nanoamperes is obtained. This current is determined by the number of initial electrons released from the cathode. These first electrons start to drift towards the anode. By increasing U_d, some new electrons are being produced by ionizing collisions, so the number of drifting electrons and positive ions increase – current strength remains in the range of microamperes for electrode diameters of the order of centimetres. Positive ions start to drift towards the cathode with much lower drift velocity than electrons drift towards the anode. Consequently, we have more positive ions in the discharge gap than electrons. The cumulative electric field produced by these ions is named *space charge field*, E_ρ. If these positive ions reach the cathode, secondary process (2.34) may happen. Since this process produces new electrons, which in turn produce new ions, a positive feedback develops. Without an external resistor, which produces negative feedback by decreasing U_d (minus sign in formula (2.36)), the discharge would rapidly transform to *glow discharge*. In glow discharge the current is much stronger, in the range of milliamperes, and processes are strongly affected by the space charge field. If the resistor has even lower resistance and the output power of the HV source is not limited, an *arc discharge* may develop, where processes are also strongly affected by the space charge field. The secondary production of electrons on the cathode can now be related to *thermionic emission* and the discharge current is of the order of amperes. Generally, in glow and arc discharges plasma state is achieved, in dark discharge plasma state is not achieved. If the resistance, r, is high and the intensity of the UV source is very low or zero, *spark discharge* may develop instead of dark discharge. In that case the capacitive energy related to the electrodes is discharged through the discharge gap. As the resistance of the outer circuit is high no constant discharge may develop, since it takes time for this 'capacitor' to be recharged again. The diameter of a spark discharge is small and the electric field is far from uniform. Lightning, for example, is a form of spark discharge. In the present work spark discharge, or *sparkling*, also occurred, especially around sharp or outstanding edges on the cathode. To avoid sparkling, the cathode was finely polished and sufficiently intense UV source was used, so that the necessary discharge current could be obtained at field strengths below the breakdown field. This discussion is true for parallel-plate discharge gaps; for other electrode geometries still different forms of discharges may exist, which we do not discuss here.

If the discharge is kept away from the edges of the electrodes and the distance between the electrodes, d, is much less than radius of the electrodes, then the macroscopic electric field in the discharge gap is homogenous and can be found from:

$$E = \frac{U_\mathrm{d}}{d} = \frac{U_\mathrm{a} - i \cdot r}{d} \,. \tag{2.36}$$

Formula (2.36) assumes that the discharge current kept is low, so that the influence of space charge field is negligible, which is generally true only for dark discharge. The upper limit of i for relation (2.36) to remain valid is evaluated in section 5.3. If the influence of space charge field is negligible, then E/N is not a function of coordinate, $x = 0 \ldots d$, α is constant, and equation (2.22) can be directly integrated:

$$\rho_\mathrm{e}(x) = \rho_\mathrm{e}(0) \cdot \exp(\alpha \cdot x) \,. \tag{2.37}$$

Consequently:

$$\ln(\rho_\mathrm{e}(x)) = \alpha \cdot x + \ln\left(\rho_\mathrm{e}(0)\right) \,. \tag{2.38}$$

The validity of relation (2.38) for the set-up used in this work was experimentally determined. Results can be seen in figures 6.1–6.3. Total number of electrons present in the discharge is related to electron number density by:

$$n_\mathrm{e}(t) = S_\mathrm{d} \cdot \int_0^d \rho_\mathrm{e}(x,t)\, dx \,. \tag{2.39}$$

The electrical current in the outer circuit produced by electrons in the discharge can be found from:

$$i_\mathrm{e}(t) = \frac{e \cdot n_\mathrm{e}(t) \cdot \mu_\mathrm{e} \cdot E}{d} \,. \tag{2.40}$$

Relations (2.39) and (2.40) can be composed for different charged species present in the discharge gap. The externally measured current, i, is the sum of currents produced by all the different charge carriers present in the discharge gap:

$$i(t) = i_\mathrm{e}(t) + i_\mathrm{p}(t) + i_\mathrm{ns}(t) + i_\mathrm{nu}(t) \,. \tag{2.41}$$

The obvious fact that a charged particle moving between the electrodes generates the same amount of electrical current in the outer circuit as if it were moving in the wires, is historically known as Shockley–Ramo theorem (Shockley 1938, Ramo 1939).

Let $\boldsymbol{\Gamma}_{e0}$ be the stationary flux density of initial electrons released from the cathode. The flux density of electrons reaching the anode will be $\boldsymbol{\Gamma}_e = \boldsymbol{\Gamma}_{e0} \cdot \exp(\alpha \cdot d)$. Since the production of every new electron is accompanied by the production of one positive ion, the flux density of positive ions that are neutralized on the cathode is $\boldsymbol{\Gamma}_e - \boldsymbol{\Gamma}_{e0}$. The flux density of positive ions is therefore $\boldsymbol{\Gamma}_p = \boldsymbol{\Gamma}_{e0} \cdot (\exp(\alpha \cdot d) - 1)$. The flux density of secondary electrons produced by process (2.34) is $\gamma_{se} \cdot \boldsymbol{\Gamma}_{e0} \cdot (\exp(\alpha \cdot d) - 1)$. Discharge in a parallel-plate discharge gap will become self-sustaining if the flux of secondary electrons becomes equal or larger than the flux of initial electrons, i.e. the initial electrons are no more needed, and all the electrons needed for sustaining the discharge are readily formed by the discharge itself. Consequently, we can write:

$$\gamma_{se} \cdot \boldsymbol{\Gamma}_{e0} \cdot (\exp(\alpha \cdot d) - 1) = \boldsymbol{\Gamma}_{e0} \,. \tag{2.42}$$

By inserting the two-term approximation for $\alpha/N(E/N)$ from relation (2.23) into (2.42) we obtain:

$$A \cdot N \cdot d \cdot \exp\left(-\frac{B \cdot N}{E}\right) = \ln(1 + \gamma_{se}^{-1}) \,. \tag{2.43}$$

For a parallel-plate gap the macroscopic electric field can be found from (2.36). Solving for U_d, we find that:

$$U_{br}(Nd) = \frac{B \cdot Nd}{\ln(A \cdot Nd) - \ln(\ln(1 + \gamma_{se}^{-1}))} \,. \tag{2.44}$$

This relation, where U_{br} is often called *breakdown voltage*, is historically known as Paschen's law, dating back to 1889 (Paschen 1889). Dark discharge is sustained only if the discharge is not self-sustaining, i.e. is *non-self-sustaining*, so condition (2.44) must never be met in this work, and the applied voltage must be less than the breakdown voltage – otherwise spark discharge would occur.

Dark discharge can be sustained at different E/N values at the same pressure if the discharge chamber enables to change the distance between the electrodes, d. All experimental points should lie below the curve predicted by (2.44). The minimum voltage corresponding to function (2.44) is given by:

$$U_{min} = 2.718 \cdot \frac{B}{A} \cdot \ln(1 + \gamma_{se}^{-1}) \,. \tag{2.45}$$

Relations (2.44) and (2.45) are plotted in figure 4.3 with coefficients A and B for air taken from table 2.1. Secondary electron emission coefficient, $\gamma_{se} \approx 0.118$, is obtained from formula (2.35) for ions created by process (2.12) that are neutralized on a clean aluminium surface. One can see that the somewhat

simplified treatment of the processes involved produces a curve that is similar in form to real Paschen's curve, but still substantially diverges from it. The main reasons for the visible discrepancy are the simplified form of α/N, and that only one secondary processes was included for obtaining relations (2.44) and (2.45).

In addition to processes described in this chapter, free electrons accelerated by externally applied electric fields can also excite molecules via inelastic collisions. This is important, especially in the context of this work, since it allows retrieving information from the discharge by using non-contact spectroscopic methods. This topic is shortly discussed in the next chapter.

3. SPECTRUM OF DIATOMIC MOLECULES

3.1. Introduction

So far we have, for several times, referred to the excited states and corresponding optical emission investigated in this thesis. The theoretical basis for determining natural lifetimes and quenching rate constants of the nitrogen $N_2(C^3\Pi_u, v' = 0)$ and $N_2^+(B^2\Sigma_u^+, v' = 0)$ excited states was discussed in the previous chapter. Also, the major excitation and loss mechanisms for the states under investigation in cold non-LTE discharges were described. The notations for these excited states may have seemed quite intimidating at first, but in this chapter all these obscurities are clarified.

For gas discharges sustained in molecular gases the accompanying spectra are far more complicated than for discharges sustained in noble gases, since the number of possible processes is larger. However, by understanding the basics of molecular spectra, useful information about the discharge can be derived from analysis of the resulting spectra. The physics and spectroscopy of molecules is a vast area, and here only a short overview of the most important aspects related to the results of this work is given.

3.2. Energy levels and allowed transitions

For an atom the energy levels are basically related to the distance of electrons form the heavy positive nucleus, since any atom is symmetric about its centre of mass. The energy levels for molecules are more complicated for several reasons. Firstly, molecules have additional vibrational and rotational degrees of freedom due to the motions of their nuclei. Secondly, the energy of each electronic state, W_e, depends on the instantaneous configuration of the nuclei. Such dependence is often represented on a graph of W_e versus internuclear separation. For a stable molecule there must be a minimum energy, corresponding to its minimum energy or ground state, so that extra energy must be supplied to separate the atoms. An excited electronic state can either have a potential minimum or not. If no minimum exists, then excitation can result in a breakup or dissociation of that molecule. Typically, internuclear separations, corresponding to potential energy minimums for different electronic states, do not coincide. Excited electronic states can be short-lived and lose their energy quickly through electric dipole radiation or be metastable. Typical spacing between low-lying electronic states is about 1–20 eV, corresponding to 60–1200 nm, i.e. UV and visible region (Lieberman and Lichtenberg 1994).

In addition to electronic energy, W_e, levels, diatomic molecules possess additional vibrational energy, W_v, and rotational energy, W_J, levels. Vibrational motion can be classically bound to the Coulomb-like interaction between the two nuclei. Typical spacing between vibrational states of low-lying electronic states is ~ 0.2 eV, corresponding to ~ 6000 nm, i.e. infrared region. For

molecules at or near room temperature, with thermal energy $W \sim 0.026$ eV, only $v = 0$ level is significantly populated. However, collisional processes, described previously, can excite those non-equilibrium vibrational energy levels (Lieberman and Lichtenberg 1994).

Typical spacing between rotational energy levels, W_J, is between 0.001–0.01 eV, corresponding to about 120–1200 μm, i.e. microwave region. Therefore, many low-lying rotational energy levels are populated in thermal equilibrium at room temperature. Rotational motion can be classically viewed as the rotation of molecule around its centre of mass.

When a molecule goes from a higher energy state, W', often denoted by a single prime, to a lower energy state, W'', often denoted by a double prime, it can emit a photon with frequency, f:

$$W' - W'' = hf = \Delta W_e + \Delta W_v + \Delta W_J \,. \tag{3.1}$$

This change in energy is the sum of corresponding changes in electronic, vibrational and rotational energies. Calculating emission frequencies or wavelengths from (3.1) for a particular diatomic molecule is, however, rather difficult. Typical spacing between different electronic, vibrational and rotational states is not a constant, and these energies are not totally independent of each other. Besides, not all of the possible transitions are allowed, and those that are allowed, have all different probabilities, which gives evidence as a difference in emission intensities. From this simple analysis one can still conclude that pure rotational spectra should lie in the far infrared or microwave region and pure vibrational spectra in the infrared region. Emission in the visible region must be accompanied by a change in the electronic energy, W_e, state while, at the same time, a change in vibrational, W_v, or rotational energy, W_J, may also occur.

The opposite is also true, as can be seen from figure 3.1, where energies for collisional excitation in N_2 are shown. One can see that to excite an electronic state at least about 1 eV is needed in the case of N_2. From Appendix A we can conclude, that at given E/N values all these processes are possible for collisions with electrons, since EEDFs easily reach 10 eV.

Subsequent decay of these excitations gives rise to rotational, vibrational and electronic spectroscopy. For homonuclear diatomic molecules, such as N_2 and O_2, quantum mechanics prohibits pure vibrational or rotational transitions and, therefore, these molecules do not have a pure vibrational or rotational spectrum, though there is emission and absorption from these molecules at visible frequencies, i.e. radiative transitions between electronic levels. With accompanying electronic transition, changes in rotational and vibrational energies are allowed. This means that transitions between electronic states have many different vibrational and rotational initial and final states, which give rise to a structure of emission and absorption bands, within which, a set of closely spaced frequencies appear, with ~ 0.01–0.1 nm. Thus, typically, electronic transition appears as a band (Lieberman and Lichtenberg 1994).

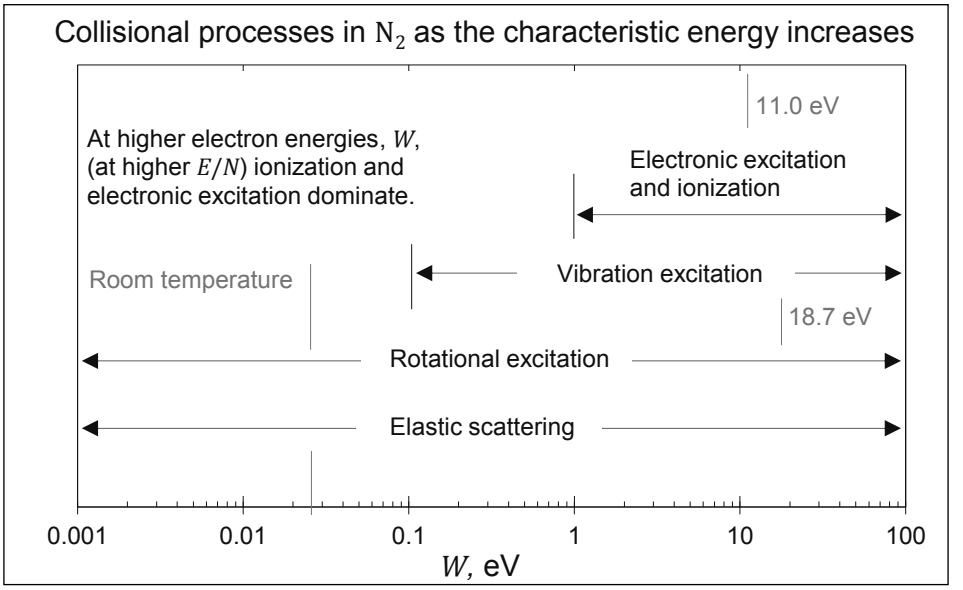

Figure 3.1. Collisional processes in N_2 (Raju 2006).

To determine corresponding emission frequencies of a diatomic molecule one usually starts with a 'decent' function that describes the potential energy between the two atoms. Selecting the best function for potential energy is of utmost importance, since there is one-to-one correspondence – relation (3.1) – between the emission frequencies and changes in potential energy.

Let us consider the potential energy curve of a molecule. Any acceptable form for a potential energy function should have a large value, if not infinite, as the nuclei come together; it should pass through a minimum at the equilibrium separation, r_e; and it should approach dissociation energy as the nuclei become far apart. There are an infinite number of functions, which have a shape suitable for potential functions. Of these, the Morse function is the simplest and most generally useful, but only, when the vibrational excitation is not too large, i.e. when the motion is confined to the bottom of potential energy curve. Other functions for potential energy that are historically used include the three-parameter Manning and Rosen function, Poschl–Teller function, potential curve of Hylleraas, Hulburt and Hirschfelder potential and others (Hugh *et al* 1941).

While historically many different functions are used, the Dunham form is most widely accepted:

$$W(r) = a_0 \cdot \xi^2 \cdot (1 + a_1 \cdot \xi + a_2 \cdot \xi^2 + \cdots) \cdot hc\,, \tag{3.2}$$

$$\xi(r) = (r - r_e)/r_e\,. \tag{3.3}$$

Here r is the internuclear separation, and r_e is the internuclear separation

corresponding to minimal potential energy, i.e. equilibrium value; a_0, a_1, a_2 are suitable constants. For N_2 ground state $r_e = 0.1095$ nm (Hugh *et al* 1941).

To transform this potential energy function to spectrum, typically, a separable Schrödinger equation in Born–Oppenheimer approximation (Born and Oppenheimer 1927) is solved to find corresponding, now quantized, energy levels. This means that the electronic and nuclear motions are treated independently. Solutions, neglecting fine structure, are usually expressed as follows:

$$W' - W'' = hc \cdot [G(\nu)' - G(\nu)'' + F(\nu, J)' - F(\nu, J)''] \,. \tag{3.4}$$

Relation (3.4) is similar to relation (3.1), but here $G(\nu)$ and $F(\nu, J)$ are so-called *term energies*, in units of cm^{-1}, corresponding to vibrational and rotational motion. In this notation electronic term, corresponding to ΔW_e, is already included in $\Delta G(\nu)$. Further, $G(\nu)$ can be expressed as:

$$G(\nu) = \sum_{i=0}^{m} Y_{i,0} \cdot \left(\nu + \frac{1}{2}\right)^i \,, \tag{3.5}$$

where ν is vibrational quantum number and $Y_{i,j}$ are Klein–Dunham coefficients. If we summed from i = 1 instead, we would obtain only vibrational term energy, since electronic term energy corresponds to Klein–Dunham coefficient $Y_{0,0}$. Rotational term energy, neglecting fine structure, can be expressed as:

$$F(\nu, J) \approx B(\nu) \cdot J(J+1) - D(\nu) \cdot J^2(J+1)^2 + \cdots \,. \tag{3.6}$$

Here J is rotational quantum number and $B(\nu)$ and $D(\nu)$ are related to Klein–Dunham coefficients by the following formulae:

$$B(\nu) = \sum_{i=0}^{m} Y_{i,1} \cdot \left(\nu + \frac{1}{2}\right)^i ; \;\; D(\nu) = \sum_{i=0}^{m} Y_{i,2} \cdot \left(\nu + \frac{1}{2}\right)^i \,. \tag{3.7}$$

Since for electronic transitions ΔW_e typically accounts for the bulk of energy related to a particular transition, most basic information about that transition can be retrieved by finding ΔW_e from respective Klein–Dunham coefficients.

To find corresponding band intensities, we must first recall that not all transitions are allowed. Allowed transitions cannot be explained away by classical physics, and from hereon we must adhere ourselves to quantum mechanical description. Subsequent analysis is only true for electronic transitions of homonuclear diatomic molecules.

Different electronic states are described first by the component of the total orbital angular momentum along the internuclear axis, Λ (in units of h), with the symbols Σ, Π, Δ and Φ, corresponding to Λ = 0, ±1, ±2, ±3. For Σ states +/– superscripts are added to denote whether the wave function is symmetric or

antisymmetric with respect to reflection at any plane through the internuclear axis. The total electron spin angular momentum, S, is also specified, with the multiplicity of 2S + 1, and is written as a prefixed superscript. The number of total angular momentum, Ω, can be, in essence, obtained as the sum of orbital angular momentum component, Λ, and spin angular momentum, S. Subscripts g or u denote whether the wave function is symmetric or antisymmetric with respect to interchange of the nuclei. In this notation, the lowest energy state, ground state, of N_2 becomes $X^1\Sigma_g^+$ (Lieberman and Lichtenberg 1994).

The selection rules for the strongest mechanism of photon emission are: $\Delta\Lambda = 0, \pm 1$ and $\Delta S = 0$. For homonuclear molecules, the only allowed transitions are g → u and u → g. This, as mentioned before, means that homonuclear diatomic molecules do not have a pure vibrational or rotational spectrum. Within an electronic transition there is no special selection rule for Δv. For ΔJ the selection rules are: $\Delta J = -1$ (P-branch of the transition band), $\Delta J = +1$ (R-branch of the transition band), and $\Delta J = 0$ (Q-branch of the transition band).

Finally, how the transition energy, $W' - W''$, is distributed between different vibrational and rotational lines within an electronic transition. There are also selection rules that control which electronic states provide strongest transition probabilities, but this topic is omitted here, since it has less importance in regard to present work. As there is no special selection rule for Δv, values of Δv up to 5 or 6 are not uncommon. High energy transitions in atoms or molecules tend to be very fast, compared to nuclei, which move much slower than the electrons. This means that electronic transitions for which the change in distance between the nuclei is smaller have higher probability. In a potential energy diagram this idea manifests itself as a vertical line between the two electronic states, and it is historically known as the Franck–Condon principle (Condon 1926). To mathematically calculate probabilities one needs corresponding Franck–Condon factors.

Each vibrational transition, Δv, is further superimposed by rotational lines, forming a band structure. To find corresponding rotational line intensities we must take into account how the rotational energy levels of the upper vibrational state are populated, since under normal conditions many rotational levels are populated, with $\Delta W_J = 0.001$–0.01 eV. Under thermodynamic equilibrium the relative population of excited states, Q_J, at a given temperature, T, is determined by the Boltzmann distribution:

$$Q_J(v, J)' \sim S_J(J') \cdot \exp\left(-\frac{hc \cdot F(v, J)'}{k_B \cdot T}\right). \tag{3.8}$$

Here $S_J(J)$ can be, in most simple cases, expressed by $S_J(J) = 2J + 1$. For electronic transitions this quantity also depends on how the orbital angular momentum of the electrons, the spin angular momentum of the electrons, the nuclear rotational angular momentum, and the nuclear spin all combine, or more specifically *couple*, i.e. on Ω. This topic is, however, too complicated for a

general description here, and it is shortly discussed in section 5.4 for particular transitions investigated in this thesis.

Lastly, and most importantly, since $S_J(J)$ and $F(v,J)$ are both functions of J, the relative population of excited states, Q_J, does not decrease immediately with the rotational quantum number, J, but first goes through a maximum. This can be seen in figures 5.2 to 5.4 where calculated rotational band structures for the transitions investigated in this thesis are presented.

3.3. Spectrum of molecular nitrogen

Nitrogen molecule has been one of the most thoroughly investigated, since most of Earth's atmosphere consists of N_2. Surely, everyone has encountered a visible blue spark or flash, either caused by static electricity in a dark room or, most conspicuously, a bolt of lightning. The glaring blue colouring of such events is in fact caused by intense electronic emission bands of N_2 molecule and molecular ion, N_2^+. Nitrogen also plays a significant role in other atmospheric phenomena, such as aurorae and airglows.

Nitrogen atom has the following electronic structure: $(1s^2)$ $(2s^2\ 3p^3)$. The first two inner shell electrons virtually retain their atomic character and are often called *K* or inner shell orbitals. Next two electrons of n = 2 levels form two orbitals with different energy, which both take 1 electron from either atom. These are $(2s\sigma_g)^2$ $(2s\sigma_u)^2$ states. For σ states $m_l = 0$. The symmetric state, σ_g, with respect to inversion through the centre of symmetry, has the lowest energy. The last three electrons from each atom are divided between the $(2p\pi_u)^4$ ($m_l = \pm 1$) and $(2p\sigma)^2$ states. For 6 out of 10 electrons the potential energy decreases ($(2s\sigma_g)^2$ and $(2p\pi_u)^4$ states) during molecule formation, producing a stable molecule. For N_2 ground state the overall angular momentum on the inter-nuclear axis is Λ = 0, therefore a Σ term. Also S = 0, since all electrons are paired, and, consequently, the ground state can be expressed as $X^1\Sigma_g^+$. Capital X is added to explicitly state that it is a ground state. Other letters – A, B, C, etc. – are used for excited states of the same multiplicity (2S+1) and are applied in order of increasing energy. States with multiplicity different from the ground state are noted with lowercase letters a, b, c, etc. The ground state of N_2^+ is denoted similarly, but as one electron is removed, the ground state of N_2^+ can be expressed as $X^2\Sigma_g^+$.

Molecular nitrogen possesses one of the richest spectrum of any diatomic molecule. The study of the spectrum of molecular nitrogen can be traced back to 1858–1859 when the first attempts were made to describe parts of this spectrum by investigating discharges in gases. Nitrogen spectrum was also used in early development of quantum theory of molecular spectra. Numerous band systems, corresponding to electronic transitions of N_2 and N_2^+, span from 49 nm to 8500 nm. The whole visible region is dominated by very strong $B^3\Pi_g \rightarrow A^3\Sigma_u^+$ First Positive and $C^3\Pi_u \rightarrow B^3\Pi_g$ Second Positive systems (SPS) of N_2, and only

under rather special conditions can these systems be sufficiently suppressed to permit observation of weaker systems. Other intensive systems in the visible region include $B^2\Sigma_u^+ \rightarrow X^2\Sigma_g^+$ First Negative system (FNS) of ionized nitrogen, N_2^+. System, in the context of previous section, refers to the fact that each electronic transition is further superimposed by vibrational structure. All these different transitions are collectively referred to as a band system (Lofthus and Krupenie 1977).

Nitrogen is widely used in plasma and gas discharge physics. Since it is readily available and its spectral characteristics are well known, it is also often used as an admixture in gas discharges, serving as a trace gas. This enables to retrieve information from the discharge via non-contact spectroscopic methods based on the interpretation of the emission spectrum.

3.4. Objectives of this thesis

To this day, optical emission spectrum of molecular nitrogen is the main tool for investigation of electric discharge phenomena in ambient atmosphere and it is often used for diagnostics of low-temperature gas discharge plasmas. Current thesis combines two disciplines – gas discharge physics and spectroscopy. The study is focused on a development of a spectroscopic method for determination of electric field strength in low-temperature gas discharge plasmas in atmospheric air. Measuring electric field strength by using probes or other contact methods is possible only in limited cases. A spectroscopic method, based on the measurement of the ratio of emission intensities of nitrogen spectral bands, can be used for this purpose if the excitation of nitrogen molecules from the ground state by electron impact is the dominant process. Usually the intensities of the most intensive spectral bands of the SPS of N_2 and FNS of N_2^+ are compared (Gallimberti *et al* 1974, Hartmann 1977, Creyghton 1994, Djakov *et al* 1998, Kozlov *et al* 2001). These bands correspond to the following transitions:

$$N_2\ C^3\Pi_u \rightarrow B^3\Pi_g \text{ (0–0, SPS) at } \lambda \approx 337.1 \text{ nm (3.68 eV)}, \tag{3.9}$$

$$N_2^+ B^2\Sigma_u^+ \rightarrow X^2\Sigma_g^+ \text{ (0–0, FNS) at } \lambda \approx 391.4 \text{ nm (3.17 eV)}. \tag{3.10}$$

Here (0–0) indicates the two vibrational quantum numbers involved in these electronic transitions, where the upper value, v', is given first. For a number of different discharge forms the upper levels of these transitions are mainly populated by direct electron impact from the ground state of N_2:

$$X^1\Sigma_g^+ + e\ (W \geq 11.0 \text{ eV}) \rightarrow C^3\Pi_u + e, \tag{3.11}$$

$$X^1\Sigma_g^+ + e\ (W \geq 18.7 \text{ eV}) \rightarrow B^2\Sigma_u^+ + 2e. \tag{3.12}$$

Still, other excitation mechanisms, like cascading from higher vibrational levels, cannot be excluded. Process (3.12) produces an excited ionized molecule, N_2^+, that may subsequently decay through process (3.10). In Appendix B these processes are presented on a simplified potential energy diagram of N_2 and N_2^+. The excitation threshold energies of these bands differ considerably (11.0 eV and 18.7 eV) and, therefore, the ratio of emission intensities is sensitive to changes in the mean electron energy, W_{mean}. Mean electron energy is, in turn, a function of electric field strength.

The expected ratio of emission intensities, $R_{\lambda 1/\lambda 2}$, can be directly calculated from:

$$R_{\lambda 1/\lambda 2}(E/N, N) = \frac{I_{\lambda 1}(E/N, N)}{I_{\lambda 2}(E/N, N)} = \frac{k_{\lambda 1}(E/N) \cdot g_{\lambda 1}(N)}{k_{\lambda 2}(E/N) \cdot g_{\lambda 2}(N)} . \qquad (3.13)$$

Here $I_{\lambda 1}$ and $I_{\lambda 2}$ are emission intensities – photon fluxes – corresponding to these bands. In this work we refer to a particular transition by a subscript, denoting its approximate transition wavelength, since the wavelengths are easiest to remember. In relation (3.13), $k_{\lambda 1}(E/N)$ and $k_{\lambda 2}(E/N)$ are second-order rate constants calculated from relation (2.21) using corresponding emission cross-sections $\sigma_{\lambda 1}(W)$, $\sigma_{\lambda 2}(W)$ and EEDF, $f(E/N, W)$. In Appendix A emission cross-sections for processes (3.9) and (3.10) are presented. From these figures we can deduce that at 165 Td there should be emission present from SPS 0–0 transition, since the EEDF easily reaches 11.0 eV, and the rate constant is non-zero. For FNS 0–0 transition the rate constant should be close to zero, since the EEDF barely reaches 18.7 eV. Therefore, $R_{391/337}(165\ \mathrm{Td}, N) \approx 0$. If incident electron energy rises from 20 eV to 30 eV, the emission intensity from SPS 0–0 transition should decrease, while, at the time, the emission intensity from FNS 0–0 transition should increase. Omitting collisional quenching, at about 23 eV, these emission intensities should be just about equal.

In relation (3.13), $g_{\lambda 1}(N)$ and $g_{\lambda 2}(N)$ denote the proportion of excited molecules that actually radiate, since at the same pressure the quenching rates for the upper states of these transitions may be different. Using the model presented in section 2.3.1 for binary collisions, we can conclude that the proportion of excited molecules that can radiate before they are collisionally quenched is τ/τ_0. Rearranging terms in relation (2.20), we obtain:

$$g(N) = \frac{\tau}{\tau_0} = \frac{1}{1 + \tau_0 \cdot k_{\mathrm{q}} \cdot N} . \qquad (3.14)$$

Here k_{q} denotes the second-order rate constant related to quenching of particular excited state. Note that if $\tau_0 \cdot k_{\mathrm{q}} \cdot N << 1$ this term is equal to 1, i.e. all excited states can radiate. If k_{q} or N increase, the emission intensity from corresponding transition decreases. To evaluate relation (3.13), EEDF, together with emission cross-sections, quenching rate constants, and natural lifetimes for both transitions must be known.

Historically, all these quantities were poorly known and values, much different from each other, were available from literature. Therefore, calculating the ratio of emission intensities from relation (3.13) presented a challenge. Nevertheless, this has been previously done by several authors (Creyghton 1994, Djakov *et al* 1998, Kim Y *et al* 2003). Current investigation was inspired by the fact that the results of different authors diverge considerably and to our knowledge no previous experimental investigation had been made. Under atmospheric-pressure conditions it is difficult to get spatially uniform low-temperature gas discharge plasmas with known field strength for a wide range of electric field strengths. Further, the presence of space charges complicates the calculation of any parameter in the discharge. At the same time, for lower discharge currents, where the influence of space charge is negligible, the emission intensities of resulting optical signals have extremely low values. These are probably the main reasons why measurements were missing up to now (Paris *et al* 2004).

As a result, the dependence of the intensity ratio of the above-mentioned nitrogen bands on the field strength in air was determined experimentally in a wide range of E/N values for the first time (Paris et al 2004, 2005, 2006; I–III). To correctly estimate relation (3.14) under our experimental conditions, quenching rate constants for $N_2(C^3\Pi_u, \nu' = 0)$ and $N_2^+(B^2\Sigma_u^+, \nu' = 0)$ states – upper states of the examined transitions – by N_2 and O_2 molecules were also determined (Valk *et al* 2010; IV). The original idea that non-self-sustaining discharge could be used for experimentally determining $R_{391/337}(E/N,\ N)$ was pointed out in Kozlov *et al* 2001.

Since there is partial overlapping between the FNS 0–0 and SPS 2–5 bands, emission from

$$N_2\ C^3\Pi_u \rightarrow B^3\Pi_g\ (2\text{–}5,\ \text{SPS})\ \text{at}\ \lambda \approx 394.3\ \text{nm}\ (3.14\ \text{eV}) \qquad (3.15)$$

transition was also registered, and ratios $R_{391/394}(E/N,\ N)$, $R_{394/397}(E/N, N)$ were determined in addition to $R_{391/337}(E/N, N)$.

4. EXPERIMENTAL SET-UP

4.1. Introduction

Sketch of experimental set-up is presented in figure 4.1. The exact configuration of the set-up, which constantly improved over the years, was varied slightly from experiment to experiment according to the goals of that particular experiment, and can be obtained from corresponding publications. Here only most general and important features of the set-up are discussed in detail.

Non-self-sustaining discharge, also known as Townsend or dark discharge, was excited between parallel-plate electrodes, as described in section 2.4. Experimental set-up is very similar to that of depicted in figure 2.1. The main difference is that negative voltage relative to ground was applied to cathode as opposed to positive voltage being applied to anode. In addition, the cathode was illuminated from the other side. The advantage of this set-up is that the cathode can be illuminated uniformly. The disadvantage of the set-up used in this work is that the thickness of the cathode has to be exact – too thick and there would be no electrons released from the other side, too thin and the electrical conductivity of the aluminium coating would be too poor.

Anode was made of brass and polished with an abrasive (grain size 0.2 μm) to mirror quality. The diameter of the flat area of the anode was 22 mm, and the curvature radius of edges was 4 mm. A thin aluminium coating evaporated on a quartz plate served as a cathode (see Appendices C and D). The diameter of the illuminated central semi-transparent area of the cathode was 18 mm. Electrodes were installed in a vacuum chamber with a volume of about 80 cm^3. The chamber was equipped with quartz windows. The discharge chamber is designed to be operated in non-self-sustaining discharge mode, which is excited by illuminating the cathode by UV radiation, whether in pulsed mode using excimer laser with wavelength 248 nm, or continuous mode using low pressure mercury lamp and interference filter for 253 nm.

Most of the equipment was computer-controllable, allowing continuous monitoring and recording of all the experimental parameters. It also enabled to carry out experiments with predetermined timing, controlled by corresponding software routines. This helped to distinguish between effects intrinsic to processes under interest and effects related to experimental procedures. However, lenses, mirrors, valves, and the distance, d, adjustment knob had to be still operated manually.

If the current density is chosen low enough, ensuring that the influence of space charge field, E_ρ, is negligible then the macroscopic electric field in the discharge gap can be calculated from formula (2.36) as the ratio of the applied voltage, U_d, and the distance between the electrodes, d. As the breakdown field strength increases when there is a decrease in the distance between electrodes, different electric field strengths can be applied by changing d. In this way processes under interest can be examined at predetermined reduced electric field strengths. The discharge chamber enabled to sustain dark discharge in the range from 100 Td to 4000 Td.

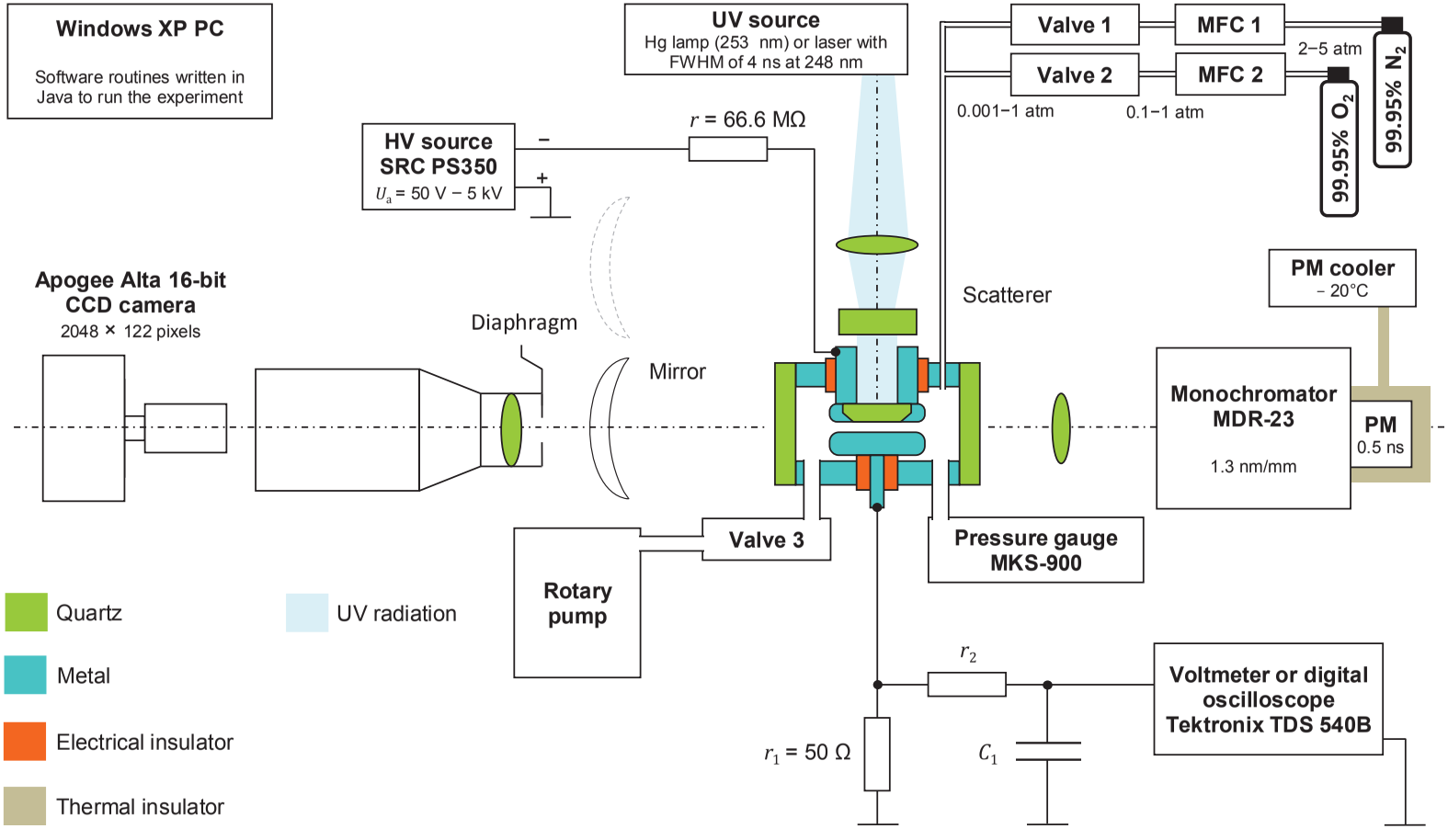

Figure 4.1. Sketch of the experimental set-up.

The severe problem with non-self-sustaining discharge is that optical and electrical signals are of very low intensity, as the charged and excited particle number densities are very low.

4.2. Experimental equipment

The cathode was stressed via current-limiting and stabilizing resistor of $r = 66.6$ MΩ (Philips components VR37 33 M ±1%, two in series). The resistance, r, of the resistor was verified to be independent of the applied voltage or current.

High voltage, below the breakdown voltage, U_{br}, was applied to the cathode using Stanford System's SRC PS350 high-voltage (HV) source. Accuracy of the HV source was 2.5 V + 0.1% of output voltage, U_{a}, and resolution was 1 V. Output ripple was less than 0.002% of full scale (5 kV). The output voltage was adjustable form 50 V to 5000 V. Output voltage was verified once a year by a high-accuracy voltmeter, the difference was always less than the provided margin of error. Stanford System's SRC PS350 was completely computer controllable. For voltages over 5 kV, Matsusada AW-60 HV source was used instead.

For continuous discharge current mode the voltage, U_{d}, between the electrodes was calculated as indicated by formula (2.36), where U_{a} is the voltage applied from the HV source, and i is the discharge current. For pulsed discharge mode the situation gets more complicated. In our case the capacitance between the electrodes, C, was no less than $C_0 = 36$ pF, and the charge carried by a discharge during one laser pulse was less than 1 nC, typically 0.01–0.1 nC. Corresponding time constant, τ, is therefore $r \cdot C_0 = 2.4$ ms. During one discharge pulse, U_{d} decreases up to 1 nC/$C_0 \approx 28$ V. After this discharge pulse U_{d} rises up to U_{a} again. The voltage between the electrodes, U_{d}, can be read equal to U_{a} provided that the pulse repetition rate is low. In our case it was up to 20 Hz, and we obtain 1/20 Hz = 50 ms. This is about 20 times more than the time constant and, consequently, there is plenty of time for U_{a} and U_{d} to become equal. For smaller inter-electrode distances and lower U_{a} the capacitance increases, and it is safe to assume that under pulsed discharge mode the gap voltage, U_{d}, always differed less than 1% from the applied voltage, U_{a}.

Distance between the electrodes, d, was settable between 0–6.0 mm, but typically remained in the range of 0.15–5.6 mm. The distance between the electrodes was measured by a dial gauge and was adjustable with an accuracy of 0.01 mm. The accuracy of d was determined to be less than 0.01 mm + 1% of d. This distance depended slightly on gas pressure, p, inside the chamber. If gas pressure inside the chamber is less than the atmospheric pressure outside, the distance decreases linearly with pressure:

$$d(p) = d_0 - (1\ \mathrm{atm} - p) \cdot 0.03\ \mathrm{mm/atm}\,. \tag{4.1}$$

Here d_0 is the distance between the electrodes at atmospheric pressure. Relation

(4.1) was determined by measuring the capacitance between the electrodes at different pressures. Small inter-electrode distances, $d < 0.3$ mm, were rarely used because relative uncertainty of E/N steeply increases with decrease in d. Therefore, small d implies 'high probability of breakdown'. Normally, experiments were at first carried out with d between 0.5–5.6 mm. Only after that tried we measure some experimental points with $d < 0.5$ mm. Frequently, this attempt would end up with the destruction of the cathode. This topic is discussed further in sections 4.4 and 4.6.

Electric field strength between the electrodes can be calculated from formula (2.36). To obtain E/N from relation (2.2), we also need to know gas pressure, p, and temperature, T. Gas pressure in the chamber was controlled by a valve which controlled the rate at which gas was pumped away from the chamber (valve 3), or by adjusting gas flow rate into the chamber. Typically, rough adjustments to the pressure were made by adjusting valve 3, and more accurate adjustments were made by adjusting the gas flow rate into the chamber, which could be controlled more precisely. Gas pressure was measured with the help of a MKS-900 transducer, combining piezoelectric and micro Pirani transducers. The accuracy of the transducer was 1% at pressures above 10 Torr (piezoelectric) and 10% at pressures below 10 Torr (micro Pirani). Typical pressures for which measurements were carried out remained in the range of 1–760 Torr.

Gas, N_2 or mixture of N_2 and O_2, supplied by AGA with purity of 99.95%, was directed into the chamber via mass flow controllers (MFCs), supplied by Alicat Scientific. With the use of valves 1, 2 and MFCs, gas was allowed to continuously flow through the discharge chamber during all the measurements. Continuous gas flow removes reaction products that can accumulate in the case of a stagnant medium. Constant flow also removes probable long-lived excited molecules whose quenching ability may be different from that of molecules in the ground state. Careful adjustment of valve 3 and gas flow rate into the chamber allowed the pressure to remain very stable over many hours of continuous operation. Gas flow speed, together with gas pressure and temperature in the chamber, were continuously monitored and recorded.

The full scale of the MFC used for N_2 flow was 1 litre/min; for O_2 controller the full scale was 0.1 litre/min, respectively. Both controllers had additional dust filters installed with bore size of 15 μm. Accuracy of each controller was ± 0.4% of the flow rate ± 0.2% of full scale. As the accuracy of the flow rate depends on flow rate itself, the flow rate was chosen such that for gas mixtures the error of oxygen concentration in N_2 was always less than 1%. For synthetic air, the concentration of O_2 was between 19–21%. Valves 1 and 2 were used to keep the pressure inside the controllers higher than pressure inside the chamber. This was necessary because the MFCs did not operate well at low pressures due to the accuracy of piezoelectric transducers inside the controllers. As the MFCs were operated in continuous mass flow mode, valves 1 and 2 did not change pressure inside the discharge chamber nor the gas mixture, but only the pressure inside each of the controllers. The controllers could also be operated in continuous volume flow mode, but this option was rarely used, because gas

mixing would be more complicated. Flow controllers measured volume flow, the conversion to mass flow (at STP) was done electronically. For that purpose each MFC also incorporated sensors for measuring gas pressure and temperature inside the MFC. Typical volume flow rates in the discharge chamber were in the range of 1–10 litre/min, depending on gas pressure inside the chamber. Typically, gas pressure inside tubes from cylinders to MFCs was about 2–5 atm; pressure inside the MFCs remained in the range of 0.1–1 atm; pressure inside the discharge chamber remained in the range of 0.001–1 atm. The pressure reading of the MKS-900 transducer could be easily compared to readings of piezoelectric pressure transducers inside each of the MFCs. At zero flow rate and at atmospheric pressure the difference was less than 0.5%.

Anode was grounded via resistor $r_1 = 50\ \Omega$. The discharge current, i, which remained between 0.5–2 μA in continuous mode, was found from the voltage on r_1. Resolution of i was 0.1 nA. Accuracy of i was estimated to be better than 1% in all our experiments in continuous mode. During breakdown, gas conductivity is high and the voltage on r_1 can rise up to $U_a/2$, as the charge is divided evenly between the electrodes. This may be several kilovolts. To protect the input of a voltmeter from such high voltages, an RC-circuit with time constant of $r_2 \cdot C_1$ was used, with $r_1 \cdot C_0 << r_2 \cdot C_1$. In the case of breakdown, charge quickly flows to the ground through r_1, and the voltage on C_1 cannot rise significantly. This breakdown, or sparkling, cannot happen continuously, as it takes time to recharge C_0 again. For experiments carried out in pulsed mode, an attenuator was used to protect the delicate input of the oscilloscope, because an RC-circuit would distort registered waveforms.

Gas temperature, T, was measured by temperature sensors inside the MFCs. This temperature was verified to be equal to room temperature. Resolution of T was 0.1 K, and accuracy was 0.5%. Gas temperature inside the discharge is addressed in section 5.2.

Initial electrons were released by UV radiation, whether in pulsed mode using KrF excimer laser with wavelength 248 nm, or continuous mode using low-pressure mercury lamp and interference filter for 253 nm. Laser pulse width, FWHM, was about 4 ns (PSX-100) in the case of quenching rate measurements (Valk *et al* 2010), and 33 ns in the case of intensity ratio measurements in pulsed mode (Paris *et al* 2004).

Next, a scatterer dispersed the beam, ensuring homogeneous illumination of the cathode. The diameter of the semi-transparent area of the cathode was 18 mm. Changing the distance between the discharge chamber and the scatterer enabled us to change the flux density of initial electrons, $\boldsymbol{\Gamma}_{e0}$.

Radiation from the discharge was focused with an achromatic quartz lens of 75 mm in focal length on the input slit of a MDR-23 monochromator. The linear dispersion of MDR-23 monochromator was 1.3 nm/mm. A photomultiplier (PM) with rise time of about 0.5 ns (PMH-100-4, Becker & Hickl GmbH) in photon-counting mode was used to detect the radiation from the discharge. The photocathode of the PM was cooled down to −20°C with the flow of cold air.

For quenching rate measurements, digital oscilloscope Tektronix TDS 540B with time resolution of 0.5 ns recorded the PM pulses. The laser flash via a high speed photodiode was used to trigger the oscilloscope.

The relative spectral sensitivity of the entire optical system was determined using a tungsten lamp and a deuterium lamp whose spectral characteristics were known. The instrumental function of the optical system, $F(\lambda)$, was recorded for every d for mercury line at 404.7 nm by illuminating the discharge gap with the mercury lamp.

Pictures of the discharge were taken using Apogee Alta 16-bit CCD camera with dynamical range of 65536 levels. Size of one pixel was 12 μm, with total of 2048×122 pixels. Interference filter for 337 nm was used in front of the camera to reduce chromatic aberration and disinclined radiation. The distance between the discharge chamber and CCD camera was chosen as long as possible – 3.58 m – limited only by our lab room size. Although the interference filter for 337 nm also helped to significantly reduce the influence of ambient light, the work had to be still carried out in total darkness during nighttime.

4.3. Adjustment of the set-up

Achieving excellent electrode parallelism was important, since small variation in d would also result in small variation in E. Small variation in E, however, produces quite significant changes in electron number density and in current density since α is exponentially related to E. This means that a small variation in E can have significant effect on i. In non-homogenous electric field the discharge current converges to regions of higher E, and the electric field becomes even more distorted due to space charge field, rendering the measurements unreliable, since most of the optical radiation is emitted from regions of higher E.

Electrodes were set parallel with the help of a He-Ne laser. Laser beam was directed trough a small hole with diameter of 1 mm in an A4 sized paper from a distance of 2 m to the anode. For this operation the lens and scatterer were removed. There were two reflections on the paper – one, more intense, coming from the cathode, and the other, less intense, from the anode. This was possible, since the cathode was semi-transparent. Both reflections were directed back to the source by adjusting the discharge chamber and the position of the cathode relative to the anode. If both reflections coincided, a set of interference rings appeared on the paper. The maximum angle of declination becomes 1 mm/2 m = 0.03 deg. For an electrode with diameter of 18 mm we get Δd = 0.03 deg·18 mm = 0.01 mm. Electrode parallelism, or in essence homogeneity of the macroscopic electric field, was also verified experimentally by photographing the discharge. This topic is discussed in detail in section 6.1.

Correct determination of d was very important, because the calculated reduced electric field strength, E/N, directly depends on d. The discharge chamber had to be opened and put back together each time the cathode was replaced. After setting electrodes parallel to each other, the reading of the dial gauge, used for

measuring the distance between the electrodes, and the actual distance between the electrodes, d, had to be matched again. The distance could not be determined from the reading for zero d, since, in this case, electrodes would have to come into contact, which could damage the delicate aluminum coating of the cathode.

For small d the capacitance between the cathode and the anode can be approximated by the formula for parallel-plate capacitor, where capacitance, $C(d)$, is proportional to the reciprocal of the distance between the electrodes:

$$C(d) = a \cdot \frac{1}{d + d_0} + C_0 \,. \tag{4.2}$$

Here a is a constant, and C_0 is some residual capacitance that is independent of d. In our case C became almost constant, independent of d and equal to 36 pF at $d > 2$ mm, thus $C_0 = 36$ pF. Rearranging terms in relation (4.2), we see that:

$$d(C) = a \cdot \frac{1}{C - C_0} - d_0 \,. \tag{4.3}$$

By plotting the reading of the dial versus reciprocal of $(C - C_0)$, the reading corresponding to zero distance, d_0, can be determined from the intercept of the respective regression line. Results of two such experiments are shown in figure 4.2. In order to avoid accidental contact, special attention has to be paid to the

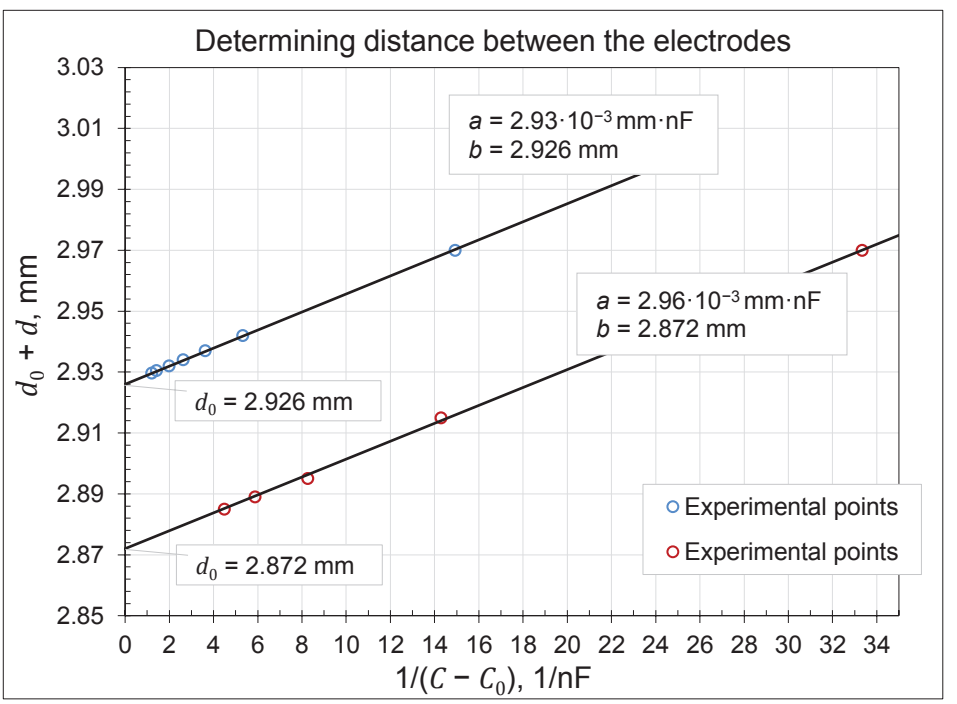

Figure 4.2. Determining d_0 from the capacitance between the electrodes.

adjustment of distance at high values of capacitance. One can see that the points neatly lie on a straight line, and that the inter-electrode distance, d, for which the capacitance becomes infinite, $C \to \infty$, does not correspond zero reading. Notice that the slopes of both regression lines are almost equal. After determining d_0, the zero-adjustment ring of the gauge was moved to this position. Now, reading of the dial corresponds to actual distance between the electrodes.

4.4. Working range of the set-up

Working range of the discharge chamber is presented in figure 4.3. Although we could choose combinations of U_d, N, and d arbitrarily, the point at which we actually get non-self-sustaining discharge is determined by the form of the Paschen's curve for our experimental set-up. The background and reasons for obtaining such a curve were explained in section 2.4. The black line in figure 4.3 represents experimentally determined Paschen's curve for air under conditions similar to ours (Dakin *et al* 1974).

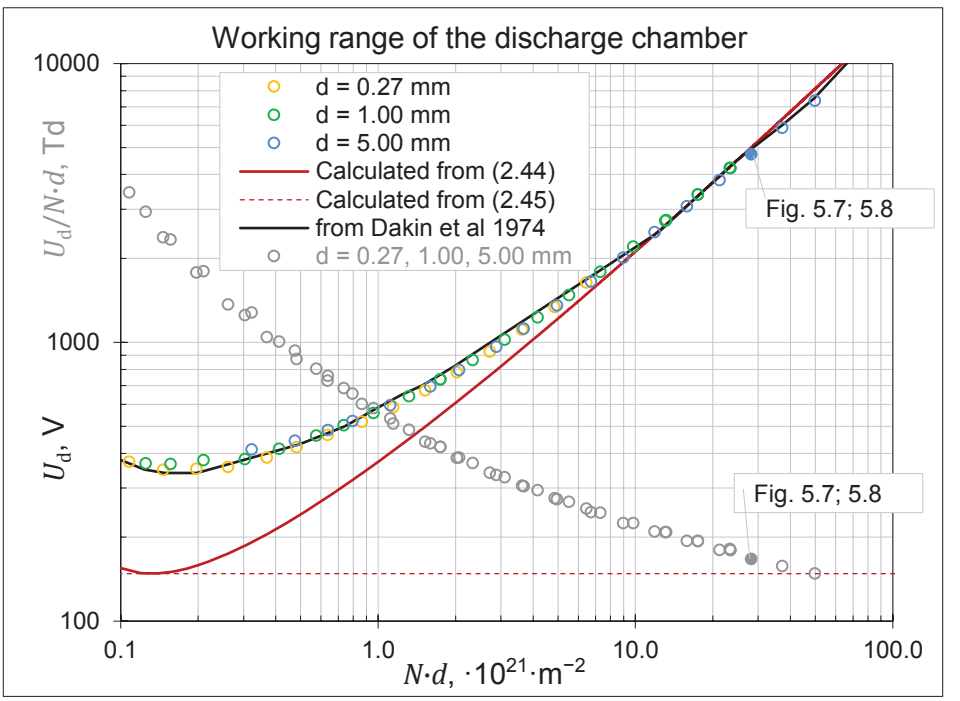

Figure 4.3. Working range of the set-up. Paschen's curves with selected experimental points for dry air (Paris *et al* 2005). The red line represents calculated breakdown voltage according to relation (2.44), with coefficients A and B for air taken from table 2.1, and $\gamma_{se} = 0.118$. The highlighted filled points correspond to conditions: d = 5.00 mm; p = 176 Torr; i = 1.36 μA; U_d = 4714 V; T = 298 K; $N = 5.70{\cdot}10^{24}$ m^{-3}; $N{\cdot}d = 28.5{\cdot}10^{21}$ m^{-2}; E/N = 165 Td. Spectrum scanned under these conditions can be seen in figures 5.7–5.8.

If U_d reaches U_{br}, the discharge transforms to self-sustaining, i.e. breakdown occurs. This can only happen for an instant, since it takes time, more than $r \cdot C_0 = 2.4$ ms, for U_d to reach U_{br} again. If U_{br} is reached again, another breakdown, or spark discharge, occurs. Typically, sparkling damaged the cathode to a point where it was impossible to get steady discharge current even at voltages well below U_{br}. This meant that the cathode had to be replaced.

The discharge chamber could also be operated at conditions where U_d remains well below U_{br}. In this case, initial electron just drift from cathode to anode without any significant effects, since their energy would be too small for avalanche growth. This option was used for conditioning and preparing each cathode for the first use. In conclusion, experimental points, measured at different pressures and gap distances, inevitably produce a curve that is very similar in form to Paschen's curve for a given gas mixture and cathode material.

The form of the Paschen's curve also explains how the discharge chamber enables to investigate processes at different E/N values by altering gap distance, d. Notice that E/N equals $U_d/N \cdot d$, and a decrease in $N \cdot d$ is accompanied by corresponding decrease in U_d. The corresponding decrease in U_d is, however, smaller, and we get an overall increase in E/N. In figure 4.3 reduced field strength as a function of $N \cdot d$ is shown in grey for the presented experimental points. Consequently, for the presented experimental points, decrease in U_d and $N \cdot d$ produces an overall increase in E/N from about 150 Td to 3500 Td.

4.5. Measuring procedure

Before each experiment certain procedures were carried out to assure the reliability of the measurements. Firstly, the discharge chamber was exhausted down to 0.005 Torr for about an hour. Then, a small gas flow was allowed from the MFCs, while pressure remained in the range of 0.1–1 Torr. If the chamber had been opened for replacing the cathode, then the chamber and inlet tubing were heated to about 70ºC with the help of a hot air gun. The minute fresh gas flow and heating helped to remove possible contaminants, mainly moisture, from the chamber. It also confirmed that there was no leakage into the system, other than from the flow controllers.

Reading of the dial versus the actual gap distance, together with electrode parallelism, was verified. This was done by one quick measurement of capacitance at $d = 0.01$ mm. If everything is as should be, the capacitance, C, should be about 0.3 nF. By further reducing d, to about 1/3 of minimum graduation, the capacitance should start to rise very steeply, up to about 500 nF. This confirms that the electrodes are not touching each other at 0.003 mm, and it also ensures parallelism of the electrodes.

Next, emission current, i_0, was measured at about $U_d = 80$ V. Typical emission currents were in the range of 0.1–0.5 nA. This assured that the wiring was intact, equipment was working, and charge carriers were available for avalanche growth. Then, voltage was raised to a point where the discharge current was

around 100 nA, and kept on for about 15 min to prepare the cathode. This procedure was useful since the discharge current would be more stable during the following measurements. Finally, radiation from the discharge gap was examined. The monochromator was set to register signals at 337 nm. If the equipment was well adjusted, there should be a measurable signal even at currents as low as 10 nA. As there is very little natural light at 337 nm, there should be very little signal when the voltage is turned off. This guarantees that ambient light does not penetrate our shielding.

The distance between the electrodes, d, was set to the required value. Commonly used distances were: 0.35 mm, 0.70 mm, 1.40 mm, 2.80 mm and 5.60 mm. Then, quartz lens between discharge chamber and the monochromator was adjusted to pick up the maximum amount of radiation available. Optics was adjusted meticulously before measurements were carried out with the help of a laser beam. As most of optical radiation is emanated from a thin layer near the anode, and the anode was the electrode which actually moved by design, it was useful to readjust the lens each time the distance, d, was changed.

Next, gas pressure was set to an appropriate value and left to stabilize for about one minute. Commonly used pressures, p, were: 0.5 Torr, 1.0 Torr, 2.0 Torr, 4.0 Torr, 8.0 Torr, 16 Torr, 32 Torr, 64 Torr, 128 Torr, 256 Torr, 512 Torr, 760 Torr. Generally, measurements were carried out by starting from lower pressures, and then moving up on the given sequence. With regard to figure 4.3, experimental points were measured one by one, gradually moving from the left to the right.

After setting d and p, voltage, well below U_{br}, was applied and the discharge current was monitored. Voltage was gradually increased, until the current reached about 2 μA. Current was left to stabilize for about 30 s, which typically meant asymptotical decrease up to 10%. Next, the investigated spectrum was recorded, the voltage was turned off, and pressure was changed for the next value. Typically, measurement were carried out for a set of currents and pressures at constant d, since changing d would also imply adjustment of optics.

After completing a set of measurements at different pressures and/or currents, the distance, d, was changed for the next value and the described procedure was started all over again. For one set of measurements at some d and p the time spent would be around 10 min. About 10 hr was required to complete a set of measurements for all different combinations of d and p.

As most of the equipment was computer-controllable, measuring procedure was mostly carried out automatically by the computer. Special programs were written for each experiment included in this thesis. Typically, the voltage was applied manually and, after the current had stabilized, an automatic measurement program was executed, which primarily dealt with storing of the acquired data and adjustment of the wavelength at which measurements were taken.

After measurements were completed all instruments were turned off. Slow gas flow was retained for about 5 min. Then, valve 3 was closed and the pump was turned off. Pressure inside the chamber was raised to about 1.2 atm. Next, gas flow rate into the chamber was set to zero. Valves 2 and 3 were left untouched,

open. If there were a small leakage of high-pressure gas from the cylinders then pressure would not build up inside the flow controllers (small volume), as this could damage the pressure transducers inside, but spread throughout the system (large volume). It was assuring to start next series of measurements and see that the pressure inside the chamber was still well over the atmospheric pressure, ensuring no leakage of contaminants into the chamber.

4.6. Accuracy of *E/N* inside the discharge

The externally applied macroscopic reduced field strength, E/N, in the discharge gap was calculated from formulae (2.2) and (2.36) using the following experimental parameters with their corresponding uncertainties: U_a, ΔU_a = 0.1%·U_a + 2.5 V; i, Δi = 1%·i + i_f; r, Δr = 1 MΩ; T, ΔT = 2ºC + T_{in}; d, Δd = 1%·d + 0.01 mm; and p, Δp = 10%·p + p_f for $p \leq 10$ Torr and Δp = 1%·p + p_f for $p > 10$ Torr. Here p_f is the amplitude of pressure fluctuation, and i_f is the amplitude of current fluctuation during the scanning of spectrum. T_{in} is possible increase in temperature in the discharge gap due to the heat produced by the discharge, which is the topic of section 5.2. The combined uncertainty of E/N is depicted in figure 4.4. The field distortion produced by the charge carriers in the discharge is not incorporated in this analysis, but is discussed in section 5.3.

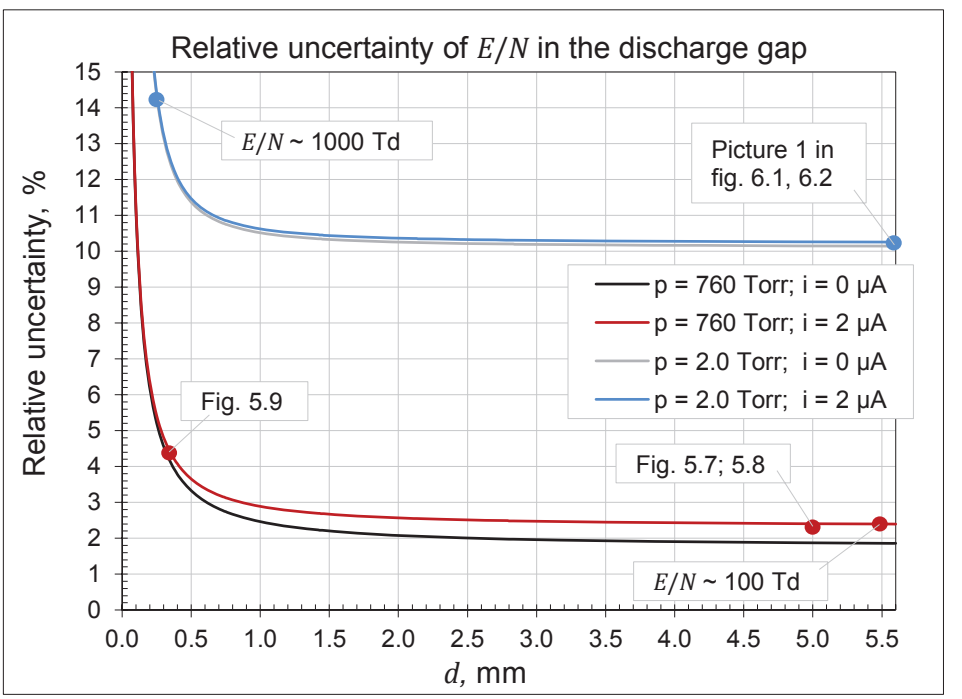

Figure 4.4. Combined relative uncertainty of E/N.

One can see that the uncertainty steeply increases for pressures below 10 Torr, since the pressure gauge uses micro Pirani sensor for pressures below 10 Torr. Uncertainty is at its lowest, 2–3%, at ~ 100 Td. At ~ 1000 Td the uncertainty steeply increases and is around 14%, since very high E/N values can only be reached by significant decrease in d. At 4000 Td, the highest E/N value at which the chamber operates, the uncertainty reaches 40%. Increase in i also increases the overall uncertainty in E/N, since Δi and ΔT both increase with increasing discharge current. In conclusion, the discharge chamber enabled to sustain dark discharge in the range from 100 Td (± 3%) to 4000 Td (± 40%).

Breakdown, or sparkling, would also occur more likely at smaller d values, since the breakdown field strength could be inadvertently reached due to increased uncertainty in E/N. Therefore, measurements were at first carried out with d between 0.5–5.6 mm, and only then with $d < 0.5$ mm. Often sparkling damaged the cathode to a point where it was impossible to get steady discharge current even at voltages well below U_{br}. This meant that the cathode had to be replaced.

5. MODELLING OF PROCESSES UNDER INTEREST

5.1. Distribution of charges in the discharge gap

Generally, experimental quantities under interest are rarely measured directly, but are often calculated indirectly from some quantities that can be measured directly. Relating the measured quantities correctly to actual physical processes and variables under investigation demands for models that unambiguously relate measured quantities to quantities under interest.

In this work the principal measured quantities are: distance between the electrodes, d; HV source output voltage, U_a; discharge current, i; gas temperature, T; gas pressure, p; and emission intensity, I_λ, at selected wavelengths. These quantities are used further as input variables in models for obtaining the results of this thesis. Such calculations only return correct results, if the models and assumptions implemented are in fact valid. In this chapter we present models that relate measured quantities to the results obtained in this work.

Most important of these models is the one that relates measured discharge current to the current produced by different charge carriers. This is one of the core topics of gas discharge physics. The experimental method used in this work does not allow direct measuring of the discharge current produced by specific charge carriers, but the measured current is the sum of currents produced by all the charge carriers present in the discharge gap. There are several reasons why the distinction is important in the context of this work. Firstly, since only electrons are expected to be responsible for excitation of the investigated states, we only need the electron current waveform to relate the measured emission intensity waveforms to the actual decrease rate of excited particles. Similarly, for estimating the influence of space charge field, we need to know positive ion number density between the electrodes. Neither of these quantities can be measured directly.

To divide i between different charge carriers, a model proposed by Wen was used (Wen 1989). In this model, apart from the neutral molecules, four species of particles are considered: electrons, positive ions, unstable negative ions, and stable negative ions, marked by corresponding subscripts e, p, nu and ns. The same notation is also used in this work. This model can be used to stimulate avalanche current waveforms for a given set of swarm parameters and gap distances, d. For a parallel-plate gap of separation d, cathode at $x = 0$, anode at $x = d$, the above-mentioned definitions result in a set of partial differential equations, set (5.1), for electron and ion number densities. From these equations, and appropriate initial and boundary conditions, the density distribution of different species can be calculated as a function of coordinate and time. We can see that for a simplified case for which there are no negative ions, i.e. $\eta = 0$, $\delta = 0$, and no time dependence, the first equation readily transforms to simple and more comprehensible equation (2.22), presented in section 2.3. Also, if $\alpha = 0$, $\delta = 0$, we obtain equation (2.26).

The main reason for using set (5.1) for modelling of discharge current rather than more simpler models presented in section 2.3, is that this model also takes into account the formation and loss mechanisms of negative ions; that is attachment of electrons to oxygen molecules, resulting in formation of unstable negative ions; detachment of electrons from unstable negative ions, and conversion of unstable negative ions to stable negative ions.

$$\begin{cases} \dfrac{\partial \rho_{\mathrm{e}}(x,t)}{\partial t} + \boldsymbol{v}_{\mathrm{e}} \cdot \dfrac{\partial \rho_{\mathrm{e}}(x,t)}{\partial x} = (\alpha - \eta) \cdot \boldsymbol{v}_{\mathrm{e}} \cdot \rho_{\mathrm{e}}(x,t) + \delta \cdot \boldsymbol{v}_{\mathrm{e}} \cdot \rho_{\mathrm{nu}}(x,t) \\ \dfrac{\partial \rho_{\mathrm{p}}(x,t)}{\partial t} - \boldsymbol{v}_{\mathrm{p}} \cdot \dfrac{\partial \rho_{\mathrm{p}}(x,t)}{\partial x} = \alpha \cdot \boldsymbol{v}_{\mathrm{e}} \cdot \rho_{\mathrm{e}}(x,t) \\ \dfrac{\partial \rho_{\mathrm{nu}}(x,t)}{\partial t} + \boldsymbol{v}_{\mathrm{nu}} \cdot \dfrac{\partial \rho_{\mathrm{nu}}(x,t)}{\partial x} = \eta \cdot \boldsymbol{v}_{\mathrm{e}} \cdot \rho_{\mathrm{e}}(x,t) - (\delta + \beta) \cdot \boldsymbol{v}_{\mathrm{e}} \cdot \rho_{\mathrm{nu}}(x,t) \\ \dfrac{\partial \rho_{\mathrm{ns}}(x,t)}{\partial t} + \boldsymbol{v}_{\mathrm{ns}} \cdot \dfrac{\partial \rho_{\mathrm{ns}}(x,t)}{\partial x} = \beta \cdot \boldsymbol{v}_{\mathrm{e}} \cdot \rho_{\mathrm{nu}}(x,t) \end{cases} \tag{5.1}$$

Detachment acts as a secondary ionization mechanism that strongly affects the slope of the current waveforms. This effect is counteracted by conversion processes, since conversion reduces the number of unstable negative ions and, as a consequence, the number of detached, delayed, electrons. As a result, electrons are continuously produced from unstable negative ions even long after the first electron transit time. The drift and the production of these delayed electrons may result in an increasing after-current, provided that the ion conversion/ stabilization rate is not very high compared with the electron detachment rate. This increasing after-current will finally decrease due to the neutralization at the anode of those unstable negative ions which have not yet lost their electrons and the ion conversion/stabilization effect. Moreover, the delayed electrons may again produce ions. The production of these ions may last for several μs, if the lifetime of the unstable negative ion is much longer than the electron transit time (Wen 1989). This implies that we can have free electrons, detached from negative ions, present in the discharge long after the initial electrons produced by photoelectric effect have reached the anode. Therefore, only by using this more complicated set of equations, can we accurately model current waveforms in electronegative gases. A more detailed discussion on the choice of swarm parameters for the evaluation of the measured avalanche current waveforms is presented in Wen 1989. See also sections 2.3.2 and 2.3.5.

Set (5.1) was solved for our experimental conditions using formulae proposed by Wen (1989). Values of ionization and attachment coefficients and electron mobility were evaluated using two-term numerical Boltzmann equation solver BOLSIG+. Number densities obtained from set (5.1) can be related to measured discharge current, i, using formulae (2.39) to (2.41).

Solutions to set (5.1) can be seen in figure 6.3. The distribution of charge carriers is calculated for $d = 2.8$ mm and $d = 5.6$ mm, for the specific conditions indicated. Notice that for pure nitrogen there are no negative ions present in the

discharge, i.e. $\eta = 0$, $\delta = 0$. For steady discharge current mode in a semi-logarithmic plot the increase in electron number density results in a straight line, as predicted by relation (2.38). If $\eta = 0$, $\delta = 0$, the slope of this line is equal to α. Similarly, for pulsed mode experiments $i_e(t)$ was obtained from $i(t)$ by solving set (5.1). Obtained waveforms, red lines, can be seen in figures 5.5 and 5.6.

5.2. Gas temperature in the discharge gap

Another experimental parameter that could not be directly measured is gas temperature, T, in the discharge gap. For evaluating relation (2.2), gas temperature inside the discharge must be known. If the rise in temperature, T_{in}, due to power dissipation in the discharge is negligible, then gas temperature in the discharge can be read equal to the temperature of the discharge chamber.

To estimate possible rise in temperature, T_{in}, we first estimate the possible rise in anode temperature, as if all the input power is to be used to heat the anode, and the only cooling mechanism available was the conduction of heat out of the chamber by a steel rod to which the anode is attached. From the law of heat conduction we can find the maximum difference in temperature:

$$\Delta T_{\text{anode}} = \frac{P \cdot l_{\text{rod}}}{\kappa_{\text{steel}} \cdot S_{\text{rod}}} . \tag{5.2}$$

If $P \approx 2$ μA·5 kV ≈ 10 mW, $\kappa_{\text{steel}} \approx 0.1$ W/cm·K, $l_{\text{rod}} = 10$ cm, and $S_{\text{rod}} = 0.5$ cm^2, we obtain $\Delta T_{\text{anode}} \approx 2$ K. Thermal conductivity of this steel rod was intentionally underestimated, since there is a threaded connection between the brass anode and the steel rod. As the surface area and thermal conductivity of the anode are well above the used values, we can be sure that this is an overestimation, and the actual anode temperature is still very close to T.

We used the following formula (Kitayama and Kuzumoto 1999) for estimating gas temperature in the discharge gap relative to anode temperature:

$$\Delta T_{\text{gas}} = (1 - \chi) \frac{P \cdot d}{3 \cdot \kappa_{\text{air}} \cdot S_{\text{d}}} . \tag{5.3}$$

Now, if $\chi \approx 0$, $P \approx 10$ mW, $d \approx 5$ mm, $\kappa_{\text{air}} \approx 0.00026$ W/cm·K (at atmospheric pressure), we obtain $\Delta T_{\text{gas}} \approx 2.5$ K. This is again an overestimation. These results were added:

$$T_{\text{in}} = \Delta T_{\text{anode}} + \Delta T_{\text{gas}} . \tag{5.4}$$

In addition to power provided by the HV source, there is also power input from the mercury lamp. Since most of this radiation is removed by the interference filter for 253 nm, and there was no detectable rise in temperature of the interference filter itself, there should not be any energy left to increase the

temperature of the electrodes. In conclusion, gas temperature inside the non-self-sustaining discharge, T, can be read equal to the temperature of the discharge chamber for the set-up used in this work. However, as was pointed out in section 4.6, T_{in} was accounted as a component of measurement uncertainty: $\Delta T = 2^{\circ}\mathrm{C} + T_{\mathrm{in}}$.

5.3. The influence of space charge field

The cumulative charge of different charge carriers present in the discharge gap distorts the externally applied and initially homogeneous electric field calculated from formula (2.36). In principle, formula (2.36) gives the correct value only if the discharge current equals zero. To overcome this problem, we estimate the field strength, E_{ρ}, produced by these charges relative to the externally applied field, E.

To find E_{ρ}, we employ Poisson's equation for electrostatics and consider, for the sake of clarity, solely the one-dimensional case. The maximum of the space charge field can be found from:

$$E_{\rho}(t) = \frac{e}{\varepsilon_0} \cdot \int_0^d \rho_{\mathrm{p}}(x,t)\, dx\,. \tag{5.5}$$

Here ε_0 is electric constant. In formula (5.5) we have included only the contribution of positive ions, since positive ion number density exceeds other charged particle densities. This can be easily explained by considering that the production of every new electron is related to production of one new positive ion, but only small part of electrons is attached, forming negative ions. Consequently, we have always more positive ions than negative ions. At steady discharge mode the flux of positive ions onto cathode must be equal to the flux of electrons onto anode. Because electron mass is much smaller than the mass of ions, the mobility of electrons is also much higher than the mobility of ions. From relation (2.33) we can conclude that these fluxes can be equal only if number densities differ about the same amount as mobilities, since the same electric field is applied to both species. Therefore, E_{ρ} is essentially determined by positive ion number density.

Relation (5.5) can be modified and directly related to measured quantities. Firstly, formula (2.39) can be used to relate E_{ρ} to the total number of positive ions:

$$E_{\rho}(t) = \frac{e \cdot n_{\mathrm{p}}(t)}{\varepsilon_0 \cdot S_{\mathrm{d}}}\,. \tag{5.6}$$

Secondly, the total number of positive ions present in the discharge gap is related to the current produced by positive ions in the external circuit by formula (2.40):

$$n_{\mathrm{p}}(t) = \frac{i_{\mathrm{p}}(t) \cdot d}{e \cdot \mu_{\mathrm{p}}(p) \cdot E} \ . \tag{5.7}$$

By inserting relation (5.7) into relation (5.6), we obtain:

$$E_{\rho}(t) = \frac{i_{\mathrm{p}}(t) \cdot d^2}{S_{\mathrm{d}} \cdot \varepsilon_0 \cdot U_{\mathrm{d}} \cdot \mu_{\mathrm{p}}(p)} < \frac{i(t) \cdot d^2}{S_{\mathrm{d}} \cdot \varepsilon_0 \cdot U_{\mathrm{d}} \cdot \mu_{\mathrm{p}}(p)} \ . \tag{5.8}$$

Since i is always greater than i_{p}, we can use the total current for evaluating E_{ρ}. In this work the discharge current, in continuous discharge mode, remained in the range of 0.5–2 μA, corresponding to $E_{\rho}/E \sim 0.01$–4%. For example, for $d = 5$ mm, $p = 176$ Torr, and $T = 298$ K, we obtain $N \approx 5.70 \cdot 10^{24}\ \mathrm{m}^{-3}$, and $N \cdot d \approx 28.5 \cdot 10^{21}\ \mathrm{m}^{-2}$. From figure 4.3 we see that the corresponding voltage, U_{d}, should be about 4.7 kV, and we get $E \approx 9 \cdot 10^5\ \mathrm{V \cdot m}^{-1}$. From relations (2.3) and (5.8) we obtain for $i = 1.36$ μA and $\mu_{\mathrm{p}}(176\ \mathrm{Torr}) \approx 10 \cdot 10^{-4}\ \mathrm{m}^2/\mathrm{V \cdot s}$ (Badaloni and Gallimberti 1972) that $\boldsymbol{v}_{\mathrm{p}} \approx 900$ m/s, and $E_{\rho} < 3 \cdot 10^3\ \mathrm{V \cdot m}^{-1}$. Consequently, $E/N \approx 165$ Td, and $E_{\rho}/E < 0.4\%$.

Still other reasons exist, why the initially homogeneous electric field may get distorted. As was pointed out in Pancheshnyi 2006, partial filamentation of the discharge or local electric field reinforcement near the imperfections of the electrode surfaces can become apparent at very low-distance measurements. To exclude this possibility, the discharge gap was investigated photographically. No filamentation was detected. Selected pictures are presented in figures 6.1–6.2.

The absence of filamentation can be also explained by theoretical considerations (Paris *et al* 2006). The anode was polished with an abrasive (grain size 0.2 μm) to mirror quality. The local unevenness of the finished surface should be less than the grain size. The enhanced electric field near the protrusions of 0.2 μm in size could stretch into the inter-electrode space up to about 1 μm from the electrode surface. The mean free path of an electron in air at atmospheric pressure is about 0.5 μm, and it increases with a decrease in pressure. Thus, on average, an electron can undergo two or less collisions in the enhanced field near the anode. The EEDF remains invariable at such a short distance in this region and retains the shape obtained in the uniform field between the electrodes. As a result, the spectral distribution of the radiation from this near-anode region should be the same as that generated in the undisturbed field region. Moreover, as the region of the enhanced field forms a small part of the discharge gap with the undisturbed homogeneous field, the radiation from this region constitutes only a small fraction of the total radiation. Imperfections on the cathode could also cause discharge filamentation due to the increased electron emission in the enhanced electric field. If the macroscopic electric field exceeds the value of about $10^7\ \mathrm{V \cdot m}^{-1}$, a considerable field emission of electrons from the cathode would occur (Dutton 1978). In our experiments, the macroscopic electric field strength never exceeded the value of $7.8 \cdot 10^6\ \mathrm{V \cdot m}^{-1}$.

In conclusion, if the discharge current is kept low and there is no filamentation due to surface imperfections, the uncertainty in E/N can be estimated as depicted in figure 4.4, since the additional uncertainty arising from the influence of E_ρ is much smaller, i.e. $\Delta E > E_\rho$.

5.4. Synthetic spectrum of investigated transitions

In order to compare the intensities of the investigated bands and determine corresponding intensity ratios, $R_{\lambda 1/\lambda 2}$, we first calculated simulated, or synthetic, spectra for these transitions. Note that each vibrational transition is further divided between numerous rotational energy levels, so the intensity of entire rotational band has to be determined. In principle, this could be achieved by just adjusting slits of the monochromator so that entire rotational band could be registered at once. There is, however, small, but still significant, overlapping between the FNS 0–0 and SPS 2–5 bands, so scanning the band and finding band intensities by employing synthetic spectra gives better results. First, we should point out that the measured spectrum corresponds to convolution, $\Phi(\lambda)$, of the actual spectrum or, in this case, synthetic spectrum, $SP(\lambda)$, and instrumental function, $F(\lambda)$:

$$\Phi(\lambda) = \int_{\lambda_1}^{\lambda_2} SP(\lambda - x) \cdot F(x)\,\mathrm{d}x\,. \tag{5.9}$$

The instrumental function tends to depend slightly on inter-electrode distance, d, and not only on slit widths; therefore, the instrumental function of the entire system was recorded for every d each time spectrum was recorded.

Let us start with SPS 0–0 transition, described by process (3.9). Potential energies of these states, relative to ground state, are approximately 11.0 eV and 7.3 eV. Potential energy functions for these states can be described by Klein–Dunham coefficients, $Y_{i,j}$. Values for these coefficients were obtained from Hartmann and Johnson 1978 and Naghizadeh-Kashani *et al* 2002, and we do not present these here. Firstly, we calculated $G(0)$, $B(0)$, and $D(0)$ from formulae (3.5) and (3.7) for both, upper (C, m = 4) and lower (B, m = 6), states. In a first approximation, rotational term energy can be found from formula (3.6), but as this formula does not take into account splitting of degenerate levels, we used more advanced formulae presented in Naghizadeh-Kashani *et al* 2002. The reason is that here we have both, upper and lower, $^3\Pi_u$ states, i.e. triplet states. These formulae for rotational terms are very similar to (3.6), but also take into account dependence on Ω. The upper C-state has a multiplicity of 3 and, therefore, the total angular momentum can take values Ω = 0, 1, 2. As a consequence, P- and R-branches are split into three sub-branches. Since $\Delta J = 0$ is not allowed when $\Omega = 0$, we only have two sub-branches for Q-branch. Corresponding wavelengths for these branches can be simply found from the difference in potential energy, as described by formula (3.4):

$$\lambda^{\Omega}_{v'\to v''}(J'') = \left(G_{\mathrm{C}}(v') - G_{\mathrm{B}}(v'') + F^{\Omega}_{\mathrm{C}}(v', J') - F^{\Omega}_{\mathrm{B}}(v'', J'')\right)^{-1}. \qquad (5.10)$$

Here $J' = J''$ (or ± 1) along with Ω must be varied to obtain the wavelengths for these branches. Transition intensities are, in essence, determined by relation (3.8). However, for electronic transitions $S_{\mathrm{J}}(J)$ depends on how the orbital angular momentum of electrons, the spin angular momentum of the electrons, the nuclear rotational angular momentum, and the nuclear spin all combine, i.e. couple. Different possibilities are often specified by so-called Hund's coupling cases, ranging from (a) to (e). These are idealized cases, and for a real molecule none of these is actually true. Most diatomic molecules can be viewed as belonging the idealized cases (a) and (b). If the orbital angular momentum is strongly coupled to the internuclear axis and spin angular momentum is strongly coupled to the orbital angular momentum, we have Hund's case (a). This approximation can be used for low values of J. With increasing J coupling weakens, and at some point Hund's case (b) gives better approximation than Hund's case (a). It has been pointed out (Naghizadeh-Kashani *et al* 2002) that the difference between these two cases only modifies the number of the satellite branches for which the intensity is negligible. Therefore, we considered only Hund's case (a). The difference hardly makes any difference in our case, since relatively wide $F(\lambda)$ was used anyway. As $S_{\mathrm{J}}(J)$, often called Hönl–London factors, depend on Ω and specific branch, we have three separate cases for $S_{\mathrm{J}}(J)$. For Hund's case (a) these factors are:

$$S^{\Omega}_{\mathrm{JP}}(J) = \frac{(J+1+\Omega)(J+1-\Omega)}{J+1};$$
$$S^{\Omega}_{\mathrm{JR}}(J) = \frac{(J+\Omega)(J-\Omega)}{J}; \qquad S^{\Omega}_{\mathrm{JQ}}(J) = \frac{(2J+1)\Omega^2}{J(J+1)}. \qquad (5.11)$$

Here again $\Omega = 0, 1, 2$ for P- and R-branches, and $\Omega = 1, 2$ for Q-branch. From relation (3.8) we can see that $S_{\mathrm{J}}(J)$ and $F(v, J)$ are both functions of J. Thus, $Q_{\mathrm{J}}(v, J)$ first increases with increasing J, because the multiplicity increases. As J increases, upper level population starts to decrease with increasing energy, which is determined by temperature, T. Therefore, at some point $Q_{\mathrm{J}}(v, J)$ starts to decrease again with increasing J, as exponential part of the function decreases more rapidly than $S_{\mathrm{J}}(J)$ increases. This results in a bell-shaped form.

To obtain the synthetic spectrum, $SP(\lambda)$, we must first determine the upper value for J. If $J > 30$ then $Q_{\mathrm{J}}(0, J')$ approaches zero for all branches and Ω values; therefore, we select $J = 0\ldots30$. Next, intensities of these transitions can be obtained from formula (3.8). In total we have 8 branches, and we get $8 \cdot 31 = 248$ transitions. Intensities obtained from relation (3.8) for these branches can be stacked, forming one long array SP_{j}, where $\mathrm{j} = 0\ldots247$. Similarly, from formula (5.10), we get 248 wavelengths, λ_{j}, corresponding to these intensities.

The preceding discussion is summarized in figures 5.1 and 5.2. In figure 5.1, wavelengths, $\lambda^{\Omega}_{0\to0}(J)$, for different branches as a function of rotational quantum number, J, are presented. Such plots are often called Fortrat diagrams. Fortrat diagram is independent of temperature, T, and it only shows us the transition wavelengths allowed by quantum mechanics. Which transitions actually occur, and their corresponding intensities, depend on upper lever population, determined by T, and Hönl–London factors. In figure 5.2, intensities calculated from relation (3.8) are presented for all 8 branches at wavelengths shown in figure 5.1. For P-branch and $J = 0$ we obtain $\lambda^{2}_{0\to0}(0) = 337.07$ nm. $\Phi(\lambda)$ has a maximum around 337.1 nm, because there are more intense lines per nm than elsewhere.

Rotational band structure for SPS 2–5 transition, process (3.15), can be obtained similarly by simply replacing respective vibrational quantum numbers. Since the overall change in energy is smaller, the expected band should appear at longer wavelengths. Rather accurate estimate can be obtained from formula (5.10) by omitting rotational terms: $[G_C(2) - G_B(5)]^{-1} = 394.2$ nm. Results are shown in figure 5.3. Compared to SPS 0–0 transition, the band is spread over a wider range. The longest wavelength corresponding to $J = 0$ for P-branch at 0 K is $\lambda^{2}_{2\to5}(0) = 394.24$ nm.

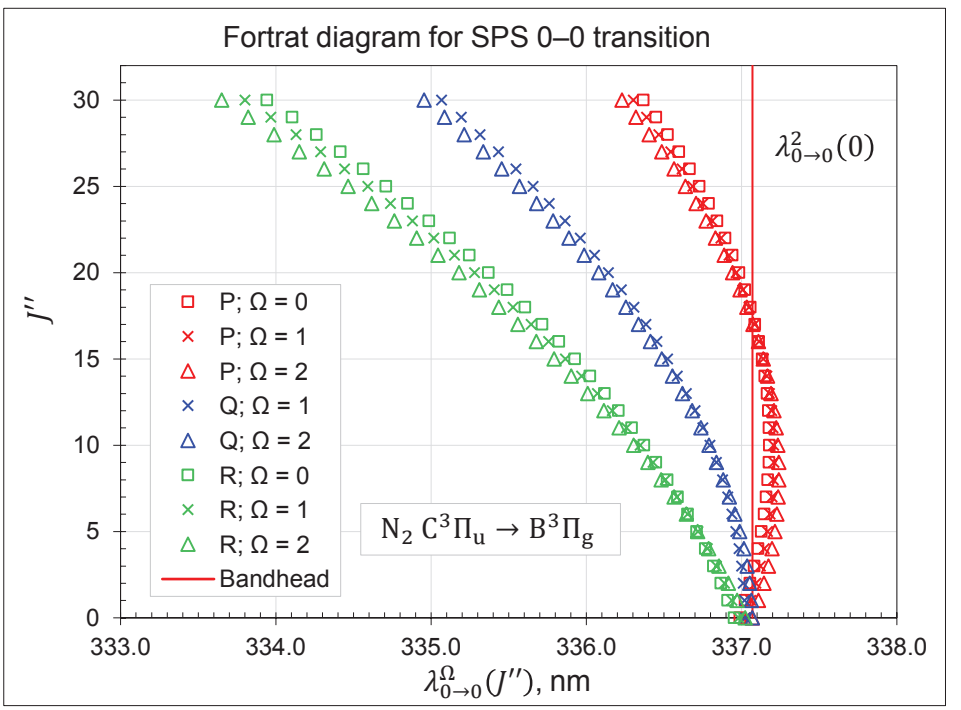

Figure 5.1. Fortrat diagram with wavelengths calculated from formula (5.10) for SPS 0–0 transition, with $J = 0\ldots30$. All 248 wavelengths for P-, R-, Q-branches with their corresponding sub-branches are shown.

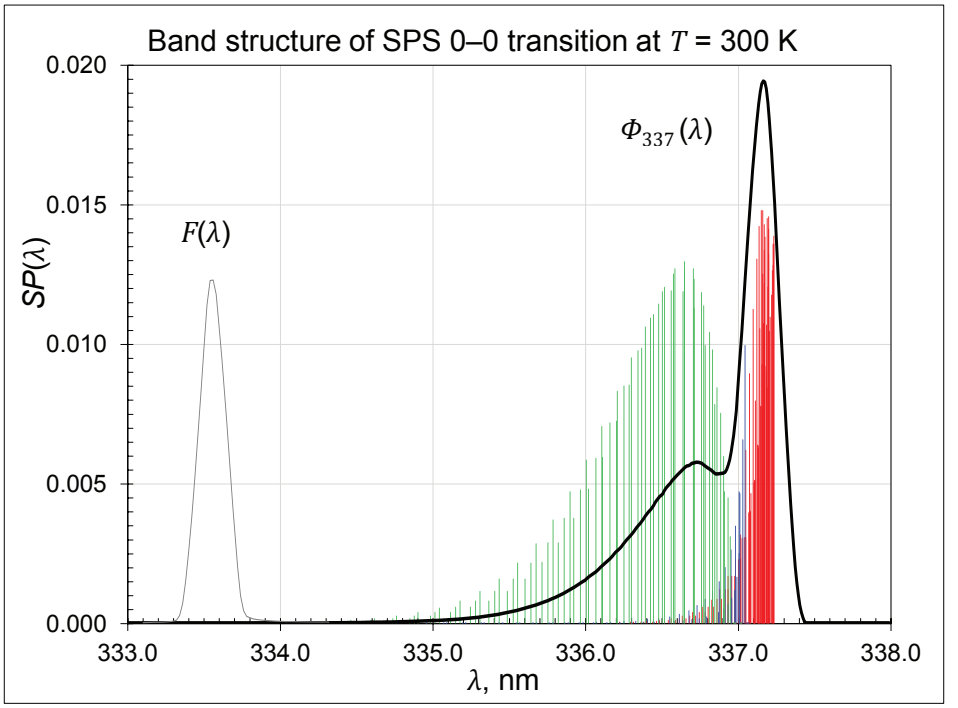

Figure 5.2. Rotational band structure of SPS 0–0 transition, with $J = 0\ldots30$ at $T = 300$ K. All 248 transitions, corresponding to P-, R-, Q-branches, are shown. Sub-branches are not explicitly specified. The black line, $\Phi(\lambda)$, is the convolution calculated from formula (5.9). Rotational line intensities are normalized so that the sum of intensities of all the 248 lines is equal to one. For clarity, this normalization coefficient is not shown in formula (3.8). Intensities of $F(\lambda)$ and $\Phi(\lambda)$ are selected suitable for the sake of clarity. $F(\lambda)$ is the instrumental function registered at 404.7 nm for slit widths of 0.17 mm and 0.15 mm in all presented figures.

Modelling of the rotational structure of N_2^+ FNS 0–0 transition, process (3.10), is somewhat simpler. Again, omitting rotational terms, we obtain from formula (5.10): $[G_{\mathrm{Bi}}(0) - G_{\mathrm{Xi}}(0)]^{-1} = 391.14$ nm. Here, similarly, we first calculated $G(0)$, $B(0)$, and $D(0)$ from formulae (3.5) and (3.7) for upper (Bi, m = 4) and lower (Xi, m = 7) states. Since both states are $^2\Sigma$ states, Hund's case (b) always applies (Naghizadeh-Kashani *et al* 2002), and we do not have a Q-branch, since it is prohibited. Likewise, both P-branch and R-branch further split into two separate branches, and we get 4 branches in total. To obtain the synthetic spectrum, we first need to evaluate $F(v, J)$ for this specific transition, before we can use formula (5.10). Similarly, we need Hönl–London factors for Hund's case (b) in formula (3.8). These formulae can be found from the above-mentioned literature. If we had simply used formula (3.6), we would still get the spectrum, but we would have no sub-branches and no fine structure. Obtained results are shown in figure 5.4. Here again we choose $T_{\mathrm{i}} = 300$ K, and $J = 0\ldots30$.

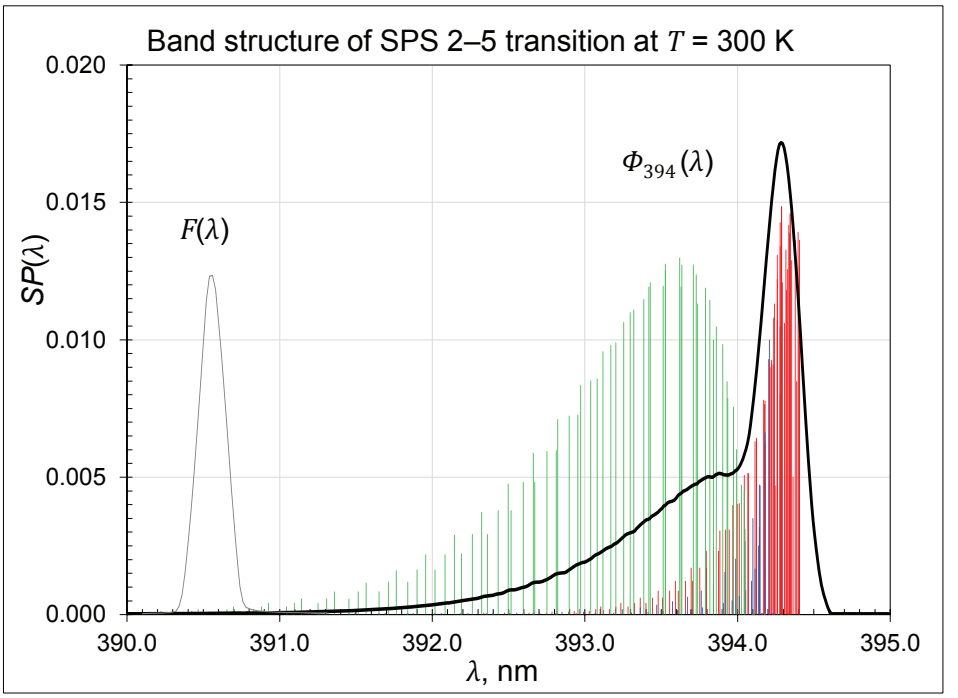

Figure 5.3. Rotational structure of SPS 2–5 transition, with $J = 0…30$ at $T = 300$ K.

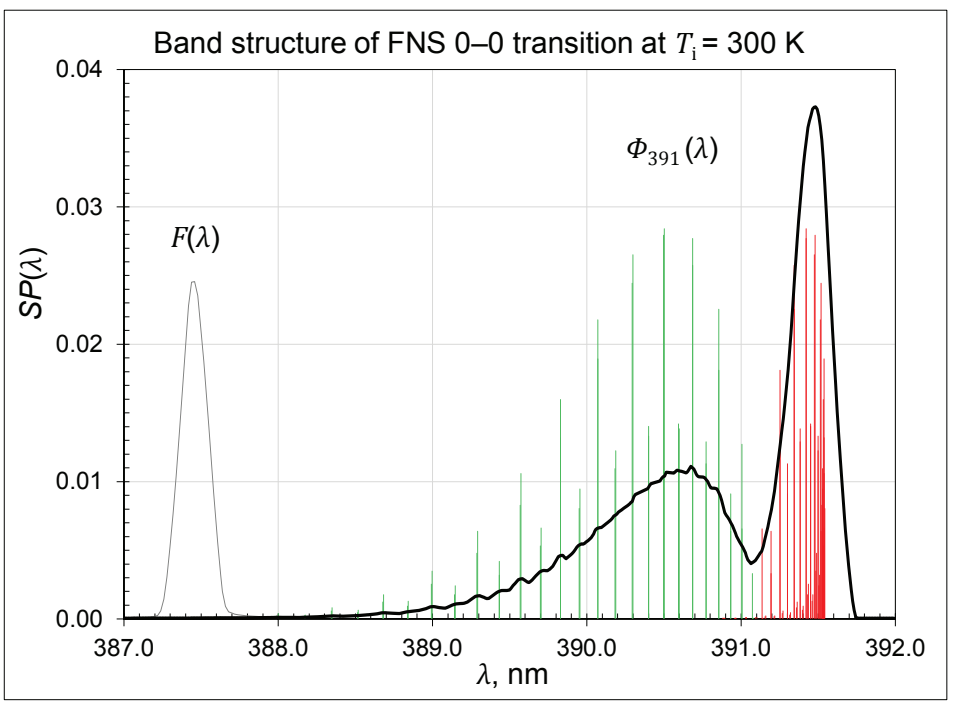

Figure 5.4. Rotational structure of N_2^+ FNS 0–0 transition, with $J = 0…30$ at $T_i = 300$ K. All 124 transitions of P- and R-branches are shown. Intensity of the rotational lines is normalized so that the sum of the intensities of all the 124 lines is equal to one. Intensities of $F(\lambda)$ and $\Phi_{391}(\lambda)$ are selected suitable for the sake of clarity.

These normalized band profiles, $\Phi_{337}(\lambda)$, $\Phi_{394}(\lambda)$, and $\Phi_{391}(\lambda)$ are subsequently used in section 5.6 for experimentally determining corresponding band intensities.

5.5. Quenching rates and lifetimes of upper states

Correct knowledge of natural lifetimes, τ_0, and quenching rate constants, k_q, for the upper states of the investigated transitions is important, since it is important to know the proportion of excited molecules that actually radiate. In this work quenching rates of $N_2(C^3\Pi_u, v' = 0)$ and $N_2^+(B^2\Sigma_u^+, v' = 0)$ states – upper states of the examined transitions – by N_2 and O_2 molecules must be known for evaluating relation (3.14) in air. Using different values for these constants, different values for $g(N)$ will be obtained. Quenching mechanisms and rates of these excited states are historically extensively studied, but as there are different values for these constants available in the literature, we decided to perform the measurements ourselves under our experimental conditions (Valk *et al* 2010).

In the case of pulsed non-self-sustaining discharge, used in this study for determining natural lifetimes and quenching rate constants, there are few electrons in the discharge gap during the decay period of excited states, since electrons are removed by the electric field. During the pause between laser flashes, the gas flow also removes reaction products that can accumulate in the case of stagnant medium. Number density of molecules in excited state is low in dark discharge, so interaction between excited particles can be excluded. However, the excitation mechanism is not selective, meaning that the discharge pulse also populates higher vibrational levels. Cascading from those higher levels can, in principle, influence our measurements.

To exclude the influence of rotational relaxation, we did not scan the transition band, but the widths of the slits were adjusted so that the registered phonon flux, $I_\lambda(t)$, corresponded to entire rotational band. Measurements were carried out at low pressures, so separation of N_2^+ FNS 0–0 transition from the R-branch of the N_2 SPS 2–5 transition was not necessary, because emission intensity from the N_2^+ FNS 0–0 transition far exceeds the emission intensity from the R-branch of the N_2 SPS 2–5 transition.

The measured emission intensity waveform for binary collisions, $I_\lambda(t)$, should correspond to the actual decrease rate of excited particles, as described by formula (2.19), if all these particles were excited in an infinitely short time interval. In practice, however, it is very difficult to excite particles in an infinitely short time interval, and the respective electron current pulse has a finite width, partly due to several different secondary processes. The following differential equation can be composed to describe excited particles number density as a function of time, which also takes into account the finite width of electron current pulse, $i_e(t)$:

$$\frac{d\rho^*(t)}{dt} = -\frac{1}{\tau} \cdot \rho^*(t) + a \cdot i_\mathrm{e}(t)\,. \tag{5.12}$$

Here $i_\mathrm{e}(t)$ is the electron component of the discharge current, and a is a coefficient of proportionality. Electron current was obtained from the measured total current by solving set (5.1). One can see that if $a = 0$, equation (5.12) transforms to simple equation (2.18), with solution described by formula (2.19). This also means that when electron current becomes zero, the decrease waveform should correspond to simple exponential decay, represented by relation (2.19). Solution to equation (5.12) can be expressed as follows:

$$\rho^*(t) = a_2 \cdot \int_0^t h(t-\tau) \cdot i_\mathrm{e}(\tau)\, d\tau\,, \quad \text{where} \quad h(t) = a_3 \cdot \exp\left(-\frac{t}{\tau}\right). \tag{5.13}$$

Therefore, solution to equation (5.12) can be viewed as the convolution of electron component of the discharge current and an exponential decay waveform, described by relation (2.19). Here a_2 and a_3 are coefficients of proportionality. Consequently, to obtain τ from the measured waveform, we need to deconvolve the measured intensity waveform $I_\lambda(t)$ and $i_\mathrm{e}(t)$. Deconvolution can be carried out using the convolution theorem by transforming these signals from the time domain to the frequency domain. In frequency domain, deconvolution can be carried out by simply dividing the two signals.

The preceding discussion is summarized in figure 5.5, where typical waveforms for $\mathrm{N_2}(\mathrm{C}^3\Pi_\mathrm{u}, v' = 0)$ state are shown. Firstly, a short laser pulse releases electrons from the cathode, which produce an electron current pulse, $i_\mathrm{e}(t)$, in constant electric field. Drifting electrons, in turn, excite small portion of molecules in the discharge gap. After initial electron pulse ends at about 50 ns, all the electrons produced by secondary processes are continuously removed by the field, and the rate of excitation approaches zero. These secondary electrons may be, for example, detached from negative oxygen ions, described by detachment coefficient, δ. Excited particle number density then decreases exponentially, according to relation (2.19). These excited molecules are lost due to radiative transition to another state, with a time constant τ_0, or due to collisional deactivation. From figure 5.5 we can see that for timescales $\tau > 20$ ns it is easy to determine τ, and separation of waveforms by deconvolution is not mandatory, since we could just start estimating τ from 50 ns, when the electron current approaches zero.

If, however, deconvolution is carried out successfully, there should not be any significant difference between lifetimes calculated from different time intervals, since the underlying process is the same. This means that, for example, if we calculated τ from yellow line starting from 50 ns without solving equation (5.12), or from black line by solving equation (5.12), the obtained lifetime should be exactly the same. In this way we can estimate how successfully the deconvolution was carried out, and how accurately the electron current pulse was calculated.

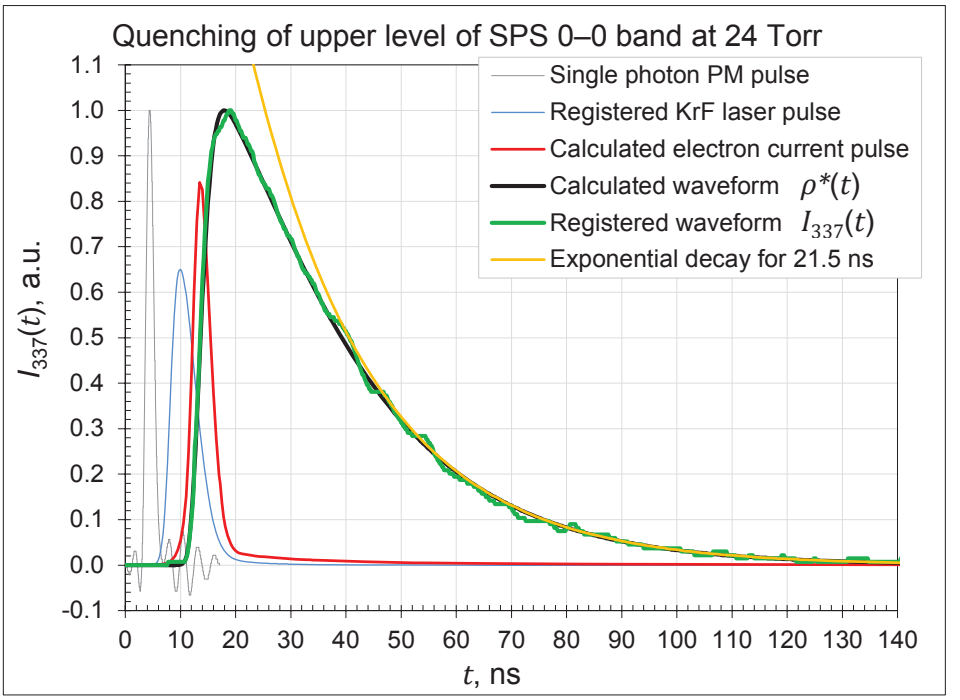

Figure 5.5. Typical pulses for $N_2(C^3\Pi_u, v' = 0)$ state at: E/N = (584 ± 23) Td; p = (24 ± 0.6) Torr; τ = (21.5 ± 1) ns; d = 0.70 mm. Gas mixture: 95% N_2, 5% O_2. $h(t)$ – exponential decay for 21.5 ns; $i_e(t)$ – calculated electron current. Amplitudes are selected suitable for the sake of clarity. Single photon PM pulse, laser pulse, and registered waveform are all oscillograms; other waveforms are calculated. The position of the laser pulse relative to other waveforms is not exact. Positioning of other waveforms is exact, since they are all parts of the same differential equation (5.12). The lifetime, τ, is long compared to the laser pulse and electron current pulse, and determining the lifetime is straightforward: the lifetime corresponds directly to the time constant of the exponential decay of the PM signal from about 50 ns, i.e. $\rho^*(t)$ and $h(t)$ coincide when $i_e(t)$ approaches zero.

At higher pressures quenching rate is higher and, consequently, lifetime is much shorter. Therefore, separation of waveforms by deconvolution becomes mandatory. This situation is depicted in figure 5.6. Now, correct knowledge of electron current waveform is important, since we cannot determine $h(t)$ directly. As can be seen from these figures, solution to equation (5.12), black line, coincides well with registered waveform, represented by green line.

For $N_2^+(B^2\Sigma_u^+, v' = 0)$ state the situation was more complicated. The main difficulty was that the lifetimes were very short and the correct results could only be obtained by deconvolution. Lowering pressure did not help, since the quenching rate for $N_2^+(B^2\Sigma_u^+, v' = 0)$ state by N_2 molecule was more than ten times greater than for $N_2(C^3\Pi_u, v' = 0)$ state (Valk *et al* 2010).

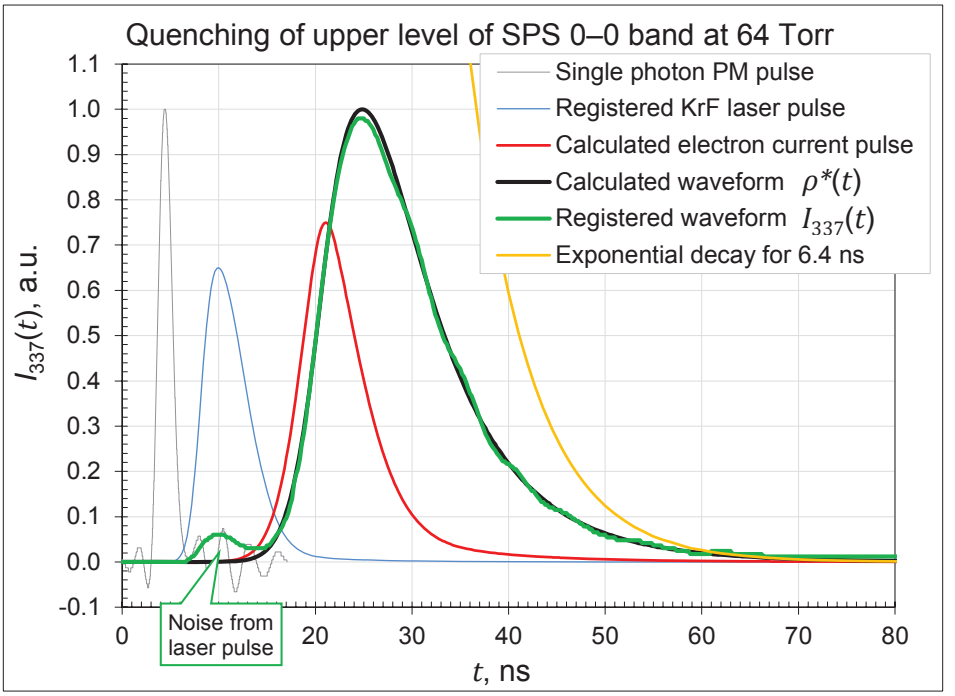

Figure 5.6. Typical pulses for $N_2(C^3\Pi_u, v' = 0)$ state at: E/N = (189 ± 8) Td; p = (64 ± 2) Torr; τ = (6.4 ± 0.7) ns; d = 2.80 mm. Gas mixture: 20% O_2, 80% N_2. There is some noise from KrF excimer laser (248 nm) at 337 nm.

Lastly, we cannot just deconvolve two signals measured by two different channels, since impulse responses for these channels may be different. In our case the difference was about 1–2 ns. This also had to be taken into account in clarity. It follows that the registered laser pulse, blue line, is the convolution of actual laser pulse and single photon PM pulse, etc. Since the timescales are short, even by using two different cables, could, in principle, result in different impulse responses for two identical oscillograph inputs. For these reasons the width of registered laser pulse in figure 5.5 appears to be wider than the resulting current pulse.

Remember from section 2.3.3 that the natural lifetime, τ_0, and the quenching rate constant, k_q, can be obtained from the slope and intercept of a regression line, composed for relation (2.20). To obtain the necessary data for composing such a line, a data set, corresponding to different lifetimes, τ, at different pressures, must be measured. To determine respective quenching rate constants for collisions with N_2 and O_2 molecules from k_q, quenching rate constant must be divided into two parts:

$$k_q \cdot N = k_{q\,N2} \cdot N_{N2} + k_{q\,O2} \cdot N_{O2}\,, \text{ where } \quad N = N_{N2} + N_{O2}\,. \tag{5.14}$$

Quenching by other species can be excluded, since number densities of these

species are very low. Consequently, to solve equation (5.14), we need to perform the described measurements in different nitrogen-oxygen mixtures. Yet, by increasing oxygen concentration we have less radiating molecules – further decreasing already weak signal. The above discussion is only true for binary collisions. Results of such measurements are presented in section 6.2.

To compare the intensity ratios of spectral bands measured at different pressures, we must take into account the proportion of excited molecules that actually radiate, and the proportion of excited molecules that are quenched by N_2 or O_2 molecules. If the spontaneous emission and the collisional quenching are the only processes of depopulation of an excited state at a given pressure and temperature, then the expected lifetime of an excited state can expressed by relation (2.20). The ratio of molecules, $g(N)$, that can radiate before being quenched is expressed by relation (3.14). The dependence of upper level depopulation on gas number density should, in principle, be cancelled out, if we multiplied each experimental point, $R_{\lambda 1/\lambda 2}(E/N, N)$, by a quotient:

$$G_{\lambda 1,\lambda 2}\,(N, N_0) = \frac{g_{\lambda 1}(N_0) \cdot g_{\lambda 2}(N)}{g_{\lambda 1}(N) \cdot g_{\lambda 2}(N_0)}\,. \tag{5.15}$$

This quotient represents the proportion of excited states at N that can radiate relative to those at N_0 ($p_0 = 100$ kPa, $T_0 = 0$°C). Based on this assumption a procedure for reduction of the measured intensity ratios to the standard conditions, N_0, can be composed (Paris *et al* 2005).

5.6. Intensity ratios of investigated transitions

Intensity ratios of the investigated bands $R_{391/394}(E/N,\ N)$, $R_{394/397}(E/N,\ N)$, $R_{391/337}(E/N,\ N)$ can be determined by using normalized band profiles $\Phi_{337}(\lambda)$, $\Phi_{394}(\lambda)$, and $\Phi_{391}(\lambda)$, obtained from synthetic spectra in section 5.4. Since the shape and location of the band are not functions of band intensity, we find a curve, $BF_1(\lambda)$, that best fits scanned experimental points:

$$\mathrm{BF}_1(\lambda) = a_{337} \cdot \Phi_{337}(\lambda) + b_{337}\,. \tag{5.16}$$

Here $\Phi_{337}(\lambda)$ is calculated from formula 5.9 for SPS 0–0 transition, as shown in figure 5.2, and a_{337} and b_{337} are freely selectable coefficients. The values of a_{337} and b_{337} were found by using the method of least squares, such that the curve $BF_1(\lambda)$ gave the best fit for the experimental points. In this way the intensity of each investigated transition band can be determined.

As the scale of the measured intensities covered many orders of magnitude, the linearity of the PM and the pulse counter was also verified. For that we used a light emitting diode for which the dependence between the junction current and emittance was well known. The dead time of the system was also measured

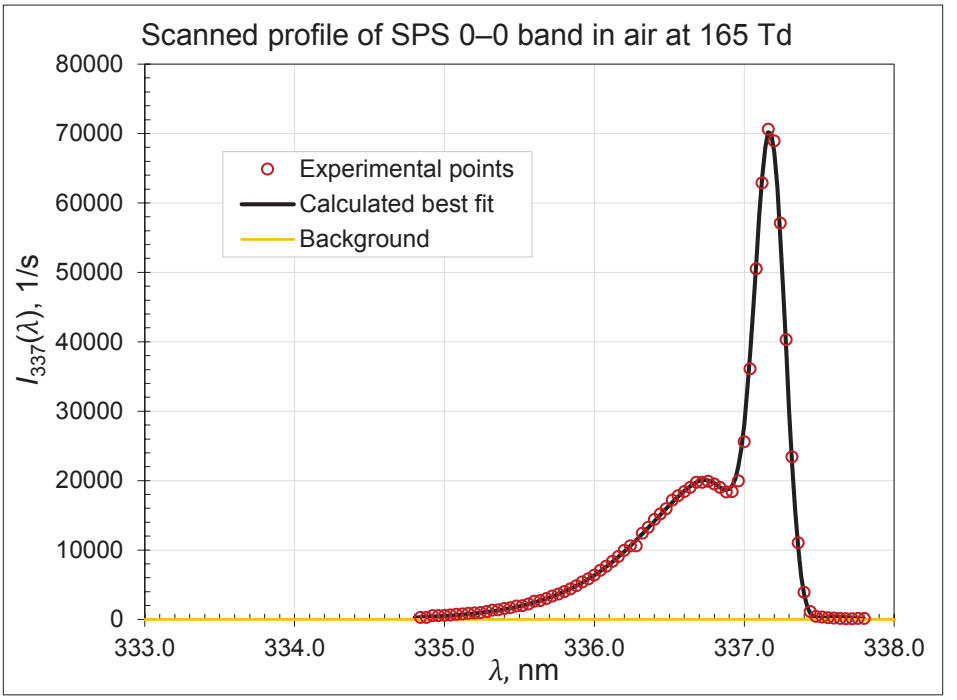

Figure 5.7. Experimental points scanned at intervals of 0.04 nm in dry air with MDR-23 at: $E/N = (165 \pm 5)$ Td; $d = 5.00$ mm; $p = 176$ Torr; $i = 1.36$ μA; $U_d = 4714$ V; $N = 5.70 \cdot 10^{24}$ m^{-3}; $E_\rho/E < 0.4\%$; $T = 298$ K; $T_{in} \approx 4$ K; $W_{mean} \approx 4.5$ eV. The underlying rotational structure is calculated for the temperature at which experimental points were scanned. The calculated best fit, black line, is: $BF_1(\lambda) = 162722 \cdot \Phi_{337}(\lambda) - 2$. Since $\Phi_{337}(\lambda)$ was normalized, the relative intensity of the entire band is equal to $a_{337} = 162722$, and the background, orange line, is $b_{337} = -2$. From Appendix A we can see that at 165 Td EEDF easily reaches 11.0 eV.

and taken into account when experimental points were prepared for comparison with the normalized band profiles.

An example for SPS 0–0 transition is presented in figure 5.7 (for steady mode, Paris *et al* 2005). In this case we first subtracted the scanned spectrum without the discharge, i.e. background, from experimental points before a_{337} and b_{337} were determined. One can see that the calculated profile coincides well with experimental points. It is also proved by the fact that the background is found to be very close to zero. Since the shape of the band, $\Phi_{337}(\lambda)$, should remain the same as the intensity changes, we can distinguish actual change in intensity from changes in the background. The scattering of experimental points, corresponding to lower intensities, has also less effect on a_{337}, since scattering is mostly random by nature and cancels out.

The coincidence of wavelengths of the model and experimental points was set manually by shifting the wavelengths of scanned experimental points. This

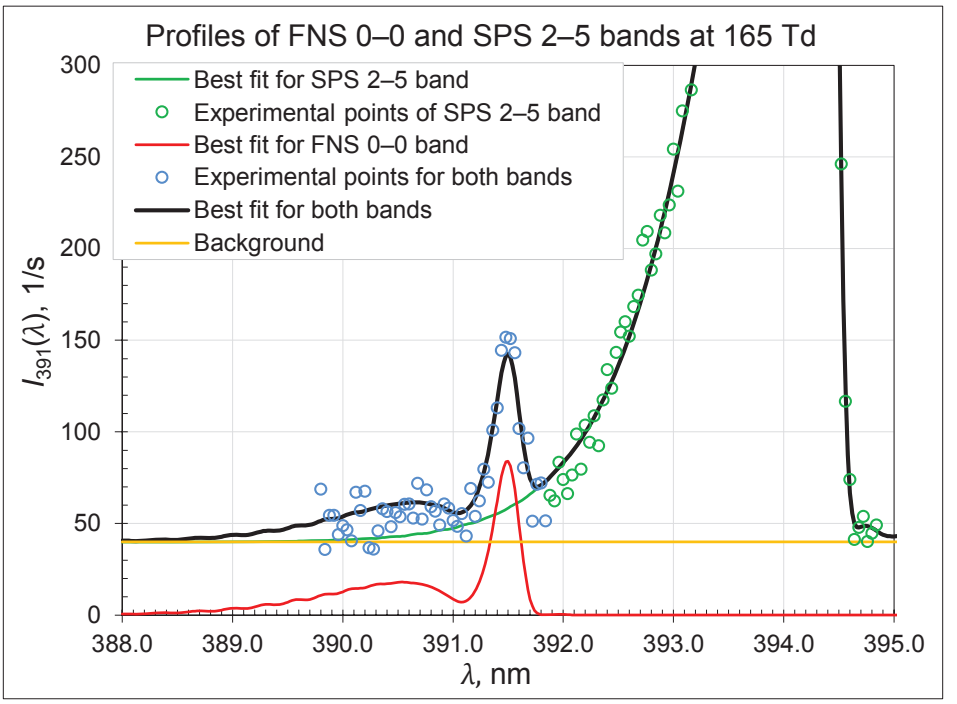

Figure 5.8. Experimental points and calculated best fit for SPS 2–5 and FNS 0–0 bands in dry air at: E/N = (165 ± 5) Td; d = 5.00 mm; p = 176 Torr; i = 1.36 μA; U_d = 4714 V; $N = 5.70 \cdot 10^{24}$ m^{-3}; $E_\rho/E < 0.4\%$; T = 298 K; $T_{in} \approx 4$ K; $W_{mean} \approx 4.5$ eV. The underlying rotational structure is calculated for T = 298 K for SPS 2–5 transition, and for T_i = 400 K for FNS 0–0 transition. The instrumental function, $F(\lambda)$, is the same for both bands. Calculated best fit for SPS 2–5 band, green line, is: $4716 \cdot \Phi_{394}(\lambda) + 40$. Therefore: $b = b_{394} = 40$. The calculated best fit for FNS 0–0 band, red line, is: $231 \cdot \Phi_{391}(\lambda)$. The calculated best fit for both bands, black line, is: $4716 \cdot \Phi_{394}(\lambda) + 231 \cdot \Phi_{391}(\lambda) + 40$. The intensity of the FNS 0–0 band is equal to $a_{391} = 231$, and the intensity of the SPS 2–5 band is equal to $a_{394} = 4716$. Consequently: $R_{391/394} = 231/4716 \approx 0.049$. At 165 Td EEDF barely reaches 18.7 eV, so very low intensity of FNS 0–0 transition is predictable.

shifting (up to ± 0.1 nm) was only necessary each time some component of the experimental set-up (lens, discharge chamber, etc.) was adjusted. In conclusion, determining the relative intensity of SPS 0–0 transition presented no problems, since SPS is one of the most intense systems of N_2, and there are no other overlapping bands in this region. Notice that the best fit was obtained at exactly the same temperature at which experimental points were registered. This also confirms that the model presented in section 5.2 is correct, and there is no significant rise in gas temperature between the electrodes. Even 10 K rise would easily show, since resemblance between the experimental points and the simulated spectrum would diminish.

For N_2^+ FNS 0–0 band circumstances are more complicated. This situation is depicted in figures 5.8 and 5.9 (for steady mode, Paris *et al* 2005). Since there is

still some radiation from the R-branch of the SPS 2–5 transition at wavelengths corresponding to FNS 0–0 band, formula (5.16) must be modified:

$$\mathrm{BF}_2(\lambda) = a_{391} \cdot \Phi_{391}(\lambda) + a_{394} \cdot \Phi_{394}(\lambda) + b \ . \qquad (5.17)$$

To use formula (5.17), we first divide measured experimental points into two groups. As with increasing temperature rotational structure spreads mostly towards higher energies, we can conclude that experimental points above about 391.9 nm correspond only to SPS 2–5 transition and background. These points are shown as green. Similarly, experimental points below 391.9 nm correspond to both bands: FNS 0–0 transition, R-branch of the SPS 2–5 transition, and background. These points are shown as blue. Next, the background was determined. For determining the background the more intense of the two transitions was selected. Typically, for low E/N values b was determined from SPS 2–5 transition, as shown in figure 5.8. When both a_{394} and b_{394} are calculated for the SPS 2–5 transition, green points, the obtained curve was subtracted from blue points. Now we have obtained experimental points without the influence from the R-branch of the SPS 2–5 transition and without background (these points are not shown in figures). The next step would be to find a_{391} using these prepared experimental points. For higher E/N values, over 700 Td, the background was calculated from FNS 0–0 rather than from SPS 2–5 transition. Now, if we add both profiles, green and red lines in both figures, we get a curve, black line, which should fit scanned spectrum in both regions. One can see that the simulated spectrum closely resembles the scanned spectrum.

Below 150 Td the FNS 0–0 band totally submerges into the R-branch of the SPS 2–5 band. At about 160 Td the FNS 0–0 band becomes detectable. From about 400 Td the FNS 0–0 band profile is easily detectable and the influence of R-branch of the SPS 2–5 transition becomes negligible. At about 500 Td intensities of both bands become equal.

Using these definitions, the ratio of emission intensities, relation (3.13), can be experimentally determined from:

$$R_{\lambda 1/\lambda 2}(E/N\,, N) = \frac{a_{\lambda 1}(E/N\,, N)}{a_{\lambda 2}(E/N\,, N)} \cdot C_{\lambda 1,\lambda 2} \ . \qquad (5.18)$$

Here $C_{\lambda 1,\lambda 2}$ takes into account the difference in sensitivity of our entire optical system at different wavelengths. The relative spectral sensitivity was determined using a tungsten lamp and a deuterium lamp whose spectral characteristics were known. We did not take into account negligible changes in the sensitivity between the FNS 0–0 and SPS 2–5 bands, consequently $C_{391,394} = 1$, while $C_{391,337} = 1.84$. For the specific conditions shown in previous figures we obtain: $R_{391/337}$(165 Td, $5.70 \cdot 10^{24}$ m^{-3}) = (231/162722)·1.84 ≈ 0.0026; $R_{391/394}$(165 Td, $5.70 \cdot 10^{24}$ m^{-3}) = (231/4716)·1 ≈ 0.049; and $R_{391/394}$(395 Td, $5.67 \cdot 10^{24}$ m^{-3}) = (1619/2630)·1 ≈ 0.62.

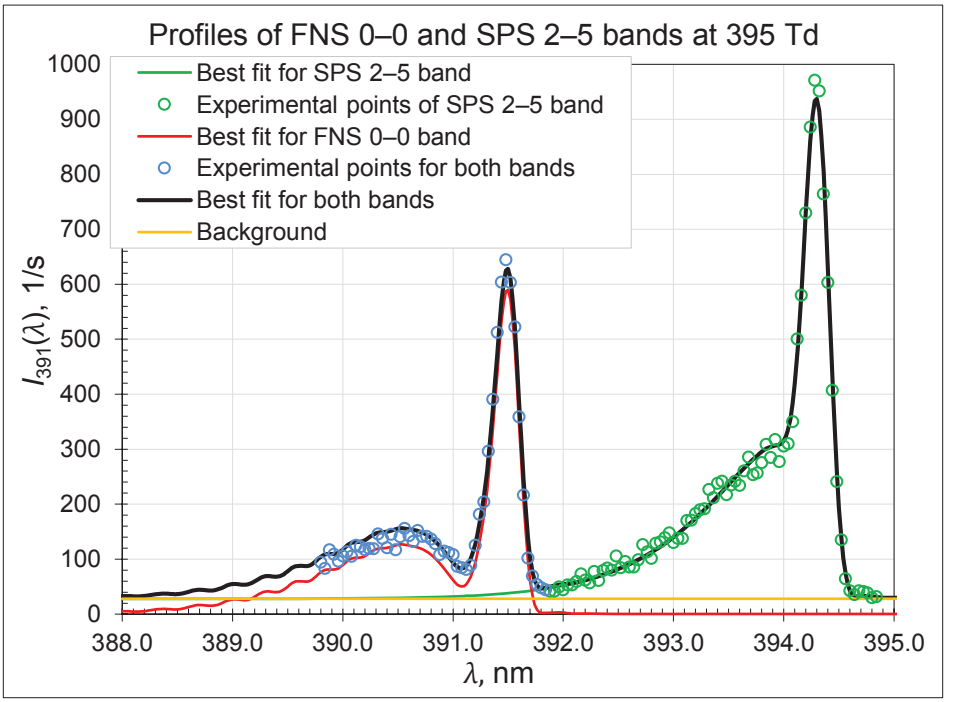

Figure 5.9. Scanned spectrum and calculated best fit for SPS 2–5 and FNS 0–0 bands in dry air at: E/N = (395 ± 20) Td; d = 0.35 mm; p = 176 Torr; i = 1.33 μA; U_d = 767 V; $N = 5.67 \cdot 10^{24}$ m^{-3}; $E_\rho/E < 0.01\%$; T = 300 K; $T_{in} \approx 0.3$ K; $W_{mean} \approx 8.1$ eV. The underlying rotational structure is calculated for T = 300 K for SPS 2–5 transition, and for T_i = 400 K for FNS 0–0 transition. Calculated best fit for SPS 2–5 band, green line, is: $2630 \cdot \Phi_{394}(\lambda) + 28$. Therefore: $b = b_{394} = 28$. Calculated best fit for FNS 0–0 band, red line, is: $1619 \cdot \Phi_{391}(\lambda)$. Best fit for both bands, black line, is: $2630 \cdot \Phi_{394}(\lambda) + 1619 \cdot \Phi_{391}(\lambda) + 28$. Consequently: $R_{391/394} = 1619/2630 \approx 0.62$. At 395 Td EEDF easily covers threshold energies – 11.0 eV and 18.7 eV – of both bands.

The variation of the discharge current during scanning was taken into account by scaling the recorded radiation intensity by corresponding variation in the discharge current, which typically remained between 1–10%. It was particularly important for comparing FNS 0–0 and SPS 0–0 bands, since it took about a minute to move monochromator MDR-23 from 337 nm to 391 nm. Using the model presented in section 2.3.1 for binary collisions, intensities measured at different pressures and temperatures can be reduced to standard conditions, as if measured at N_0, by multiplying all the experimental points by the quotient (5.15):

$$R_{\lambda 1/\lambda 2}(E/N, N_0) = R_{\lambda 1,\lambda 2}(E/N, N) \cdot G_{\lambda 1,\lambda 2}(N, N_0) . \qquad (5.19)$$

6. EXPERIMENTAL RESULTS AND DISCUSSION

6.1. Distribution of charges in the discharge gap

To verify the applicability of models presented in sections 5.1–5.3 to our experimental set-up and to exclude the possibility of filamentation or other spurious effects, we investigated the discharge photographically. Pictures of stationary discharge under selected conditions are presented in figures 6.1 and 6.2. Next, we calculate charged particle number densities between the electrodes from set (5.1) at exactly the same conditions as the presented pictures were taken. Solutions to set (5.1) are presented in figure 6.3.

To overcome technical problems related to low emission intensity, a CCD camera with high sensitivity and 16-bit dynamical range (Apogee Alta, 2048×122 pixels) was used. To eliminate chromatic aberration and disinclined radiation an interference filter, with maximum transmission at 337 nm, in front of the camera was used. The registered section was about 1 mm out of total discharge diameter of 18 mm. Since electrodes are round, the registered intensity cannot be entirely constant in vertical direction. This effect is removed from the presented pictures by applying a transform which takes into account the curvature of electrodes. One can see that the intensity in vertical direction is relatively uniform. This supports the presumption that the emission of electrons and the reduced electric field strength, E/N, are both uniform in the illuminated part of the cathode.

Pictures presented in figure 6.1 can be transformed to 2D plots, presented in figure 6.2, by summing up all the counts in vertical direction. One can see that the increase in intensity is almost linear in a semi-log graph, as predicted by relation (2.38). Due to limited field of depth, the emission intensity near the anode does not drop to zero in the image plane as sharply as in the object plane. The field of depth could not be reduced further since the exposure time was already around 4 minutes.

The rate of growth of electron avalanche and the rate of growth of photon emission as a function of distance can now be compared. To find the rate of growth of photon emission as a function of distance from these figures, we first need to find the correspondence between the image plane, CCD matrix, and the object plane, discharge gap. From figure 6.2 we can see that, although we know the distance between the electrodes, we cannot easily determine the position of electrodes from these pictures. For determining the pixel size in object plane, we took pictures of the discharge gap at different inter-electrode distances without the discharge by illuminating electrodes from behind. In that way the size of the pixel in the object plane could be determined very accurately.

Slopes for $\ln(I_{337}(x))$ curves are presented for each case in figure 6.2. The middle case, $d = 2.80$ mm, is presented in same scale as others to point out that it was the anode that actually moved. From figure 6.2 we can see that the increase in intensity produces a straight line in semi-log plot everywhere but near the cathode. As first electrons are released by photoelectric effect, they do not immediately possess the EEDF corresponding to the conditions between the electrodes.

Profile registered at: 100% N_2; 0% O_2; 5.60 mm; 8.0 Torr; 2185 nA; (465 ± 50) Td; 28°C.

Profile registered at: 100% N_2; 0% O_2; 2.80 mm; 64 Torr; 2177 nA; (272 ± 7) Td; 28°C.

Profile registered at: 60% N_2; 40% O_2; 5.60 mm; 16 Torr; 2081 nA; (328 ± 8) Td; 30°C.

Figure 6.1. Pictures of the non-self-sustaining discharge at 337 nm, corresponding to process (3.9). Vertical range in these pictures in the object plane is about 1 mm. Blue tint was added to these pictures because N_2 spectrum appears bluish for human eye. Although typical exposure times were around 4 minutes, the discharge still remained essentially dark for the naked eye. Only when the discharge current was raised several times, was there a faint blue layer visible near the anode.

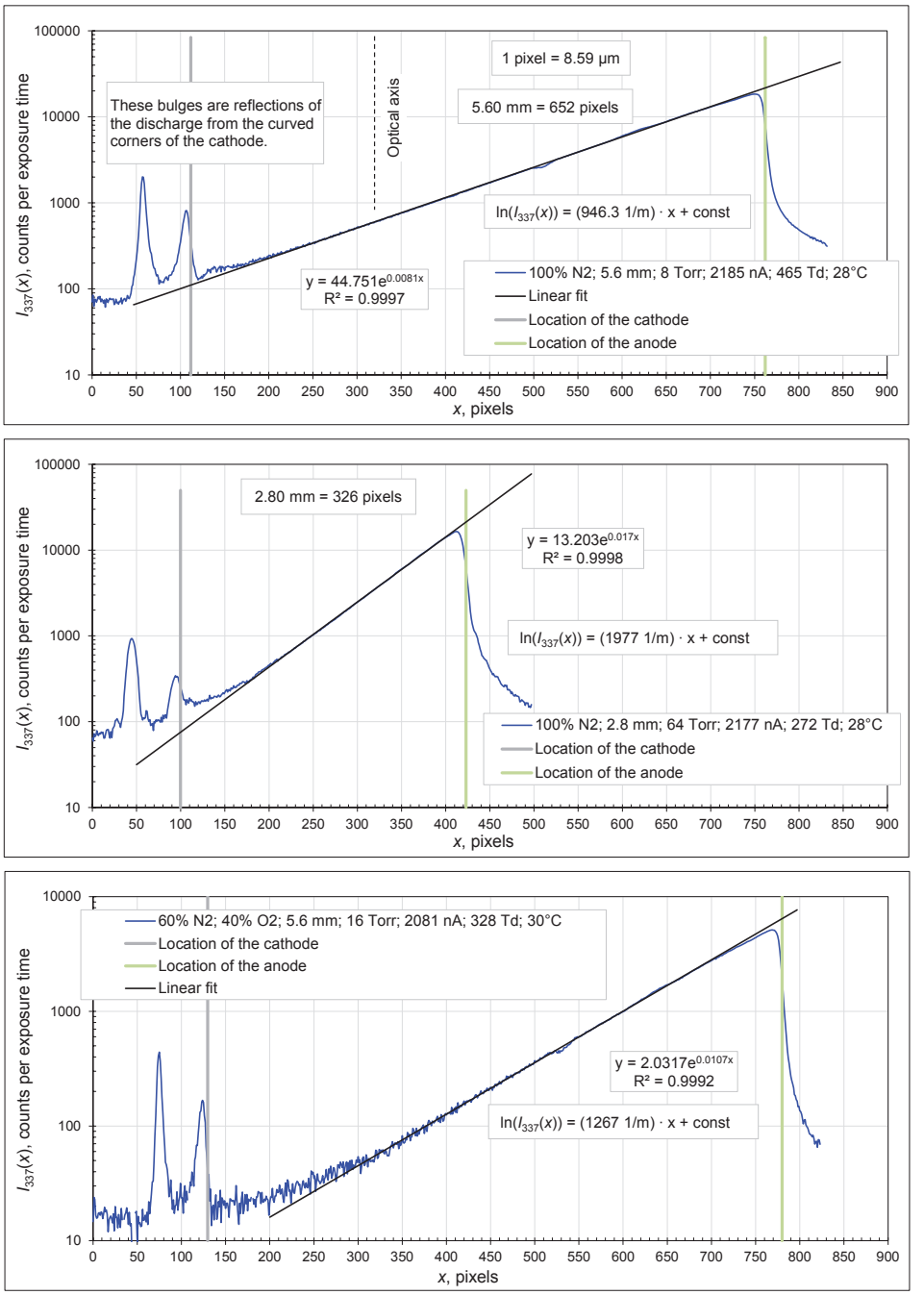

Figure 6.2. Typical emission profiles of the discharge. These figures are obtained from those presented in 6.1 by summing up all the counts in vertical direction and dividing by 122. To avoid overexposure, the exposure time was selected such that the intensity near the anode remained less than 2^{16}. By adding oxygen the intensity sharply decreased, since the quenching rate constant for the upper state of SPS 0–0 transition is more than ten times greater for O_2 than for N_2. In these figures R denotes correlation coefficient.

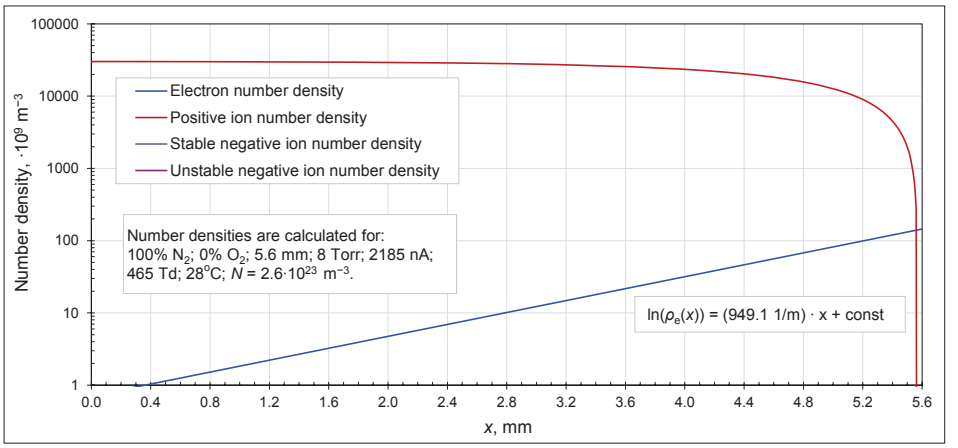

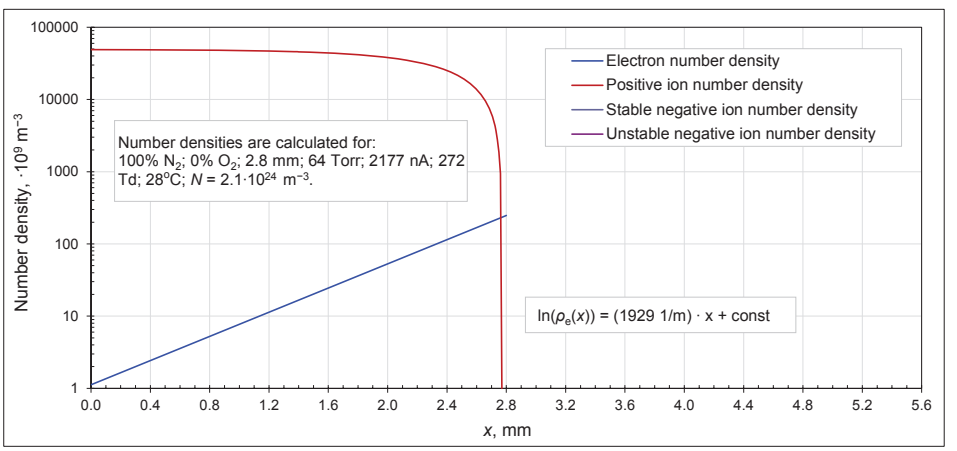

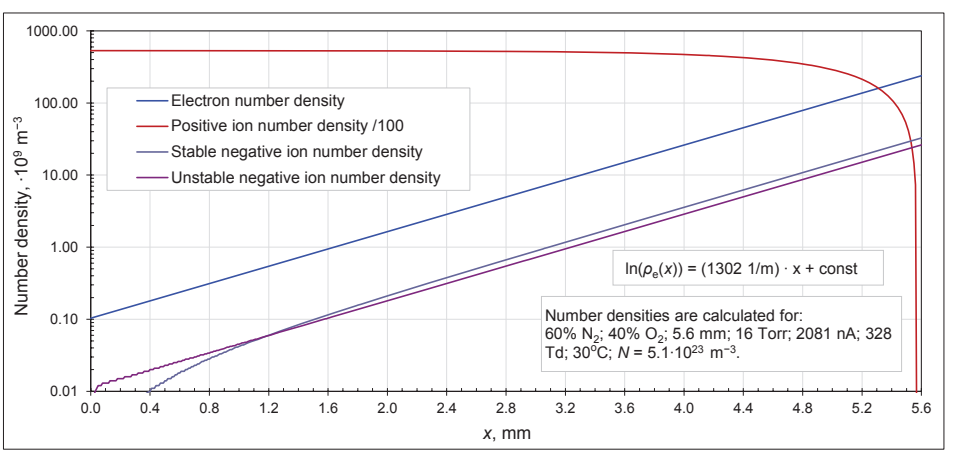

Figure 6.3. Solutions to set (5.1) for conditions at which the pictures presented in figures 6.1–6.2 were taken. If oxygen concentration is zero, then negative ion number density is zero, since the attachment coefficient, η, is zero for pure nitrogen.

This means that these electrons do not yet have enough energy to ionize molecules and just drift, with increasing drift velocity, until EEDF fully develops. Then the drift velocity becomes constant, and the slope of $\ln(\rho_e(x))$ can be characterized by a single coefficient, α. In these pictures, however, the intensity near the cathode is very low, comparable to noise, and this effect cannot be discerned. Yet, for stationary electrons to even reach ionization energy for process (2.12) at conditions presented in the first picture, at least (15.6 V)/$E \approx 0.3$ mm is needed, which corresponds to about 15 pixels.

From the first two equations of set (5.1) we can conclude that electron and positive ion production rates are proportional to electron number density. Consequently, most positive ions and most electrons are created near the anode. Positive ions are pushed towards the cathode and, consequently, positive ion number density increases towards the cathode. When negative ions are absent, the flux of positive ions onto cathode and the flux of electrons onto anode must be equal. From relation (2.33) we can conclude that these fluxes can be equal only if number densities differ about the same amount as mobilities, since the same electric field is applied to both species. Consequently, since the mobility of electrons is much higher than the mobility of ions, $\rho_p(x = 0)$ exceeds $\rho_e(x = d)$ by several orders of magnitude.

By adding oxygen η is no longer zero and negative ions are created. Negative ion number densities are low, since every new electron produces a new positive ion, but only a small fraction of electrons are attached. Remember from section 2.3.2 that most new negative ions are created as unstable negative ions. Consequently, from the third equation in set (5.1), we can conclude that $\rho_{nu}(x)$ is non-zero if $\rho_e(x)$ is non-zero, and unstable negative ions start to form immediately near the cathode. These ions drift towards the anode before they are stabilized and, consequently, $\rho_{ns}(x)$ only starts to increase some distance away from the cathode, as expressed by the last equation in set (5.1).

The results show that, within the limits of uncertainty, the slopes of $\ln(I_{337}(x))$ and $\ln(\rho_e(x))$ coincide at different E/N values, where values of $\ln(\rho_e(x))$ are calculated from set (5.1) using swarm parameters with values obtained from BOLSIG+. Remember that $\alpha/N(E/N)$ is exponentially related to E/N, i.e. small error in E/N would result in larger error in α. For example, for the first picture, using simple relation (2.23) with values presented in table 2.1, we get: α[(465 ± 50) Td] ≈ (896 ± 170) 1/m. Experimentally determined value is 946.3 1/m. Using BOLSIG+, we obtain from set (5.1): (949.1 ± 200) 1/m. This confirms that uncertainty in E/N is well within the limits predicted by figure 4.4.

Pictures of the discharge show that the electric field between the electrodes is homogenous. No filamentation was found. In the case of filamentation, the exponential intensity distribution should be distorted. Although here only three case studies are presented, the same applies to all the pictures taken. The results presented in this section confirm that the processes involved and assumptions made in sections 2.2–2.4, together with models proposed in sections 5.1–5.3, describe satisfactorily non-self-sustaining discharge for the experimental set-up used in this thesis.

6.2. Lifetimes and quenching rate constants

Collisional quenching rate constants for $N_2(C^3\Pi_u, v' = 0)$ and $N_2^+(B^2\Sigma_u^+, v' = 0)$ states by N_2 and O_2 molecules were determined as described in section 5.5. Typical Stern–Volmer dependencies for $N_2(C^3\Pi_u, v' = 0)$ state are shown in figure 6.4. The basis for obtaining such a curve was explained in section 2.3.3. As can be seen from figure 6.4, experimental points, corresponding to different N_2-O_2 mixtures, clearly lie on straight lines. The linear dependence of $1/\tau$ on pressure, p, indicates two-body nature of the quenching reaction in investigated E/N and pressure ranges. The intercept of each regression line corresponds to the reciprocal of natural lifetime, $1/\tau_0$, of the excited state, and the slopes of these lines determine the collisional quenching rate constant, k_q.

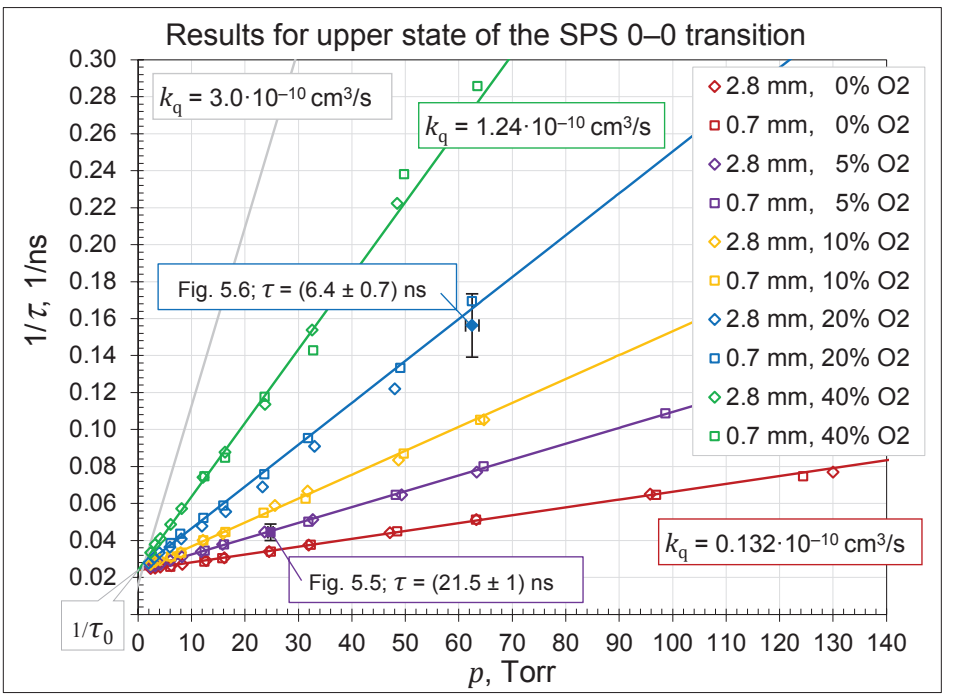

Figure 6.4. Typical Stern–Volmer dependencies for $N_2(C^3\Pi_u, v' = 0)$ state in different N_2-O_2 mixtures. For clarity, only a fraction of the total number of measured experimental points are shown.

For pure nitrogen, represented by the red line, the collisional quenching rate constant could be determined more accurately than for mixtures, because for mixtures the uncertainty in oxygen concentration had to be taken into account. Also, as the quenching rate constant for N_2 molecule was smaller, a wider pressure range could be used for pure nitrogen. Obtained results are presented in table 6.1.

By adding oxygen quenching rate increases. Firstly, remember from section 5.5 that for shorter lifetimes, below 10 ns, we had to separate waveforms using

deconvolution, which implies that the uncertainty is much greater for shorter lifetimes. Secondly, by increasing oxygen concentration, we have fewer radiating molecules and, consequently, emission intensity decreases. Therefore, $\tau_0 = (41.9 \pm 1.7)$ ns is most accurately determined in pure nitrogen, i.e. for the red line, and we can fix the intercept to $1/\tau_0$.

Table 6.1. Lifetimes and quenching rate constants for nitrogen states examined in this thesis. Values used for reduction in Paris *et al* 2005, last row, are taken from Pancheshnyi *et al* 1998 and Pancheshnyi *et al* 2000. Values for $N_2(C^3\Pi_u, \nu' = 2)$ state are presented in parentheses.

State	$N_2^+(B^2\Sigma_u^+, \nu' = 0)$			$N_2(C^3\Pi_u, \nu' = 0)$		
Quantity	τ_0, ns	$k_{q\,N2}$, $\cdot 10^{-10}$ cm^{3}s^{-1}	$k_{q\,O2}$, $\cdot 10^{-10}$ cm^{3}s^{-1}	τ_0, ns	$k_{q\,N2}$, $\cdot 10^{-10}$ cm^{3}s^{-1}	$k_{q\,O2}$, $\cdot 10^{-10}$ cm^{3}s^{-1}
This study	62 ± 3	3.0 ± 0.4	8 ± 3	41.9 ± 1.7	0.132 ± 0.005	2.9 ± 0.1
Values used in Paris *et al* 2005	62 ± 6	2.1 ± 0.2	5.1 ± 0.5	42 ± 2 (39 ± 4)	0.13 ± 0.02 (0.46 ± 0.06)	3 ± 0.3 (3.7 ± 0.5)

Unlike quenching rate constants for N_2, quenching rate constants for O_2 cannot be directly measured. We can carry out experiments in pure N_2, but not in pure O_2. To differentiate between quenching by N_2 and O_2 molecules, linear equation (5.14) has to be solved. To obtain the necessary data for solving equation (5.14), the total quenching rate, k_q, in different N_2-O_2 mixtures was measured. One can see from figure 6.4 that by increasing oxygen concentration the lifetime decreases rapidly. The increase in uncertainty can be seen as increasing dispersion of experimental around given regression lines. Intercept, $1/\tau_0$, remains invariable, even if not fixed, which gives evidence of the correctness of our measurements. We did not measure lifetimes below 3.3 ns (1/3.3 = 0.3), since the lifetime would be too short for successfully deconvolving these waveforms. Quotient for the slope of the green line can be found from relation (5.14) as: $0.4 \cdot 2.9 + 0.6 \cdot 0.132 = 1.24$. Points measured at the same pressure, but different distances between electrodes, correspond to E/N values differing about 2–3 times. Points obtained at different E/N values lie on the same line, indicating that there is no evident dependence on the electric field strength.

We were unable to measure quenching rate constants for $N_2(C^3\Pi_u, \nu' = 2)$ state ourselves. The reason was that the signal was too weak for obtaining waveforms from which the lifetime could be accurately determined. Values shown in table 6.1 are taken from Pancheshnyi *et al* 2000.

Results for $N_2^+(B^2\Sigma_u^+, \nu' = 0)$ state are obtained similarly and are presented in table 6.1. Since the quenching rate constants are greater, the corresponding life-

times are much shorter and, consequently, have greater uncertainty. For comparison, the grey line in figure 6.4 represents quenching of $N_2^+(B^2\Sigma_u^+, v'=0)$ state in pure nitrogen. Consequently, the pressure range for which measurements could be carried out is more limited for $N_2^+(B^2\Sigma_u^+, v'=0)$ state. This results in greater uncertainties for intercepts and slopes of the Stern–Volmer lines composed for $N_2^+(B^2\Sigma_u^+, v'=0)$ state.

Unlike the quenching rate constant for neutral nitrogen states, the quenching rate constant for nitrogen ion state may be expected to depend on E/N. An expectation for such effect originates from the dependence of quenching rate on temperature, reported by Belikov *et al* 1995. At higher temperature the kinetic energy of colliding particles, gas molecules and ions, is higher. Kinetic energy of ions also becomes higher at higher electric fields. Thus, we can expect the dependence of quenching rate of nitrogen ion on E/N. The effect of electric field on ion-neutral collisions is also present in the nitrogen ion conversion reaction (2.32), as can be seen from table 1 in Paris *et al* 2006. If the conversion reaction participates in some way in the quenching, the dependence of quenching rate of $N_2^+(B^2\Sigma_u^+, v'=0)$ state on E/N should appear. Our experiments, however, revealed no dependence on E/N.

In the present work the lifetime of $N_2^+(B^2\Sigma_u^+, v'=0)$ state was experimentally determined in pressure ranges of 0.5–32 Torr (66–4000 Pa). The results show that, similarly to $N_2(C^3\Pi_u, v'=0)$ state, in these pressure ranges $1/\tau$ is linearly related to N and not to N^2. This means that at given pressure ranges three-body collisions have a very small or zero rate constant. Therefore, for both states the quenching rate was found to be dependent on N, but independent of E/N. These results, however, do not exclude the possible influence of three-body processes. At higher pressures N^2 increases more rapidly than N, and three-body processes may become important.

The results obtained by the author of this work coincide well with the results obtained by Pancheshnyi, who used a nanosecond pulse repetitive high-voltage discharge for excitation, but differ considerably from results obtained by Dilecce (Dilecce *et al* 2010) for $N_2^+(B^2\Sigma_u^+, v'=0)$ state. The large difference in results, obtained by different authors for $N_2^+(B^2\Sigma_u^+, v'=0)$ state, is probably caused by difference in experimental conditions and measurement methods. Dilecce has highlighted that the quenching rate constants available in the literature have a clear dependence on the excitation method. The selective excitation methods (LIF) result in consistently higher quenching rate constants, while methods based on the pulsed discharge give smallest, up to 3 times lower, values for these constants.

A more extensive comparison of the results obtained by different authors is presented in Valk *et al* 2010 (IV).

6.3. Intensity ratios of investigated transitions

A comprehensive overview of the results is given in Paris *et al* 2004, 2005, and 2006 (I–III). Here only clear and concise summary is presented.

Intensity ratios of the investigated transitions were calculated as described in section 5.6. In figure 6.5, intensity ratios calculated from relation (5.18) at different pressures are presented. Experimental points for which the calculation of intensity ratios was explicitly shown in figures 5.7–5.9 are also shown as red points. Only results for $R_{391/337}(E/N, N)$ and $R_{391/394}(E/N, N)$ are presented; $R_{394/337}(E/N, N)$ can be found form Paris *et al* 2005, figure 8. Unlike quenching rates and lifetimes, presented in the previous section, intensity ratios we only measured in dried air (for steady mode, Paris *et al* 2005) and in ambient air (for pulsed mode, Paris *et al* 2004).

From figure 6.5 we can see that by lowering pressure, at constant E/N, both ratios increase. This is, in our opinion, caused by the difference in natural lifetimes and collisional quenching constants for these states. For simplicity, let's only consider quenching by N_2 molecules, since air consists mostly of N_2. Remember from table 6.1 that the quenching rate constant for $N_2^+(B^2\Sigma_u^+, v' = 0)$ state is roughly ten times greater than for $N_2(C^3\Pi_u, v' = 0, 2)$ states. Therefore, by deduction, we can conclude that as pressure decreases, more and more ion states can radiate, relative to neutral states, resulting in an increase in the ratio of emission intensities. To see if this assumption is indeed true, we can use formula (5.19), instead of (5.18), to reduce all experimental points, obtained at different pressures, p, and temperatures, T, to the same conditions. In figure 6.6 experimental points reduced to N_0 (STP) are presented. Here all 280 experimental points, including the points presented in figure 6.5, are presented (Paris *et al* 2005, steady mode). One can see that after reduction points obtained at different pressures clearly lie on a single curve. Experimental points which are already closer to STP, measured at higher pressures, shift less than points measured at lower pressures.

A rapid increase with increasing E/N is a common tendency for both intensity ratios. The shape these curves is similar, but the values for $R_{391/394}$ lie about 17 times higher. Similarity between the shapes is expected, because the general shape of excitation functions for upper states of the SPS 0–0 and 2–5 transitions is similar, and the difference between threshold energies for excitation of these states is small (Fons *et al* 1996). From the similarity of the shapes it follows that the ratio $R_{394/337}(E/N, N_0)$ should be, more or less, constant.

From Appendix A we can deduce that with increasing E/N the radiation intensity from SPS 0–0 transition starts to diminish as the EEDF shifts towards higher energies. At the same time as emission cross-section for SPS 0–0 transition decreases, the emission cross-section for FNS 0–0 increases with increasing E/N. Consequently, $R_{391/337}(E/N, N_0)$ and $R_{391/394}(E/N, N_0)$ should be very sensitive to the mean electron energy. Change in E/N for about two orders of magnitude, 100–10000 Td, results in a change in intensity ratios for about three orders of magnitude.

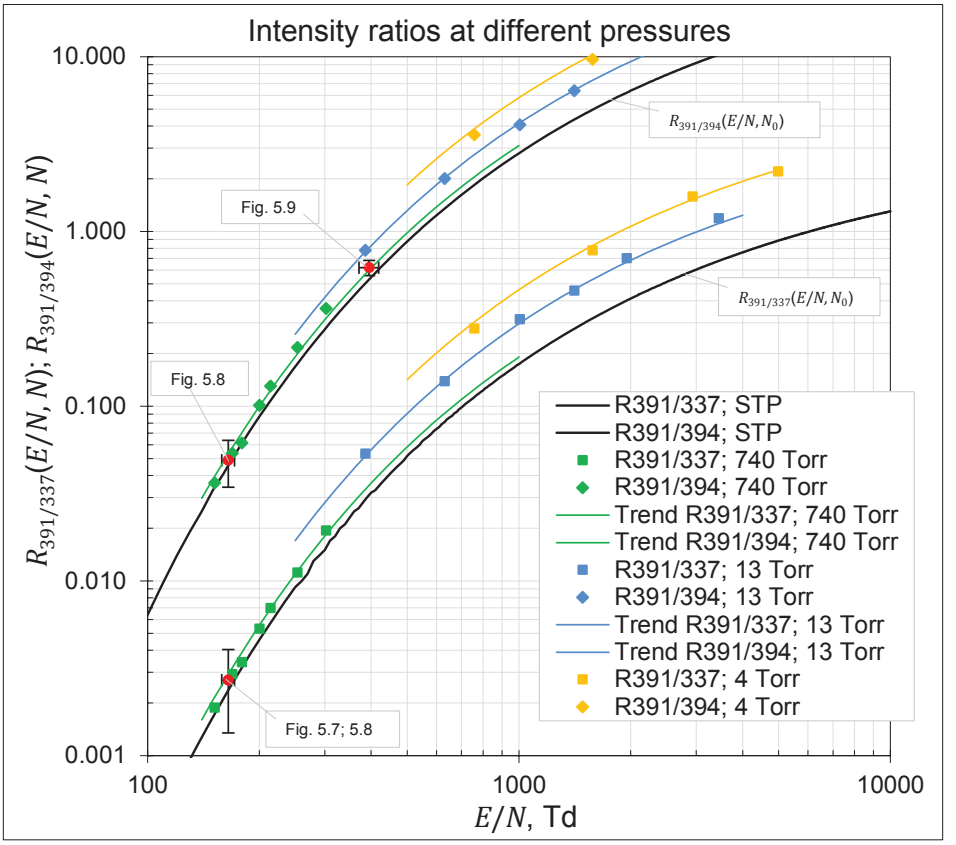

Figure 6.5. Experimentally determined intensity ratios, calculated from relation (5.18). For clarity, only a small fraction of the total number of measured experimental points are shown in a logarithmic scale. These points are obtained in steady mode (Paris *et al* 2005). One can see that ratios measured at different pressures lie on different curves, while the distance between these curves is independent of E/N.

Following empirical formulae (Paris *et al* 2005) can be used for relationships between the intensity ratios and E/N at STP:

$$R_{394/337}(E/N, N_0) = 0.065 \cdot \exp\left(\frac{-402}{(E/N)^{1.5}}\right), \tag{6.1}$$

$$R_{391/394}(E/N, N_0) = 46.5 \cdot \exp\left(\frac{-89}{\sqrt{E/N}}\right), \tag{6.2}$$

$$\begin{aligned} R_{391/337}(E/N, N_0) &= \\ &= R_{394/337}(E/N, N_0) \cdot R_{391/394}(E/N, N_0) \approx \\ &\approx 3.3 \cdot \exp\left(\frac{-92}{\sqrt{E/N}}\right). \end{aligned} \tag{6.3}$$

In these formulae E/N is a dimensionless quantity that numerically equals the reduced field strength expressed in Td. Trendlines, black lines, presented in figures 6.5 and 6.6 are calculated using these formulae. Trendlines for different pressures are obtained by also taking into account formula (5.15).

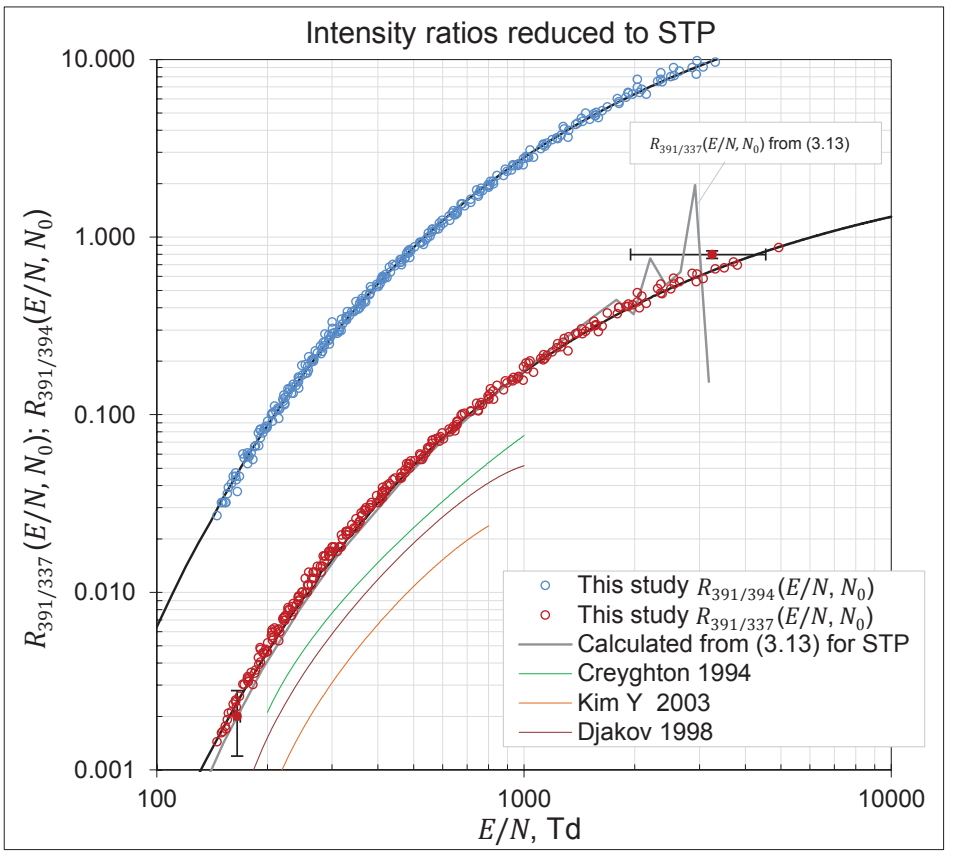

Figure 6.6. Intensity ratios calculated from relation (5.19). Intensity ratios are reduced to standard conditions using formula (5.15). Values of quenching rate constants and lifetimes used in formula (5.15) are presented in the last row of table 6.1.

From figure 6.6 one can notice that the scattering of experimental points around the trendline is smaller for $R_{391/394}$ than for $R_{391/337}$. This can be accounted for by two reasons. Firstly, the background was considered to be the same for FNS 0–0 and SPS 2–5 bands, and was calculated from whichever of the two transitions had higher intensity. Secondly, it took time to move monochromator from 337 nm to 391 nm. Therefore, it took longer time to scan data for $R_{391/337}$ than for $R_{391/394}$. Experimental conditions had more time to change and, consequently, the scattering is larger for $R_{391/337}$.

Remember from section 4.6 that for smaller gap distances and lower pressures the uncertainty in E/N increases. Therefore, the relative uncertainty in E/N is higher at high E/N values. This increase manifests itself as an increase in

scattering of experimental points above 1000 Td. The uncertainty in R increases at lower E/N values as the radiation intensity from FNS 0–0 band decreases. This means that experimental points for which uncertainty in E/N is small have greater uncertainty in R and vice versa. However, from figure 5.6 we can see that there is no accompanying increase in scattering of experimental points at low E/N values. This is because the uncertainty has more a systematic nature. By changing d or p at high E/N we actually make an error in E/N, but at low R values the uncertainty in R does not show, because all ratios were always found by using the same band profiles. For example, $\Phi_{391}(\lambda)$ could be calculated for different ion temperatures, T_i, producing slightly different ratios at low E/N values. This tends to decrease the actual scattering of experimental points. The combined uncertainty is smallest between 300–1000 Td, because there is sufficient amount of radiation available from both bands to determine the ratio accurately, and the uncertainty in E/N is still under 10%. For $R_{394/337}$ and $R_{391/337}$ the corresponding uncertainty is also greater due to the fact that, in addition to uncertainties in E/N, the difference in sensitivity of our entire optical system at 337 nm and 391 nm had to be taken into account. Considering all these circumstances, the corresponding uncertainties for coefficients in formulae 6.1–6.3 are: (0.065 ± 0.01), (–402 ± 100); (46.5 ± 3), (–89 ± 2); (3.3 ± 0.5), (–92 ± 3).

The main results of this thesis are the intensity ratios expressed by formulae 6.1–6.3. These formulae can be used for field strength estimation in low-temperature plasma studies in air if excitation of molecules from the ground state by electron impact is the dominant process. The most accurately determined ratio is $R_{391/394}(E/N, N_0)$, which should be preferred if the results presented in this thesis are to be used.

The expected ratio of emission intensities can also be evaluated theoretically from relation (3.13). This has been previously done for $R_{391/337}(E/N, N)$ by several different authors (Creyghton 1994, Djakov *et al* 1998, Kim Y-H *et al* 2001). The measured intensity ratio considerably differs from theoretical calculations of these authors. In figure 6.6, relation (3.13) is also evaluated numerically for $R_{391/337}(E/N, N_0)$ by the author of this work. EEDFs were obtained by using two-term numerical Boltzmann equation solver BOLSIG+, and emission cross-sections were taken from Itikawa 2006, as presented in Appendix A. This curve coincides, within the limits of uncertainty, with the experimental results obtained by the author of this work. Notice that between 300–1000 Td, where the experimentally determined ratio has the smallest uncertainty, experimentally determined and calculated ratios coincide rather accurately, which indicates that our measurements and calculations are indeed correct. At E/N values over 1500 Td BOLSIG+ does not converge correctly and computed EEDFs are not reliable, which is probably caused by limited database of cross-sections for higher E/N values.

The discrepancy between the results obtained in this work and theoretical calculations of other authors is, probably, caused by uncertainties in reaction schemes, reaction rates, and due to the limited accuracy of cross-sections. It is

also important to note that software for numerically evaluating EEDF has made a major progress in the last decade and was not available to earlier authors.

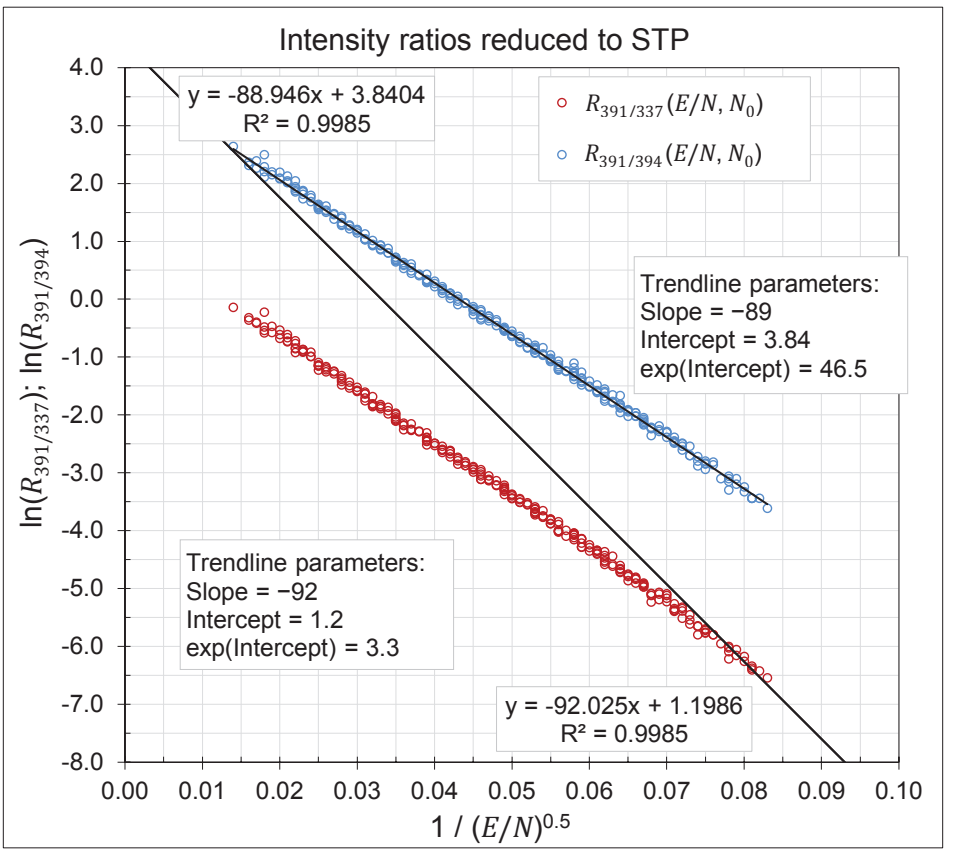

Figure 6.7. Intensity ratios at STP. All experimental points should now be characterized by a straight line. On this figure R denotes correlation coefficient.

6.4. Open problems

The coincidence of our theoretical calculations and measurements is achieved by using the same constants for reduction in relation (3.14). The values used for reduction of intensity ratios in this work are taken from Pancheshnyi *et al* 1998 and Pancheshnyi *et al* 2000, and are presented in the last row of table 6.1. By using different constants for reduction, different ratios are obtained, regardless of whether it is theoretically evaluated or experimentally determined. Note that relation (3.14) is independent of E/N, i.e. this relation does not change the shape of the curve, $R_{\lambda 1/\lambda 2}(E/N, N_0)$, and that the shapes of the curves obtained by different authors are similar.

The deactivation mechanism of $N_2^+(B^2\Sigma_u^+, v' = 0)$ state in air is not clear enough, and the values of rate constants for different processes are not known

sufficiently well for different experimental conditions. Also, other deactivation mechanisms, in addition to quenching via binary collisions, expressed by (3.14), may become important under different experimental conditions. This includes, as pointed out by S Pancheshnyi, the influence of nitrogen ion conversion reaction (2.32) at higher pressures (Pancheshnyi 2006).

The excitation by electron impact is not selective, meaning that higher vibrational levels are also populated. The cascading from those higher levels should be taken into account when determining quenching rates and emission intensities. In Dilecce *et al* 2010 a selective excitation method was used for excitation of the $N_2^+(B^2\Sigma_u^+, \nu' = 0)$ state that excluded the influence of cascading. Results showed that the obtained quenching rate constants are higher for both N_2 and O_2 molecules from those obtained in this study. This strongly indicates to the possibility of cascading, since cascading tends to decrease the quenching rate. Note that by increasing the quenching rate for $N_2^+(B^2\Sigma_u^+, \nu' = 0)$ state, ratios presented in figure 6.6 shift downward. Clarifying of the role of cascading needs further investigation and possibly further experimentation.

APPENDIX A

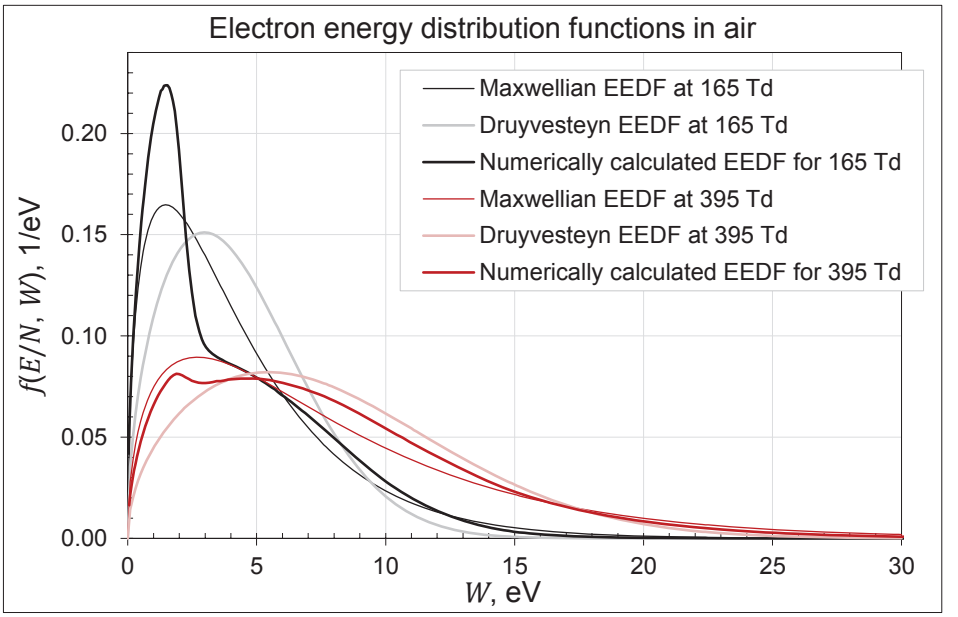

EEDFs in air for two different mean electron energies, W_{mean} = 4.5 eV, E/N = 165 Td, and W_{mean} = 8.1 eV, E/N = 395 Td. Numerically calculated EEDFs are obtained by using two-term numerical Boltzmann equation solver BOLSIG+.

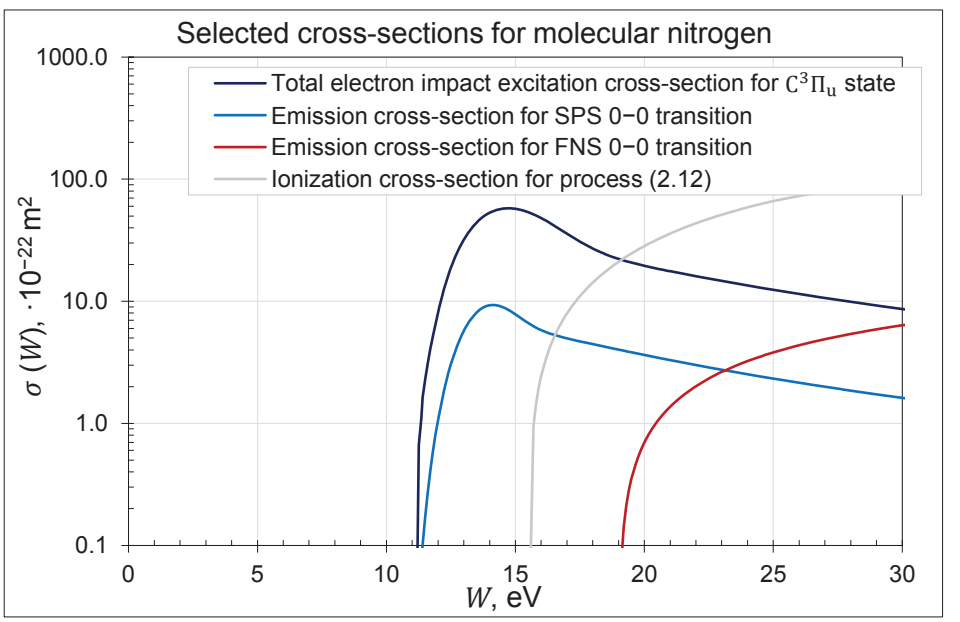

Selected cross-sections for electron collisions with N_2 (Itikawa 2006). The total electron impact excitation cross-section for $N_2C^3\Pi_u$ state follows the same general form as emission cross-section for SPS 0–0 transition, but only part of $N_2C^3\Pi_u$ states decays through SPS 0–0 transition.

APPENDIX B

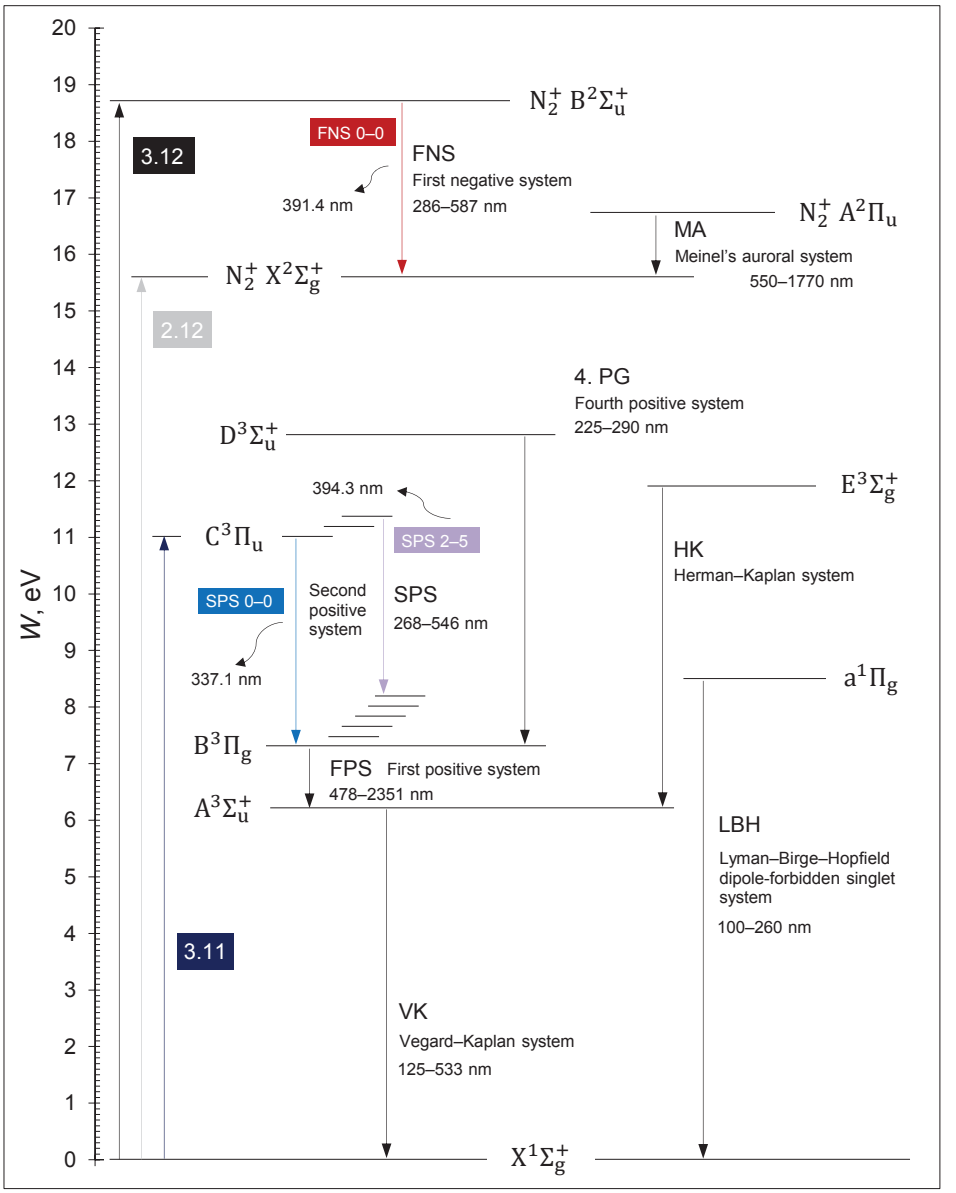

Selected electronic transitions for N_2 and N_2^+ molecules in a simplified potential energy diagram (Šimek 2014). Radiative transitions investigated in this work are shown in colour.

APPENDIX C

Detailed sketch of the discharge chamber.

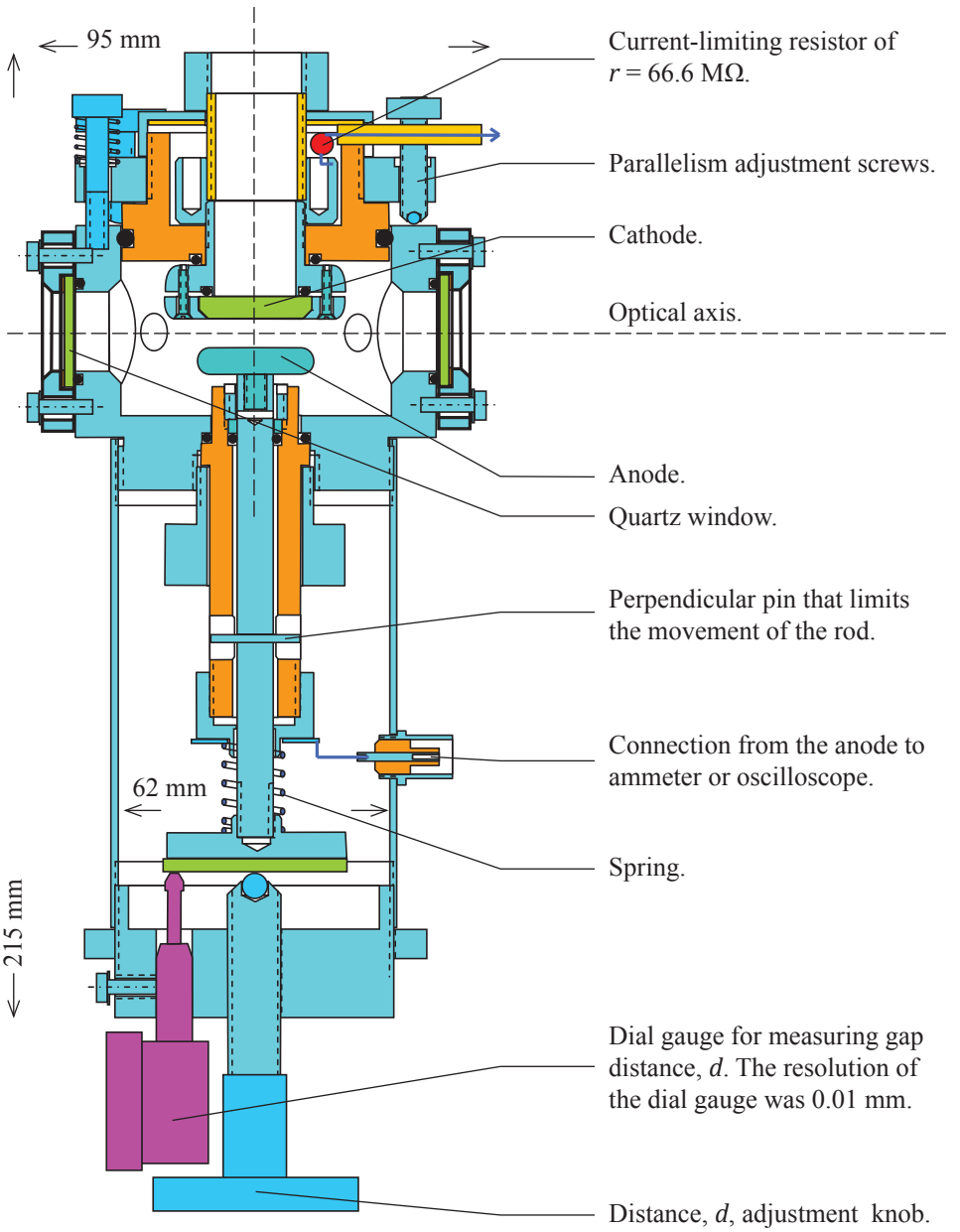

APPENDIX D

Selected pictures of the discharge chamber.

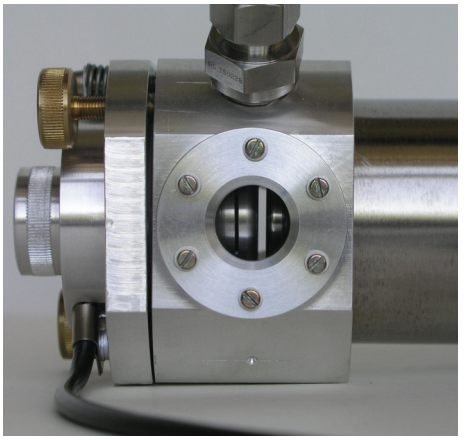

Side view of the discharge chamber. The black lead is high-voltage input. Looking through the quartz window, cathode, on the left, and anode, on the right, can be seen. In this case the chamber is equipped with a steel anode.

After replacing the cathode, the interior of the discharge chamber is cleaned to remove all previous cathode remnants. Then the chamber is pumped down to 0.01 Torr, leaving a small flow of pure gas flowing through the system.

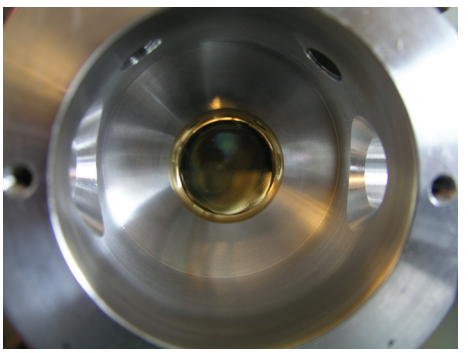

Inside view of the discharge chamber.

The chamber is equipped with a brass anode. The greenish spot on the anode appears after weeks of experimenting due to cathode sputtering.

Although the discharge is almost homogenous at larger gap distances, at smaller distances the cathode still does not wear off uniformly, producing this visible spot on the anode.

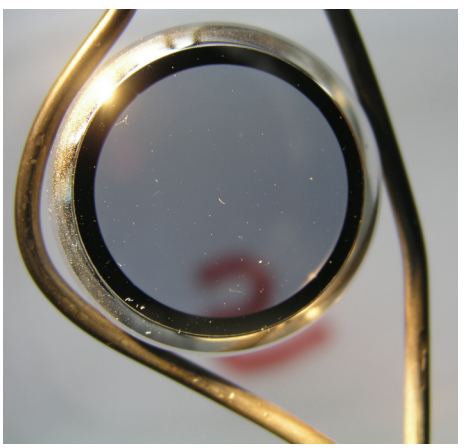

Close-up view of the cathode – a thin semi-transparent aluminium coating evaporated on a quartz plate.

Aluminium is evaporated in two steps. First, a thin film of about 200 nm is laid with transparency of 10–40% at visible ranges. Secondly, a thicker layer of several μm is deposited at the edges to ensure good electrical connection to the socket in which the cathode lies. For some experiments gold was used as cathode material; however, in our case there seemed to be no advantages over using aluminium.

SUMMARY

Optical emission spectrum of molecular nitrogen is an important tool for investigating electric discharge phenomena in ambient atmosphere and it is also often used for diagnostics of low-temperature gas discharge plasmas.

In particular, the intensity ratio of spectral bands with bandhead wavelengths at 391.4 nm and 337.1 nm (or 394.3 nm), corresponding to $N_2^+ B^2\Sigma_u^+ \rightarrow X^2\Sigma_g^+$ (FNS) 0–0 and $N_2\ C^3\Pi_u \rightarrow B^3\Pi_g$ (SPS) 0–0 (or 2–5) transitions, throughout this work denoted as $R_{391/337}$ (or $R_{391/394}$), is often used for electric field strength determination in nitrogen-containing gas discharges. Since the excitation energies of these bands differ considerably – 18.7 eV and 11.0 eV –, the ratio of emission intensities is sensitive to comparatively small changes in the mean electron energy.

Despite a rather wide use of the above-mentioned intensity ratio for measuring or estimating electric field strength in gas discharge plasmas, the relation between the intensity ratio, $R_{391/337}$, electric field strength, E, and gas number density, N, was estimated by earlier authors only theoretically. Moreover, theoretical intensity ratios of different authors differ considerably. According to our knowledge, no experimental verification of these theoretical curves had yet been made.

The aim of the present work was to experimentally determine the relationship between radiation intensity and electric field strength in air discharges for the above-mentioned transitions, and clear up physical processes that are significant for development of this relationship.

For this purpose low current, ~ 2 μA, non-self-sustaining discharge with homogeneous electric field between parallel-plate electrodes was generated. The discharge was initiated by illuminating the cathode with continuous ultraviolet radiation (UV) or short, few ns, UV pulses. Changing both, the distance between electrodes, d, and the gap voltage, U_d, the reduced field strength, E/N, (the ratio of electric field strength and gas number density) was varied in the range of $(150–4000)\cdot10^{-21}$ V·m^2 (150–4000 Td). Ratios $R_{391/337}$ and $R_{391/394}$ were measured in the pressure range of 300 to 10^5 Pa (~ 2–760 Torr).

Main results of this thesis are:

- The dependence of $R_{391/337}$ and $R_{391/394}$ on the reduced field strength, E/N, in air is determined experimentally for the first time in a wide range of E/N values. The experimental set-up is straightforward, ensuring excitation of gas molecules under controlled conditions in an undistorted homogeneous field.
- Measurements showed that at pressures above 10 kPa (~ 100 Torr) ratios $R_{391/337}(E/N, N)$ and $R_{391/394}(E/N, N)$ are independent of pressure and are only functions of E/N. At lower pressures the dependence on pressure becomes evident. This is probably caused by different radiative lifetimes

and collisional deactivation coefficients of the upper states of the examined transitions.

- Based on this assumption, a reduction procedure for $R_{391/337}(E/N, N)$ and $R_{391/394}(E/N, N)$ to the standard conditions (STP), N_0, was proposed. As a result, functions of only one variable, E/N, for $R_{391/337}(E/N, N_0)$ and $R_{391/394}(E/N, N_0)$ at N_0 were obtained.
- $R_{391/337}(E/N, N_0)$ was shown, within the limits of uncertainty, to be the same for pulsed and steady state conditions.
- Empirical formulae of only one dependent variable, reduced field strength, E/N, for these relations at STP were deduced.
- These formulae can be used for estimating E/N in low-temperature plasma studies in air if the excitation of molecules from the ground state by electron impact is the dominant process.
- A new method for quenching rate measurements is implemented. The characteristic and novel detail of the method is that the gas is excited by pulses of non-self-sustaining discharge, while electrons are removed by the steady field from the excited gas. Thus, the participation of electrons in collisional processes during the de-excitation period is excluded.
- For the first time the dependence of collisional quenching rate of $N_2^+(B^2\Sigma_u^+, v' = 0)$ state by N_2 and O_2 molecules on the electric field strength was investigated in the range of up to 4000 Td. The collisional quenching rate was found to be independent of the reduced electric field strength, E/N.
- The linear dependence of reciprocal of lifetime on pressure, p, indicates two-body nature of the quenching reaction of the upper states of the investigated transitions in investigated E/N and pressure ranges of 70–4300 Pa (~ 0.5–32 Torr).

Open problems:

- The excitation-deactivation mechanism of $N_2^+(B^2\Sigma_u^+, v' = 0)$ state in air is not clear enough, and the values of rate constants for collisional de-activation and conversion reactions for ions are not known sufficiently well for different experimental conditions.
- The excitation by electron impact is not selective, meaning that higher vibrational levels are also populated by the discharge pulse. Cascading from higher levels, in principle, can influence the lifetime measurements. Clarifying the role of cascading needs further investigation and, possibly, further experimentation.

SUMMARY IN ESTONIAN

Elektrivälja tugevuse määramine gaaslahendusplasmas lämmastiku kiirgusspektri kaudu

Gaaslahenduses toimuvate protsesside uurimisel on sageli teadmata tegelik elektrivälja tugevus mingis kindlas lahenduse piirkonnas. Põhjuseks on tavaliselt gaaslahenduses osalevate laengukandjate poolt tekitatud ruumlaengu oluline mõju või ka väljatugevuse kiire muutumine. Osutub, et tegelikku elektrivälja tugevust saab määrata ka optiliselt – kasutades vastavast lahenduse piirkonnast mõõdetud kiirgusspektri intensiivsuse jaotust. Optiline diagnostikameetod põhineb asjaolul, et molekule ergastavate elektronide energia sõltub otseselt elektrivälja tugevusest antud piirkonnas. Kui uuritavate spektrijoonte ergastusenergiad üksteisest palju erinevad, siis ongi spektrijoonte intensiivsuste suhe sõltuvuses elektrivälja tugevusest. Optilise diagnostikameetodi suur eelis on, et see ei mõjuta elektrivälja lahenduses.

Lämmastiku puhul on diagnostikaks sobivaimad palju uuritud suure intensiivsusega lämmastiku spektri teise positiivse süsteemi, $N_2C^3\Pi_u \rightarrow B^3\Pi_g$, 0−0 ja 2−5 üleminekud lainepikkustega 337,1 nm ning 394,3 nm ja lämmastiku molekulaarse iooni esimese negatiivse süsteemi, $N_2^+B^2\Sigma_u^+ \rightarrow X^2\Sigma_g^+$, 0–0 üleminek lainepikkustel 391,4 nm. Täpse sõltuvuse teoreetiline määramine pole aga kerge ülesanne, sest see oleneb elektronide energia jaotusfunktsioonist, kasutatavate nivoode ergastus-ristlõigetest ja veel teistest teguritest, mille täpne väärtus pole alati teada. Senised erinevate autorite tehtud intensiivsuse suhte teoreetilised arvutused on andnud üksteisest oluliselt lahknevaid tulemusi.

Käesoleva doktoritöö peamine tööülesanne oli toodud üleminekute intensiivsuste suhete, $R_{391/337}$ ja $R_{391/394}$, eksperimentaalne määramine erinevatel taandatud elektrivälja tugevustel, E/N, ja erinevatel rõhkudel õhus. Selleks tekitati nõrga vooluga mitteiseseisev lahendus tasaparalleelsete elektroodide vahel, kus elektriväli on homogeenne ja väljatugevust saab muuta laiades piirides muutes elektroodide vahekaugust, d, ja gaasi tihedust, N. Lisaks mõõdeti ka uuritavate üleminekute ergastatud seisundite eluead ja põrkelised kustutustegurid N_2 ja O_2 molekulide jaoks. Kirjeldatud mõõtmisi raskendas lämmastiku molekulaarse iooni kiirguse väike intensiivsus madalamatel väljatugevustel ja lahendusvahemiku läbilöögi tekkimine suurematel väljatugevustel.

Käesolevas töös leitud intensiivsuste suhteid saab kasutada elektrivälja tugevuse hindamiseks erinevatel rõhkudel gaaslahendusplasmas ainult N_2^+ ja N_2 kiirgusspektrite alusel. Saadud tulemusi saab kasutada ka teiste autorite teoreetiliste arvutuste õigsuse kontrolliks.

Doktoritöö põhitulemused on järgmised:

- Otsitavad intensiivsuste suhted määrati esmakordselt eksperimentaalselt õhus laias taandatud elektrivälja tugevuse (150–4000 $\cdot 10^{-21}$ V·m^2; 150–4000 Td) ja rõhu (0,3–100 kPa; ~ 2–760 Torr) vahemikus. Nii katse-

seadme kui ka kogu eksperimendi loogiline ülesehitus võimaldas vältida katsetulemuste mitmeti tõlgendamist: gaasi molekulid ergastati homogeenses elektriväljas tingimustel, mis võimaldas otsitavad suurused üheselt määrata.

- Impulssrežiimis saadud suhete väärtused langesid kokku pidevas režiimis mõõdetud väärtustega.
- Mõõtmised näitasid, et rõhkudel üle 10 kPa (~ 100 torri) on leitud intensiivsuste suhted rõhust, p, sõltumatud ja sõltuvad ainult taandatud elektrivälja tugevusest, E/N. Madalamatel rõhkudel avaldub ka otsitavate suhete sõltuvus gaasi rõhust. Rõhust sõltuvuse põhjusena tuuakse välja uuritavate üleminekute ergastatud seisundite kustutustegurite ja eluigade erinevus.
- Sellest lähtudes tuletati võimalus intensiivsuste suhete taandamiseks gaasi normaaltihedusele, N_0. Taandamise tulemusena saadakse funktsioonid $R_{391/337}(E/N, N_0)$ ja $R_{391/394}(E/N, N_0)$, mis sõltuvad ainult ühest muutujast – taandatud elektrivälja tugevusest, E/N.
- Kõikide uuritavate intensiivsuste suhete kirjeldamiseks leiti empiirilised lähendusfunktsioonid, mis sõltuvad ainult taandatud elektrivälja tugevusest, E/N.
- Leitud lähendusfunktsioone võib kasutada elektrivälja tugevuse määramiseks madaltemperatuurilises lahendusplasmas juhul, kui molekulide ergastamine toimub peamiselt läbi elektronpõrke põhiseisundist.
- Mõõdeti uuritavate üleminekute ülemiste seisundite eluea sõltuvus rõhust ja elektrivälja tugevusest. Leiti, et ergastatud seisundite põrkelise kustutusteguri väärtus ei sõltu elektrivälja tugevusest nii lämmastiku molekuli kui molekulaarse iooni korral.
- Veendumaks, et elektriväli elektroodide vahel on homogeenne, uuriti lahendust seda pildistades. Tulemused näitasid, et elektriväli on kogu lahenduse ulatuses homogeenne.

Käesolevas töös eksperimentaalselt mõõdetud intensiivsuste suhe $R_{391/337}$ ei lange määramatuse piires kokku teiste autorite teoreetiliste arvutustega. Leitud lämmastiku molekulaarse iooni ergastatud seisundi põrkelise kustutusteguri väärtus langeb kokku nende autorite poolt saadud väärtustega, kes on kasutanud ergastamiseks impulsslahendust. Samas autorid, kes on kasutanud ergastamiseks teisi meetodeid, on saanud mitu korda suuremaid kustutusteguri väärtusi. Suuremaid väärtusi on saadud just kasutades selektiivset ergastamist laserikiirgusega. Sellisel juhul langeb ära uuritavate seisundite ergastamine kõrgema energiaga ergastatud molekulide poolt, mis võib aga aset leida käesolevas töös kasutatud ergastusmeetodi korral. Nende küsimuste selgitamiseks on vaja teostada eraldi mõõtmisi teistsuguste seadmetega, kui olid kasutada käesoleva töö autorile.

ACKNOWLEDGEMENTS

While I am the beneficiary of much of the attention and compliments for this arduous work, I would like to thank people without whose significant contribution completing this work would have been an impossible task.

I am grateful to assistant professor Kirill V. Kozlov from Moscow State University and Dr. Hans-Erich Wagner from University of Greifswald whose original idea triggered this study.

I am also grateful to several former undergraduate students whose measurement results are included in several parts of the thesis. It is a pleasure to acknowledge Artur Tamm, who helped me to measure the data required for determining the lifetimes and quenching rates of the investigated states, and Mikk Viidebaum, who assisted me in investigating the discharge photographically.

Many thanks to Lennart Neiman, who produced all these precious cathodes used in this work and kept up a continuous fresh supply.

I would also like to thank Tõnu Asu, who aided me in solving numerous technical challenges that would inevitably arise during such a work.

Special thanks to my supervisors Dr. Märt Aints and Dr. Peeter Paris, whose contribution and will have been a compelling force for me for all these years. Thanks also for reading parts of the thesis and for making valuable suggestions, which is gratefully acknowledged. Any errors and omissions are entirely my own responsibility.

For supporting my research continuously for more than ten years, I would like to thank my family, who have forgiven me my inevitable non-participation in social and family responsibilities, which results from an undertaking such as this. Their patience has been a source of continuous energy during the entire study.

REFERENCES

Anders A 2003 Tracking down the origin of arc plasma Science – II. Early continuous discharges *IEEE Transactions On Plasma Science* **31** 1060–69

Badaloni S and Gallimberti I 1972 Basic data of air discharges *Upee-72/05* (Padova University)

Belikov A E, Kusnetsov O V and Sharafutdinov R G 1995 The rate of collisional quenching of N_2O^+ ($B^2\Sigma$), N_2^+ ($B^2\Sigma$), O_2^+ ($b^4\Sigma$), O^+ (3d), O (3p), Ar^+ (4p´), Ar (4p, 4p´) at the temperature ≤200 K *J. Chem. Phys.* **102** 2792–801

Bellan P M 2006 *Fundamentals of Plasma Physics* (Cambridge University Press)

Bogaerts A, Neyts E, Gijbels R, Mullen J 2002 Gas discharge plasmas and their applications *Spectrochimica Acta Part B:Atomic Spectroscopy* **57** 609–658

BOLSIG+ 2005 http://www.bolsig.laplace.univ-tlse.fr/ Boltzmann equation solver for electrons

Born M and Oppenheimer J. R. 1927 Zur Quantentheorie der Molekeln Annalen der Physik **389** 457–484

Braithwaite N St J 2000 Introduction to gas discharges *Plasma Sources Sci. Technol.* **9** 517–527

Condon E 1926 A Theory of Intensity Distribution in Band Systems *Phys. Rev.* **28** 1182–1201

Creyghton Y L M 1994 Pulsed positive corona discharges *PhD Thesis* Eindhoven University of Technology

Dakin T W, Luxa G, Oppermann G, Vigreux J, Wind G and Winkelnkemper H 1974 Breakdown of gases in uniform fields. Paschen curves for nitrogen, air and sulfur hexafluoride *Electra* **32** 61–82

Dilecce G, Ambrico P F and De Benedictis S 2010 On the collision quenching of $N_2^+(B^2\Sigma_u^+, v=0)$ by N_2 and O_2 and its influence on the measurement of E/N by intensity ratio of nitrogen spectral bands *J. Phys. D: Appl. Phys.* **43** 195201

Dilecce Giorgio 2014 Optical spectroscopy diagnostics of discharges at atmospheric pressure *Plasma Sources Sci. Technol.* **23** 015011

Djakov A F, Bobrov Yu K, Bobrova L N and Yourguelenas Yu V 1998 Streamer discharge plasma parameters determination in air on a base of a measurement of radiation of the molecular bands of nitrogen *Physics and Technology of Electric Power Transmission* (Moscow: MPEI) pp 219–33 (in Russian)

Dutton J 1978 Spark breakdown in uniform fields *Electrical Breakdown of Gases* ed J M Meek and J D Craggs (Chichester: Wiley)

Fitzpatrick R 1998 *Introduction to plasma physics* (The University of Texas at Austin, a graduate level lecture course)

Fons J T, Schappe R S and Lin C C 1996 Electron-impact excitation of the second positive band system ($C^3\Pi_u \rightarrow B^3\Pi_g$) and the $C^3\Pi_u$ electronic state of the nitrogen molecule *Phys. Rev.* A **53** 2239–47

Gallimberti I, Hepworth J K and Klewe R C 1974 Spectroscopic investigation of impulse corona discharges *J. Phys. D: Appl. Phys.* **7** 880–98

Goldston R J Rutherford P H 1995 *Introduction to plasma physics* (Bristol: Institute of Physics Publishing)

Grill A 1994 *Cold Plasma in Materials Fabrication: From Fundamentals to Applications* (Wiley-IEEE Press)

Hartmann G and Johnson P C 1978 Measurements of relative transition probabilities and the variation of the electronic transition moment for N_2 $C^3\Pi_u$ – $B^3\Pi_g$ second positive system *J. Phys. B. Atom. Molec. Phys.* **11** 1597–612

Hartmann G 1977 Spectroscopie de la décharge couronne: étude des méchanismes de collisions dans le dard (streamer) *PhD Thesis* 1783, Université de Paris-Sud, Centre d'Orsay

Hugh M Hulburt and Joseph O Hirschfelder 1941 Potential Energy Functions for Diatomic Molecules *J. Chem. Phys*. **9** 61

Itikawa Y 2006 Cross Sections for Electron Collisions with Nitrogen Molecules *Journal of Physical and Chemical Reference Data* **35** 32–53

Kim Y, Hong S H, Cha M S, Song Y-H and Kim S J 2003 Measurements of electron energy by emission spectroscopy in pulsed corona and dielectric barrier discharges *J. Adv. Oxid. Technol.* **6** 17–22

Kim Y-H, Hong S H, Cha M S, Song Y-H and Kim S J 2001 Measurements of electron energy by emission spectroscopy in pulsed corona and dielectric barrier discharges *Proc. 3rd ISNPT Cheju* (*Korea*)

Kitayama J and Kuzumoto M 1999 Analysis of ozone generation from air in silent discharge *J. Phys. D: Appl. Phys.* **32** 3032

Kozlov K V, Wagner H-E, Brandenburg R, Michel P 2001 Spatio-temporally resolved spectroscopic diagnostics of the barrier discharge in air at atmospheric pressure *J. Phys. D: Appl. Phys.* **34** 3164–3176

Lieberman M A, Lichtenberg A J 1994 *Principles of Plasma Discharges and Materials Processing* (Wiley-Interscience, Hoboken, NJ: John Wiley and Sons)

Lofthus A and Krupenie P H 1977 The spectrum of molecular nitrogen *J. Phys. Chem. Ref. Data* **6** 113–307

Morrow R 1985 Theory of negative corona in oxygen *Phys. Rev.* A **32** 1799–1809

Naghizadeh-Kashani Y, Cressault Y and Gleizes A 2002 Net emission coefficient of air thermal plasmas *J. Phys. D: Appl. Phys*. **35** 2925–2934

Pancheshnyi S 2006 Comments on 'Intensity ratio of spectral bands of nitrogen as a measure of electric field strength in plasmas' *J. Phys. D: Appl. Phys.* **39** 1708–1710

Pancheshnyi S 2013 Effective ionization rate in nitrogen-oxygen mixtures *J. Phys. D: Appl. Phys*. **46** 155201 (8pp)

Pancheshnyi S V, Starikovskaia S M and Starikovskii A Yu 1998 Measurements of rate constants of the N_2 ($C^3\Pi_u$, v'=0) and N_2^+ ($B^2\Sigma^+_u$, v'=0) deactivation by N_2, O_2, H_2, CO and H_2O molecules in afterglow of the nanosecond discharge *Chem. Phys. Lett.* **294** 523–7

Pancheshnyi S V, Starikovskaia S M and Starikovskii A Yu 2000 Collisional deactivation of N_2 ($C^3\Pi_u$, v'=0, 1, 2, 3) states by N_2, O_2, H_2 and H_2O molecules *Chem. Phys.* **262** 349–357

Paris P, Aints M, Laan M and Valk F 2004 Measurement of intensity ratio of nitrogen bands as a function of field strength *J. Phys. D: Appl. Phys.* **37** 1179–84

Paris P, Aints M, Valk F, Plank T, Haljaste A, Kozlov K V and Wagner H-E 2005 Intensity ratio of spectral bands of nitrogen as a measure of electric field strength in plasmas *J. Phys. D: Appl. Phys.* **38** 3894–9

Paris P, Aints M, Valk F, Plank T, Haljaste A, Kozlov K V and Wagner H-E 2006 Reply to comments on 'Intensity ratio of spectral bands of nitrogen as a measure of electric field strength in plasmas' *J. Phys. D: Appl. Phys.* **39** 2636–2639

Paschen F 1889 Uerber die zum Fumkenübergang in Luft Waserstoff und Kohlensäune bei verschiedenen Drucken erforderliche Potentialdifferenz *Ann. Phys*. **273** 69–75

Plank T, Jalakas A, Aints M, Paris P, Valk F, Viidebaum M, Jõgi I 2014 Ozone generation efficiency as a function of electric field strength in air *J. Phys. D: Appl. Phys.* **47** 335205

Raizer Y P 1991 *Gas Discharge Physics* (New York: Springer)

Raju G G 2006 *Gaseous electronics: theory and practice* (CRC/Taylor & Francis)

Ramo S 1939 Currents induced by electron motion *Proc. Inst. Radio Eng.* **27** 584–585

Šimek M 2014 Optical diagnostics of streamer discharges in atmospheric gases *J. Phys. D: Appl. Phys.* **47** 46300

Shockley W 1938 Currents to conductors induced by a moving point charge *J. Appl. Phys.* **9** 635

Valk F, Aints M, Paris P, Plank T, Maksimov J and Tamm A 2010 Measurement of collisional quenching rate of nitrogen states $N_2(C^3\Pi_u, \nu = 0)$ and $N_2^+\left(B^2\Sigma_g^+, \nu = 0\right)$ *J. Phys. D: Appl. Phys.* **43** 385202

Wen C 1989 Time resolved swarm studies in gases with emphasis on electron detachment and ion conversion *PhD Thesis*, Eindhoven, Netherlands

ORIGINAL PUBLICATIONS

CURRICULUM VITAE

Name:	Fred Valk
Date and place of birth:	25.12.1979, Rapla, Estonia
Citizenship:	Estonian
Phone:	+372 56 917827
Contact-address:	University of Tartu, Institute of Physics, Physicum 415D, W. Ostwaldi 1, 50411 Tartu, Estonia
E-mail:	fred.valk@il.ee

Education:

2005–2009	University of Tartu, PhD student.
2003–2005	University of Tartu, MSc in physics.
1999–2000	military service in Estonian Defence Forces.
1998–2003	University of Tartu, BSc in physics.
1995–1998	Rapla Vesiroosi Gymnasium.

Professional employment:

2010–	OÜ Insenerlahendused, CEO.
2005–2015	University of Tartu, Institute of Physics, engineer.
2006–2009	Estonian University of Life Sciences, Institute of Technology, lecturer.

Professional development:

09.2006–	IPP Summer University for Plasma Physics, Max-Planck Institut für Plasmaphysik, September 2006, Garching, Germany.
07.2006–	Calibration measurements at University of Greifswald, July 2006, Greifswald, Germany.
06.2005–	Summer school of experimental plasma physics (SUMTRAIC) 2005, Institute of Plasma Physics, Tokamak Department, June 2005, Prague, Czech Republic.

Teaching experience:

Undergraduate Course in Physics, 6 EAP, TET 3.2411, University of Life Sciences.

Digital Signal Processing, 3 EAP, LOTI.05.026, University of Tartu.

Theses supervised by me:

Diploma and bachelor's theses:

Mihkel Rähn, "The *U–i* characteristics of non-self-sustained gas discharge depending on the properties of photocathode", University of Tartu, 2006.

Artur Tamm, "Spectroscopical determination of the collisional deactivation rate constant of excited nitrogen molecular ion", University of Tartu, 2008.

Mikk Viidebaum, "Determination of the spatial distribution of electrons in plasma through optical radiation", University of Tartu, 2009.

Kaarel Prommik, "Projekt zur Optimierung von Produktionslinien in AS Estiko-Plastar", Estonian University of Life Sciences, Tartu 2010.

Taavi Väljaots, "Autonomous embedded system for LED lighting", Tartu Technology College, 2012.

Karl Tiirik, "A guide to digital signal processor TMS320VC5510 – an introduction with practical tasks", University of Tartu, 2012.

Madis Sepp, "Fully autonomous data-logger developed in Java language", University of Tartu, 2012.

Antti Jaaniste, "Android OS based metering system for inertial flywheel exercise machines", University of Tartu, 2014.

Hanno Soo, "Optical positioner for the production of paint cans", University of Tartu, 2014.

Master's theses:

Erich Tohvre, "Educational Laboratory of Renewable Energy", Estonian University of Life Sciences, Tartu 2009.

Practical works composed by me:

Fred Valk, "Introduction to Nuclear Energy", Estonian University of Life Sciences, Tartu, 2009.

ELULOOKIRJELDUS

Ees- ja perekonnanimi:	Fred Valk
Sünniaeg ja -koht:	25.12.1979, Rapla
Kodakondsus:	Eesti
Telefon:	+372 56 917827
Kontaktaadress:	Tartu Ülikool, Füüsika Instituut, Physicum 415D, W. Ostwaldi 1, 50411 Tartu, Eesti
E-post:	fred.valk@il.ee

Haridus:

2005–2009	Tartu Ülikool, Füüsika Instituut, doktorantuur.
2003–2005	Tartu Ülikool, M.Sc. füüsikas.
1999–2000	ajateenistus Eesti Kaitseväes, radist.
1998–2003	Tartu Ülikool, B.Sc. füüsikas.
1995–1998	Rapla Vesiroosi Gümnaasium.

Teenistuskäik:

2010–	OÜ Insenerlahendused, juhataja.
2005–2015	Tartu Ülikool, Füüsika Instituut, insener.
2006–2009	Eesti Maaülikool, Tehnikainstituut, mittekoosseisuline lektor.

Erialane enesetäiendus:

09.2006 –	Plasmafüüsika teemaline suvekool „IPP Summer University for Plasma Physics 2007“, Garching, Saksamaa.
07.2006 –	Intensiivsuste suhte kalibratsiooni- ja kontrollmõõtmised Greifswaldi Ülikoolis, juuli 2006, Greifswald, Saksamaa.
06.2005 –	Plasmafüüsika teemaline suvekool „SUMTRAIC 2005“, Plasmafüüsika Instituut, Tokamaki osakond, juuni 2005, Praha, Tšehhi.

Minu poolt loetud kursused:

Füüsika põhikursus, TET 3.2411, 6 EAP, Eesti Maaülikool.

Digitaalne signaalitöötlus, LOTI.05.026, 3 EAP, Tartu Ülikool.

Minu juhendamisel valminud bakalaureuse- ja diplomitööd:

Mihkel Rähn, „Mitteiseseisva gaaslahenduse volt-amper tunnusjoon sõltuvalt fotokatoodi omadustest“, Tartu Ülikool, 2006.

Artur Tamm, „Lämmastiku molekulaarse iooni ergastatud seisundi põrkelise kustutusteguri spektroskoopiline määramine“, Tartu Ülikool, 2008.

Mikk Viidebaum, „Elektronide ruumilise jaotuse määramine gaas-lahendusplasmas optilise kiirguse kaudu“, Tartu Ülikool, 2009.

Kaarel Prommik, „AS Estiko-Plastari tootmisliinide optimeerimise projekt“, Eesti Maaülikool, Tartu 2010.

Taavi Väljaots, „Atonoomne manussüsteem LED-valgustusele“, EMÜ Tartu Tehnikakolledž, 2012.

Karl Tiirik, „Tööjuhendi koostamine tutvumiseks digitaalse signaalitöötlusprotsessoriga TMS320VC5510“, Tartu Ülikool, 2012.

Madis Sepp, „Täisautonoomse juhtprogrammi loomine andmehõive-moodulile Java keeles“, Tartu Ülikool, 2012.

Antti Jaaniste, „Android operatsioonisüsteemil põhinev mõõtesüsteem treeninguseadmetele“, Tartu Ülikool, 2014.

Hanno Soo, „Optiline värvipurkide asendimääraja“, Tartu Ülikool, 2014.

Minu juhendamisel valminud magistritööd:

Erich Tohvre, „Alternatiivenergeetika õppelabor“, Eesti Maaülikool, Tartu, 2009.

Minu koostatud praktikumijuhendid:

Fred Valk, „Tutvumine tuumaenergiaga“, Eesti Maaülikool, Tartu, 2009.

DISSERTATIONES PHYSICAE UNIVERSITATIS TARTUENSIS

1. **Andrus Ausmees.** XUV-induced electron emission and electron-phonon interaction in alkali halides. Tartu, 1991.
2. **Heiki Sõnajalg.** Shaping and recalling of light pulses by optical elements based on spectral hole burning. Tartu, 1991.
3. **Sergei Savihhin.** Ultrafast dynamics of F-centers and bound excitons from picosecond spectroscopy data. Tartu, 1991.
4. **Ergo Nõmmiste.** Leelishalogeniidide röntgenelektronemissioon kiiritamisel footonitega energiaga 70–140 eV. Tartu, 1991.
5. **Margus Rätsep.** Spectral gratings and their relaxation in some low-temperature impurity-doped glasses and crystals. Tartu, 1991.
6. **Tõnu Pullerits.** Primary energy transfer in photosynthesis. Model calculations. Tartu, 1991.
7. **Olev Saks.** Attoampri diapasoonis voolude mõõtmise füüsikalised alused. Tartu, 1991.
8. **Andres Virro.** AlGaAsSb/GaSb heterostructure injection lasers. Tartu, 1991.
9. **Hans Korge.** Investigation of negative point discharge in pure nitrogen at atmospheric pressure. Tartu, 1992.
10. **Jüri Maksimov.** Nonlinear generation of laser VUV radiation for high-resolution spectroscopy. Tartu, 1992.
11. **Mark Aizengendler.** Photostimulated transformation of aggregate defects and spectral hole burning in a neutron-irradiated sapphire. Tartu, 1992.
12. **Hele Siimon.** Atomic layer molecular beam epitaxy of A^2B^6 compounds described on the basis of kinetic equations model. Tartu, 1992.
13. **Tõnu Reinot.** The kinetics of polariton luminescence, energy transfer and relaxation in anthracene. Tartu, 1992.
14. **Toomas Rõõm.** Paramagnetic H^{2-} and F^+ centers in CaO crystals: spectra, relaxation and recombination luminescence. Tallinn, 1993.
15. **Erko Jalviste.** Laser spectroscopy of some jet-cooled organic molecules. Tartu, 1993.
16. **Alvo Aabloo.** Studies of crystalline celluloses using potential energy calculations. Tartu, 1994.
17. **Peeter Paris.** Initiation of corona pulses. Tartu, 1994.
18. **Павел Рубин.** Локальные дефектные состояния в CuO_2 плоскостях высокотемпературных сверхпроводников. Тарту, 1994.
19. **Olavi Ollikainen.** Applications of persistent spectral hole burning in ultrafast optical neural networks, time-resolved spectroscopy and holographic interferometry. Tartu, 1996.
20. **Ülo Mets.** Methodological aspects of fluorescence correlation spectroscopy. Tartu, 1996.
21. **Mikhail Danilkin.** Interaction of intrinsic and impurity defects in CaS:Eu luminophors. Tartu, 1997.

22. **Ирина Кудрявцева.** Создание и стабилизация дефектов в кристаллах KBr, KCl, RbCl при облучении ВУФ-радиацией. Тарту, 1997.
23. **Andres Osvet.** Photochromic properties of radiation-induced defects in diamond. Tartu, 1998.
24. **Jüri Örd.** Classical and quantum aspects of geodesic multiplication. Tartu, 1998.
25. **Priit Sarv.** High resolution solid-state NMR studies of zeolites. Tartu, 1998.
26. **Сергей Долгов.** Электронные возбуждения и дефектообразование в некоторых оксидах металлов. Тарту, 1998.
27. **Kaupo Kukli.** Atomic layer deposition of artificially structured dielectric materials. Tartu, 1999.
28. **Ivo Heinmaa.** Nuclear resonance studies of local structure in $RBa_2Cu_3O_{6+x}$ compounds. Tartu, 1999.
29. **Aleksander Shelkan.** Hole states in CuO_2 planes of high temperature superconducting materials. Tartu, 1999.
30. **Dmitri Nevedrov.** Nonlinear effects in quantum lattices. Tartu, 1999.
31. **Rein Ruus.** Collapse of 3d (4f) orbitals in 2p (3d) excited configurations and its effect on the x-ray and electron spectra. Tartu, 1999.
32. **Valter Zazubovich.** Local relaxation in incommensurate and glassy solids studied by Spectral Hole Burning. Tartu, 1999.
33. **Indrek Reimand.** Picosecond dynamics of optical excitations in GaAs and other excitonic systems. Tartu, 2000.
34. **Vladimir Babin.** Spectroscopy of exciton states in some halide macro- and nanocrystals. Tartu, 2001.
35. **Toomas Plank.** Positive corona at combined DC and AC voltage. Tartu, 2001.
36. **Kristjan Leiger.** Pressure-induced effects in inhomogeneous spectra of doped solids. Tartu, 2002.
37. **Helle Kaasik.** Nonperturbative theory of multiphonon vibrational relaxation and nonradiative transitions. Tartu, 2002.
38. **Tõnu Laas.** Propagation of waves in curved spacetimes. Tartu, 2002.
39. **Rünno Lõhmus.** Application of novel hybrid methods in SPM studies of nanostructural materials. Tartu, 2002.
40. **Kaido Reivelt.** Optical implementation of propagation-invariant pulsed free-space wave fields. Tartu, 2003.
41. **Heiki Kasemägi.** The effect of nanoparticle additives on lithium-ion mobility in a polymer electrolyte. Tartu, 2003.
42. **Villu Repän.** Low current mode of negative corona. Tartu, 2004.
43. **Алексей Котлов.** Оксианионные диэлектрические кристаллы: зонная структура и электронные возбуждения. Tartu, 2004.
44. **Jaak Talts.** Continuous non-invasive blood pressure measurement: comparative and methodological studies of the differential servo-oscillometric method. Tartu, 2004.
45. **Margus Saal.** Studies of pre-big bang and braneworld cosmology. Tartu, 2004.

46. **Eduard Gerškevitš.** Dose to bone marrow and leukaemia risk in external beam radiotherapy of prostate cancer. Tartu, 2005.
47. **Sergey Shchemelyov.** Sum-frequency generation and multiphoton ionization in xenon under excitation by conical laser beams. Tartu, 2006.
48. **Valter Kiisk.** Optical investigation of metal-oxide thin films. Tartu, 2006.
49. **Jaan Aarik.** Atomic layer deposition of titanium, zirconium and hafnium dioxides: growth mechanisms and properties of thin films. Tartu, 2007.
50. **Astrid Rekker.** Colored-noise-controlled anomalous transport and phase transitions in complex systems. Tartu, 2007.
51. **Andres Punning.** Electromechanical characterization of ionic polymer-metal composite sensing actuators. Tartu, 2007.
52. **Indrek Jõgi.** Conduction mechanisms in thin atomic layer deposited films containing TiO_2. Tartu, 2007.
53. **Aleksei Krasnikov.** Luminescence and defects creation processes in lead tungstate crystals. Tartu, 2007.
54. **Küllike Rägo.** Superconducting properties of MgB_2 in a scenario with intra- and interband pairing channels. Tartu, 2008.
55. **Els Heinsalu.** Normal and anomalously slow diffusion under external fields. Tartu, 2008.
56. **Kuno Kooser.** Soft x-ray induced radiative and nonradiative core-hole decay processes in thin films and solids. Tartu, 2008.
57. **Vadim Boltrushko.** Theory of vibronic transitions with strong nonlinear vibronic interaction in solids. Tartu, 2008.
58. **Andi Hektor.** Neutrino Physics beyond the Standard Model. Tartu, 2008.
59. **Raavo Josepson.** Photoinduced field-assisted electron emission into gases. Tartu, 2008.
60. **Martti Pärs.** Study of spontaneous and photoinduced processes in molecular solids using high-resolution optical spectroscopy. Tartu, 2008.
61. **Kristjan Kannike.** Implications of neutrino masses. Tartu, 2008.
62. **Vigen Issahhanjan.** Hole and interstitial centres in radiation-resistant MgO single crystals. Tartu, 2008.
63. **Veera Krasnenko.** Computational modeling of fluorescent proteins. Tartu, 2008.
64. **Mait Müntel.** Detection of doubly charged higgs boson in the CMS detector. Tartu, 2008.
65. **Kalle Kepler.** Optimisation of patient doses and image quality in diagnostic radiology. Tartu, 2009.
66. **Jüri Raud.** Study of negative glow and positive column regions of capillary HF discharge. Tartu, 2009.
67. **Sven Lange.** Spectroscopic and phase-stabilisation properties of pure and rare-earth ions activated ZrO_2 and HfO_2. Tartu, 2010.
68. **Aarne Kasikov.** Optical characterization of inhomogeneous thin films. Tartu, 2010.
69. **Heli Valtna-Lukner.** Superluminally propagating localized optical pulses. Tartu, 2010.

70. **Artjom Vargunin.** Stochastic and deterministic features of ordering in the systems with a phase transition. Tartu, 2010.
71. **Hannes Liivat.** Probing new physics in e+e− annihilations into heavy particles via spin orientation effects. Tartu, 2010.
72. **Tanel Mullari.** On the second order relativistic deviation equation and its applications. Tartu, 2010.
73. **Aleksandr Lissovski.** Pulsed high-pressure discharge in argon: spectroscopic diagnostics, modeling and development. Tartu, 2010.
74. **Aile Tamm.** Atomic layer deposition of high-permittivity insulators from cyclopentadienyl-based precursors. Tartu, 2010.
75. **Janek Uin.** Electrical separation for generating standard aerosols in a wide particle size range. Tartu, 2011.
76. **Svetlana Ganina.** Hajusandmetega ülesanded kui üks võimalus füüsikaõppe efektiivsuse tõstmiseks. Tartu, 2011.
77. **Joel Kuusk.** Measurement of top-of-canopy spectral reflectance of forests for developing vegetation radiative transfer models. Tartu, 2011.
78. **Raul Rammula**. Atomic layer deposition of HfO_2 – nucleation, growth and structure development of thin films. Tartu, 2011.
79. **Сергей Наконечный.** Исследование электронно-дырочных и интерстициал-вакансионных процессов в монокристаллах MgO и LiF методами термоактивационной спектроскопии. Тарту, 2011.
80. **Niina Voropajeva.** Elementary excitations near the boundary of a strongly correlated crystal. Tartu, 2011.
81. **Martin Timusk.** Development and characterization of hybrid electro-optical materials. Tartu, 2012, 106 p.
82. **Merle Lust.** Assessment of dose components to Estonian population. Tartu, 2012, 84 p.
83. **Karl Kruusamäe.** Deformation-dependent electrode impedance of ionic electromechanically active polymers. Tartu, 2012, 128 p.
84. **Liis Rebane.** Measurement of the $W \to \tau\nu$ cross section and a search for a doubly charged Higgs boson decaying to τ-leptons with the CMS detector. Tartu, 2012, 156 p.
85. **Jevgeni Šablonin.** Processes of structural defect creation in pure and doped MgO and NaCl single crystals under condition of low or super high density of electronic excitations. Tartu, 2013, 145 p.
86. **Riho Vendt**. Combined method for establishment and dissemination of the international temperature scale. Tartu, 2013, 108 p.
87. **Peeter Piksarv.** Spatiotemporal characterization of diffractive and non-diffractive light pulses. Tartu, 2013, 156 p.
88. **Anna Šugai.** Creation of structural defects under superhigh-dense irradiation of wide-gap metal oxides. Tartu, 2013, 108 p.
89. **Ivar Kuusik.** Soft X-ray spectroscopy of insulators. Tartu, 2013, 113 p.
90. **Viktor Vabson**. Measurement uncertainty in Estonian Standard Laboratory for Mass. Tartu, 2013, 134 p.

91. **Kaupo Voormansik.** X-band synthetic aperture radar applications for environmental monitoring. Tartu, 2014, 117 p.
92. **Deivid Pugal.** hp-FEM model of IPMC deformation. Tartu, 2014, 143 p.
93. **Siim Pikker.** Modification in the emission and spectral shape of photostable fluorophores by nanometallic structures. Tartu, 2014, 98 p.
94. **Mihkel Pajusalu**. Localized Photosynthetic Excitons. Tartu, 2014, 183 p.
95. **Taavi Vaikjärv.** Consideration of non-adiabaticity of the Pseudo-Jahn-Teller effect: contribution of phonons. Tartu, 2014, 129 p.
96. **Martin Vilbaste.** Uncertainty sources and analysis methods in realizing SI units of air humidity in Estonia. Tartu, 2014, 111 p.
97. **Mihkel Rähn.** Experimental nanophotonics: single-photon sources- and nanofiber-related studies. Tartu, 2015, 107 p.
98. **Raul Laasner.** Excited state dynamics under high excitation densities in tungstates. Tartu, 2015, 125 p.
99. **Andris Slavinskis.** EST Cube-1 attitude determination. Tartu, 2015, 104 p.
100. **Karlis Zalite**. Radar Remote Sensing for Monitoring Forest Floods and Agricultural Grasslands. Tartu, 2016, 124 p.
101. **Kaarel Piip.** Development of LIBS for *in-situ* study of ITER relevant materials. Tartu, 2016, 93 p.
102. **Kadri Isakar.** ^{210}Pb in Estonian air: long term study of activity concentrations and origin of radioactive lead. Tartu, 2016, 107 p.
103. **Artur Tamm.** High entropy alloys: study of structural properties and irradiation response. Tartu, 2016, 115 p.
104. **Rasmus Talviste.** Atmospheric-pressure He plasma jet: effect of dielectric tube diameter. Tartu, 2016, 107 p.
105. **Andres Tiko.** Measurement of single top quark properties with the CMS detector. Tartu, 2016, 161 p.
106. **Aire Olesk.** Hemiboreal Forest Mapping with Interferometric Synthetic Aperture Radar. Tartu, 2016, 121 p.